國立臺灣大學工學院材料科學與工程學研究所

博士論文

Department of Material Science and Engineering

College of Engineering

National Taiwan University

Doctoral Dissertation

利用原子氣相沉積技術成長氧化鋅磊晶薄膜與 *n*型氧化鋅/ *p*型氮化鎵異質介面發光二極體之研究

Characteristics of ZnO epilayers and *n*-ZnO/*p*-GaN hetrojunction light-emitting diodes grown by atomic layer deposition

陳星兆

Hsing-Chao Chen

指導教授：陳敏璋 博士

Advisor: Miin-Jang Chen, Ph.D.

中華民國 99 年 7 月

July, 2010

致謝

感謝我的父母支持我讀完博士學位，不斷給我鼓勵及照顧我的生活所需，讓我專心唸書，而不用負擔生活的瑣事。也感謝我的女朋友劉方慈在一路上的陪伴，分享我的喜悅與哀愁。感謝宏昌(養樂多)及孟楷在碩士班時給了我許多快樂的回憶，從馬利歐賽車到FIFA、CS與世紀，那是個黃金年代。感謝施穎蒼學長跟我一起走過這四年辛苦的路程，甘苦與共。感謝眾多學弟，祥祥讓我有很多機會練習將裝丙酮、Aki是我的世紀導師、阿邱的傻、修哥的帥、鳥人的白爛、蔡曄提供的游泳池、盈伸、煌大、葉B、郁勛、阿呑、阿哈、棋王等人的陪伴，一起渡過無數個鳳城的夜晚、一起橫渡日月潭、八八水災的愛心募捐……等等。這一切都將是我永生難忘的回憶。也感謝我的指導教授陳敏璋教授，讓我自由自在的學習、成長。

摘要

本論文研究使用原子層沉積技術所成長之氧化鋅磊晶薄膜其晶體結構、光激發光以及電激發光之性質。以原子層沉積技術所成長之氧化鋅薄膜在高溫退火後其結晶方向為高度c-軸取向，且於穿透式電子顯微鏡(TEM)的觀察下並無明顯的貫穿式差排(threading dislocation)出現。而其發光性質良好，自發輻射(spontaneous emission)之主要發光波長為378nm的紫外光，缺陷發光強度約為紫外光強度之千分之一。光激發受激輻射(optically-pumped stimulated emission)之起始值(threshold)為33.3kW/cm^2，且此起始值隨著鋁原子摻雜濃度的升高而逐漸降低，此現象可歸因於random lasing之產生，而此random lasing現象的發生及來源可藉由兩種不同摻雜模式之鋁摻雜氧化鋅薄膜其所表現出不同的光學性質來佐證。

為研究其電激發光之性質，本研究將氧化鋅磊晶薄膜以原子層沉積技術成長於*p*型氮化鎵上以製作*n*-ZnO/*p*-GaN異質接面發光二極體(LED)。此發光二極體於順向偏壓下發出391nm之紫外光及425nm之藍光，其中391nm之紫外光為氧化鋅薄膜所產生，而425nm之藍光則源自於*p*型氮化鎵。另外本研究亦發現，若於此發光二極體背面鍍上金屬反射層，則氧化鋅薄膜所發之紫外光隨著電流的上升而呈現出非線性上升的現象，可歸因為amplified spontaneous emission的發生。

另一方面，將此*n*-ZnO/*p*-GaN異質接面發光二極體操作在逆向偏壓時可觀察到白光的產生。此白光為波長分別為430nm的藍光與550nm的黃光混合而成，其於色域圖上之座標為(0.31,0.36)與理想之白光座標(0.33,0.33)十分接近。另外若於氧化鋅薄膜中摻雜鋁原子，可在此*n*-ZnO/*p*-GaN異質接面發光二極體於逆向偏壓操作下觀察到波長範圍為370nm-396nm之紫外光，此紫外光是由*p*型氮化鎵所產生，其發光波長隨著空乏區電場強度的增加而紅位移，其成因為excitonic Franz-Keldysh所導致。

由上述結果可以得知，以原子層沉積技術所成長之氧化鋅磊晶薄膜具有良好的晶體品質及光學性質，可以應用於下一世代的高效率發光元件。

關鍵字： 原子層沉積、氧化鋅、貫穿式差排、受激輻射、發光二極體、紅位移。

Abstract

High-quality ZnO epilayers were grown on the (0002) sapphire substrate by atomic layer deposition (ALD) and treated by post-deposition thermal annealing. The highly c-axis orientated, well crystallized ZnO epilayers and dominant ultraviolet (UV) near-band-edge emission with negligible defect-related bands were manifested by the X-ray diffraction pattern, transmission electron microscopy images and photoluminescence measurement. A low-threshold (33.3 kW/cm^2) optically-pumped stimulated emission was observed in the ZnO epilayers. It was found that the threshold gradually decreased with the increase in the Al doping concentration in the ZnO films. The onset of random lasing was proposed to be the reason of the reduction in the threshold of stimulated emission.

The high-quality ZnO epilayers were grown by ALD on the *p*-type GaN and treated by rapid thermal annealing to form the *n*-ZnO/*p*-GaN heterojunction light-emitting diodes (LEDs). The LEDs exhibited a competition between the electroluminescnce (EL) from the *n*-ZnO (λ=391 nm) and *p*-GaN (λ=425 nm). On the other hand, the effect of external feedback on the UV EL from *n*-ZnO/*p*-GaN heterojunction LEDs was also studied. The super-linear increase in the UV EL intensity from ZnO with the injection current was observed, attributed to the occurrence of amplified spontaneous emisson in the ZnO epilayer.

White-light EL from the *n*-ZnO/*p*-GaN hetrojunction LEDs operated at reverse breakdown bias was also reported. The EL spectrum was composed of the blue light at 430 nm and broad yellow band around 550 nm. The chromaticity coordinate of the EL spectrum was estimated to be (0.31,0.36), very close to (0.33,0.33) of the standard white light. Significant ultraviolet (UV) electroluminescence (EL) coupled with a red shift from *n*-ZnO/*p*-GaN hetrojunction LEDs diodes was observed under the reverse

breakdown bias. The reverse breakdown is attributed to the type II band alignment with large band offsets between *n*-ZnO and *p*-GaN heterojunction, which facilitates electron tunneling from the valence band in *p*-GaN to the conduction band in *n*-ZnO.Theoretical calculations were carried out to fit the EL spectra, indicating that the excitonic Franz-Keldysh effect under a large electric field in the depletion region of *p*-GaN is responsible for the red shift in the UV EL spectra.

The crystal structures and optical properties of ZnO epilayers and the *n*-ZnO/*p*-GaN hetrojunction LEDs grown by ALD were studied in this thesis. The results indicate that the ALD technique is a very promising approach to the growth of high-quality ZnO epilayers for the next-generation UV photonic devices.

Keywords: ALD, ZnO, threading dislocation, stimulated emission, light emitting diode, red-shift.

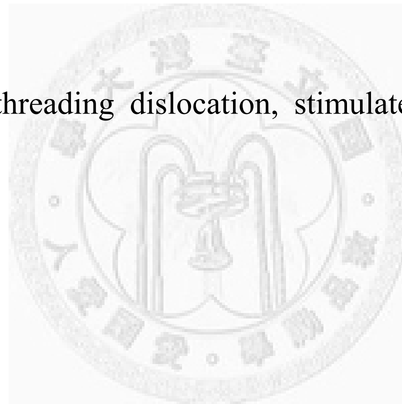

Table of Contents

Chapter 1 1
Introduction 1
1.1 Motivation 1
1.2 Outline of this thesis 2
1.3 Characteristics of ZnO 4
1.4 Franz-Keldysh Effect 8
Reference 12
Chapter 2 15
Structure of ZnO epilayer grown by atomic layer deposition on the sapphire substrate 15
2.1 Introduction 15
2.2 Sample preparation 16
2.3 Experimental procedure 17
2.4 Results and Discussion 17
2.4.1 X-ray diffraction 17
2.4.2 Cross-sectional TEM 19
2.4.3 High resolution TEM 19
2.4.4 Optical property 21
2.5 Summary 23
Reference 24
Chapter 3 27
Stimulated Emission in ZnO and ZnO:Al Thin Films Grown by Atomic Layer Deposition 27

3.1 Introduction 27
3.2 Stimulated emission in undoped ZnO thin film 28
3.2.1 Sample preparation 28
3.2.2 Experiment procedure 29
3.2.3 Crystal quality 29
3.2.4 Stimulated emission 31
3.2.5 Al_2O_3 surface passivation 33
3.2.6 Gain spectrum 35
3.2.7 Al doping effect 36
3.3 Reduction in stimulated emission threshold of ZnO:Al 38
3.3.1 Sample preparation 38
3.3.2 Crystal quality 38
3.3.3 Reduction of the stimulated emission 39
3.4 Random lasing in heavily doped 6% ZnO:Al thin film 44
3.4.1 Sample configuration 44
3.4.2 Crystal quality 44
3.4.3 Stimulated emission with random lasing 45
3.4.4 Examining of random lasing 49
3.5 Summary 49
Chapter 4 53
Ultraviolet Electroluminescence of *n*-ZnO/*p*-GaN Heterojunction Light-Emitting Diodes at Forward Bias 53
4.1 Introduction 53
4.2 UV electroluminescence of *n*-ZnO/*p*-GaN heterojunction LED 54
4.2.1 Sample preparation 54
4.2.2 Experimental setup and procedure 55

4.2.3 Crystal quality of the ZnO film on *p*-GaN ... 56

4.2.4 Optical property of *n*-ZnO and *p*-GaN ... 61

4.2.5 Electroluminescence ... 62

4.2.6 Interfacial layer ... 63

4.2.7 Confirm the interfacial layer by C-V method ... 66

4.2.8 Competition mechanism ... 69

4.3 Electroluminescence of *n*-ZnO/*p*-GaN heterojunction LED with aluminum back reflector ... 71

4.3.1 Sample preparation ... 71

4.3.2 Electroluminescence ... 71

4.3.3 Super-linearly growth of EL intensity ... 73

4.4 Summary ... 76

Appendix 4A: four-level laser system ... 78

Reference ... 80

Chapter 5 ... 83

White Light and Avalanche UV Electroluminescence of *n*-ZnO /*p*-GaN Hetrojunction Light-Emitting Diodes at Reverse Breakdown Bias ... 83

5.1 Introduction ... 83

5.2 White-light Electroluminescence ... 84

5.2.1 Sample preparation ... 84

5.2.2 Current *vs.* Voltage (*I-V*) characteristics ... 86

5.2.3 Optical and crystal quality ... 87

5.2.4 White light electroluminescence ... 88

5.2.5 Discussion ... 88

5.2.6 White light in CIE chromaticity coordinate ... 94

5.3 Excitonic Franz-Keldysh effect in ultraviolet electro- luminescence from

n-ZnO:Al/*p*-GaN:Mg heterojunction light-emitting diodes operated at reverse breakdown bias 94

5.3.1 Sample preparation 94

5.3.2 Current vs. Voltage (*I*-*V*) characteristics 96

5.3.3 Photoluminescence of *n*-ZnO:Al and the *p*-GaN films 98

5.3.4 Breakdown electroluminescence 98

5.3.5 Discussion 101

5.4 Summary 104

Appendix 5A 106

Appendix 5B 113

Reference 117

Chapter 6 121

Conclusion 121

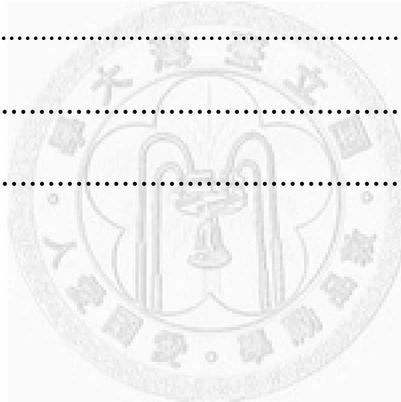

List of Figures

Figure 1.1 the crystal structure of ZnO (wurtzite structure) which can be regarded as a hexagonal closed packed structure with four basis atoms. In which the atoms 1 and 2 are anions (oxygen) and the atoms 3 and 4 are cations (zinc). **5**

Figure 1.2 the tight binding method (TBM) band structure of ZnO (wurtzite structure) of wavevector in [001] and [100] direction. **5**

Figure 1.3 the band diagram of excion-exciton scattering. After the inelastic collision between the excitons, one is excited into a higher state and the other is transformed into a photon. **7**

Figure 1.4 the band diagram of band gap renormalization induced by many body effect as the electron-hole concentration exceeds the Mott density. **8**

Figure 1.5 Franz-Keldysh effect or photon-assisted absorption in a bulk semiconductor with a uniform electric field bias. **9**

Figure 1.6 Absorption spectrum for a finite field F≠0 (solid line). The dashed line is the free electron and hole absorption spectrum without an applied electric field (F=0). **10**

Figure 2.1 X-ray diffraction pattern of the ZnO epilayer grown on the *c*-Al_2O_3 substrate. **18**

Figure 2.2 Cross-sectional transmission electron microscopy (TEM) image of the ZnO epilayer grown on the *c*-Al_2O_3 substrate. **18**

Figure 2.3 High-resolution TEM (HRTEM) image of an area including the ZnO/Al_2O_3 interface. Computer diffractograms are of the small areas

indicated by a, b, and c and the whole area (all). Indexes in diffractogam a correspond to the lattice fringes of Al_2O_3 crystal and indexes in diffractograms b and c correspond to the lattice fringes of ZnO crystal. In the diffractogram all, the spots enclosed by large circles come from ZnO and the spots enclosed by small circles originate from Al_2O_3. .... **20**

Figure 2.4 HRTEM image of the area enclosed by a square in Fig. 2.2. .... **22**

Figure 2.5 Spontaneous emission PL spectrum of the ZnO epilayer pumped by a CW He-Cd laser at room temperature. The inset is the plot of the same PL spectrum in the logarithm scale. **22**

Figure 3.1 XRD pattern of the post-annealed ZnO film *without* the Al_2O_3 surface passivation layer. **30**

Figure 3.2 XRD patterns of the as-deposited and post-annealed ZnO films *without* the Al_2O_3 surface passivation layer.................................. **30**

Figure 3.3 Room-temperature PL spectra of the post-annealed ZnO film *with* the Al_2O_3 surface passivation layer at various excitation intensities. The inset is the PL spectrum at an excitation intensity of 17.2 kW/cm^2. **31**

Figure 3.4 The integrated PL intensity as function of the excitation intensity of the post-annealed ZnO films *with* and *without* the Al_2O_3 surface passivation layer. **33**

Figure 3.5 PL measurements of the as-deposited ZnO films *with* and *without* the Al_2O_3 passivation layer: (a) PL spectra at an excitation intensity of 244 kW/cm^2. (b) The integrated PL intensity as function of the excitation intensity. **34**

Figure 3.6 The optical gain spectra of the post-annealed ZnO film *with* the Al_2O_3 surface passivation layer at excitation intensities of (a) 59.2

kW/cm^2 and (b) 102.6 kW/cm^2. .... **36**

Figure 3.7 XRD patterns and FWHM widths of the (0002) peaks of the ZnO:Al films with Al doping percentage of 0%, 2%, and 4%. **39**

Figure 3.8 PL spectra of the ZnO:Al film with 0% Al doping percentage. The inset is the integrated PL intensity as a function of the excitation intensity. **40**

Figure 3.9 PL spectra of the ZnO:Al film with 4% Al doping percentage. The inset is the integrated PL intensity as a function of the excitation intensity. **40**

Figure 3.10 Threshold for stimulate emission of ZnO:Al films versus the Al dopingpercentage. **42**

Figure 3.11 Two different configuration of Al doped ZnO:Al thin films. Configure A is the uniformly doped ZnO:Al film, and configure B is the concentrated doped ZnO:Al. **44**

Figure 3.12 The XRD patterns measured in θ-2θ configuration, normalized by the intensity of ZnO (0002) peak. (a) the 6% Al doped ZnO grown by spread doping configuration; (b) the 6% Al doped ZnO grown by concentrated doping configuration. **45**

Figure 3.13 The photoluminescence spectrums of the spread doping sample of various excitation powers. The inset is the integral intensity of different excitation powers. **46**

Figure 3.14 The photoluminescence spectrums of the concentrated doping sample of various excitation powers. The inset is the integral intensity of different excitation powers. **47**

Figure 3.15 The photoluminescence spectrums of concentrated doping sample in 0°, 30° and 60° directions. **48**

Figure 4.1 The device structure of the *n*-ZnO/*p*-GaN heterojunction LED. **54**

Figure 4.2. Experimental configuration for the measurement of EL spectra. **56**

Figure 4.3 (a) X-ray diffraction patterns and (b) X-ray rocking curves of the as-deposited and post-annealed ZnO films grown by ALD on *p*-GaN. **57**

Figure 4.4 Cross-sectional bright field transmission electron microscopy (TEM) image of the *n*-ZnO/*p*-GaN heterojunction on the underlying GaN and Al_2O_3 substrate, and selected-area electron diffraction patterns from the Al_2O_3 layer, the interfacial layer and the ZnO layer. The spots in the interfacial layer comprise the spots from the ZnO (whose 0002 and $11\bar{2}0$ spots are marked) and additional spots from an unknown crystal formed with an orientation with their *c*-axis. **59**

Figure 4.5 Cross-sectional TEM image of an area in the *n*-ZnO/*p*-GaN heterojunction. **60**

Figure 4.6 Room temperature (RT) photoluminescence spectra of the *p*-GaN layer and the *n*-ZnO layer grown on the *p*-GaN. **61**

Figure 4.7 I-V curve of the n-ZnO/p-GaN heterojunction LED. The insets show the EL image of the n-ZnO/p-GaN heterojunction LED. **62**

Figure 4.8 Room temperature EL spectra of the *n*-ZnO/*p*-GaN heterojunction LED at various DC injection currents. The inset shows the EL peak intensities of the *n*-ZnO (λ=391 nm) and *p*-GaN (λ=425 nm) as a function of the injection current. **63**

Figure 4.9 (a) and (b) are High-resolution TEM images of the interfacial layer between ZnO and GaN. **64**

Figure 4.10 High-angle annular dark-field scanning transmission electron microscopy image of the *n*-ZnO/*p*-GaN heterojunction on the GaN layer. **65**

Figure 4.11 Capacitance *vs.* voltage (*C-V*) curves of the *n*-ZnO/*p*-GaN structures *with* and *without* the RTA treatment. **67**

Figure 4.12 (a) Band diagram of the *n*-ZnO/*p*-GaN heterojunction without applying voltage. (b) Band diagram of the *n*-ZnO/*p*-GaN heterojunction. The GaN electrode is grounded and the positive voltage is applied to the ZnO electrode (reverse bias for the *pn* junction). **68**

Figure 4.13 Schematic diagram of the devices. Aluminum was evaporated on the back of the c-Al_2O_3 substrate as a reflector in device (A). The back side is maintained polish in device (B). The back side is roughened by diamond blend in device (C). **71**

Figure 14.14 Room-temperature EL spectra of the device shown in the inset of Fig.4.13(a) at various pulsed currents from 300 mA to 800 mA. The inset is the normalized PL spectra of the *n*-ZnO and *p*-GaN layers at room temperature. **72**

Figure 4.15 Room-temperature EL spectra of devices A, B, and C at a pulsed current of 800 mA. The inset presents the Gaussian functions (dash lines) were used to fit the EL spectra to extract the EL intensities and FWHM of ZnO and GaN.. .... **72**

Figure 4.16 (a) The EL peak intensity as a function of the injection current of devices A, B, and C for GaN. (b) The EL peak intensity (solid line) and applied voltage (doted line) as a function of the injection current of the three devices for ZnO. The inset in (b) shows the variations of the FWHM of ZnO spectral peak with injection current for devices A, B and C.

.... **74**
Figure 4.17 Variations of the FWHM of ZnO spectral peak with injection current for devices A, B and C.. **75**
Figure 4A-1 Schematic diagram of four-level laser system................. **78**
Figure 5.1 Device structure of the *n*-ZnO/*p*-GaN hetrojunction LED. **85**
Figure 5.2 Room-temperature *I-V* curve of the *n*-ZnO/*p*-GaN heterojunction LED. The inset shows the *I-V* curve of two Ni/Au contacts on *p*-GaN.. **86**
Figure 5.3 Room-temperature PL spectra of the *p*-GaN layer and the thick (540 nm) *n*-ZnO layer grown on the *p*-GaN. The inset is the HRTEM image of this thick *n*-ZnO layer in the region near the top surface......... **87**
Figure 5.4 Room-temperature EL spectra of the *n*-ZnO/*p*-GaN heterojunction LED measured at various DC injection current from 1 to 15 mA under the reverse breakdown biases. The inset is the EL image of the LED in a bright room... **89**
Figure 5.5 Room-temperature PL spectrum of the thin (90 nm) *n*-ZnO layer grown on the *p*-GaN *with/without* post-annealing. The inset is the HRTEM image of the interfacial layer between *n*-ZnO and *p*-GaN of the sample after the RTA treatment. **89**
Figure 5.6 The band diagram of the undoped-GaN/*p*-GaN/*n*-ZnO of the LED under the reverse breakdown bias.. **91**
Figure 5.7 The plots of $\ln(J \cdot F)$ vs. F^{-1} and $\ln(J/F^3)$ vs. F^{-1} of the *n*-ZnO/*p*-GaN hetrojection the under reverse breakdown bias................ **93**
Figure 5.8 The schematic diagram of the 8% *n*-ZnO:Al/*p*-GaN heterojunction LED.. **95**

Figure 5.9 Room-temperature Current *vs*. Reverse-bias voltage (*I-V*) curve of the *n*-ZnO:Al(8%)/*p*-GaN heterojunction LED. **97**
Figure 5.10 The *ln(J/F³)* vs. *1/F* fitting curve of the n-ZnO:Al(8%)/p-GaN heterojunction LED under various reverse bias condition. The linear slope shows the occurrence of the tunnelling. The inset is the room-temperature photoluminescence (PL) spectra of the *p*-GaN layer and *n*-ZnO:Al(8%) layer grown on the *p*-GaN. **97**
Figure 5.11 Room-temperature electroluminescence (EL) spectra of the *n*-ZnO:Al(8%)/*p*-GaN heterojunction LED measured at various injection currents from 35 mA to 75 mA under the reverse breakdown biases. **99**
Figure 5.12 The EL spectra of *n*-ZnO:Al(2%)/*p*-GaN heterojunction LED measured at various injection currents under the reverse breakdown biases. This figure shows the intensity of UV light increase with the current increase but the blue light decrease with current increase. **100**
Figure 5.13 The normalized (a) EL spectra (b) fitting curves of *n*-ZnO:Al(8%)/*p*-GaN heterojunction LED. **101**
Figure 5.14 The band diagram of the *n*-ZnO:Al(8%)/*p*-GaN heterojunction LED. **102**
Figure A-1 The band diagram of an electron in a bound state tunneling to a free state. **106**
Figure A-2 Energy vs. square of the wave vector for electrons in the forbidden band. (ref. K. H. Gundlach, *J. Appl. Phys.* 44 pp.5005-5010, 1973) **107**
Figure 5B-1 Band diagram of the p-n junction and the shadow region is the band to band tunneling region. **113**

List of Tables

Table 3.1 Hall effect measurements of the as-deposited and post-annealed ZnO films. **37**
Table 3.2 Hall effect measurement of the ZnO:Al films with Al doping percentage of 0%, 2%, and 4%. **42**

Chapter 1

Introduction

1.1 Motivation

To date, the II-VI semiconductor ZnO is commonly suggested as the next generation material for the ultraviolet photonic devices, such as ultraviolet (UV) light-emitting diodes (LEDs), photo-detectors and lasers because its high excitonic binding energy (60 meV) and wide band gap energy (3.37 eV). The high excitonic binding energy of ZnO, excitonic binding energy of GaN is 24 meV [1], leads it to more efficient UV light emission and a reduced lasing threshold at room temperature. In addition, ZnO also has the following advantages: easily to perform wet etching process, relatively low cost, stable, and environmental friendly, which enable ZnO as the next generation LEDs, LDs or other photonic devices. However, the difficulty to produce stable and reproducible high carrier concentration and low resistivity *p*-type ZnO impedes the fabrication of ZnO based optoelectronic device.

Many techniques have been used to grow high-quality ZnO films, including molecular beam epitaxy (MBE) [2-5], metal-organic chemical vapor deposition (MOCVD) [6-9], chemical vapor deposition (CVD) [10-11], pulsed laser deposition (PLD) [12], radio-frequency magnetron sputtering (RFMS) [13-15], and filtered cathodic vacuum arc technique [16,17]. Lim *et al.* reported that ZnO films grown on the (0001) sapphire (c-Al_2O_3) at 200-275°C by electron cyclotron resonance-assisted MBE were basically single crystals, which comprised subgrains with 15~150 nm in size and accompanied by threading dislocations [3]. Generally, a lot of columnar grains were embedded in the ZnO films grown by MOCVD [6-9]. PLD and RFMS may be the most popular techniques for preparation of ZnO films, but they usually require a high growth temperature (above 350°C or more).

Atomic layer deposition (ALD) is another noteworthy method of growing high-quality ZnO films [18-20]. ALD is a kind of CVD technique, however, contrary to the conventional CVD, the reation in ALD precedes the reaction solely on the surface of the substrate, leading to self-limiting and layer-by-layer growth. The advantages of ALD are shown as follows:

1. easy and accurate thickness control
2. excellent conformality
3. high uniformity over a large area
4. good reproducibility
5. low defect density
6. pinhole-free structures
7. low deposition temperatures
8. large-area and large-batch capacity

from the advantages stated above, one can expect a uniform and good quality ZnO deposited by ALD. And the crystal structure, optical and optoelectronic property will be studied in this thesis.

1.2 Outline of this thesis

Four major topics are contained in this thesis. The first part is the structure and optical property of the ZnO grown by ALD. The second part is the optical property of ZnO:Al film with various Al doping concentration. The third part is the electroluminescence of n-ZnO/p-GaN hetrojunction in both forward and reverse bias. And the fourth part is the future works.

In chapter 2, a high-quality ZnO epilayer was grown on the (0001) sapphire substrate by atomic layer deposition (ALD) and followed by high-temperature rapid thermal annealing. The highly c-axis orientated and well crystallized ZnO epilayer

was manifested by the X-ray diffraction pattern and transmission electron microscopy (TEM) images. The layer-by-layer growth and low deposition temperature of ALD prevent the formation of columnar structures in the ZnO epilayer. High-resolution TEM images indicate the presence of a distorted ZnO layer at the ZnO/sapphire interface, which relaxes the misfit in ZnO and thus lead to a low threading dislocation density in the ZnO epilayer. Photoluminescence spectrum consisted of a strong ultraviolet spontaneous emission associated with the near-band-edge emission at 3.28 eV and a negligible defect-related band.

In chapter 3, ZnO and ZnO:Al thin films were grown on sapphire substrates by atomic layer deposition (ALD). A low threshold of 33.3 kW/cm^2 was observed at room temperature in the ZnO thin film with a thin Al_2O_3 passivation layer. And a threshold of stimulated emission decreases with the increasing Al concentrations was observed. The reduction in the threshold of stimulated emission was attributed to the increase in the optical scattering centers resulting from the segregation of excess Al in the heavily doped ZnO:Al films. In order to investigate the role of random lasing in the reduction of stimulated emission threshold of ZnO:Al thin film. Two configurations of concentrated and spreading 6% Al doped ZnO films were grown by atomic layer deposition (ALD). Two thresholds were observed and the appearance of random lasing was shown by the collecting PL spectrums from different angles. This result indicates that the reduction of stimulated emission threshold is actually related to the random lasing.

In chapter 4, atomic layer deposition (ALD) technique and subsequent rapid thermal annealing (RTA) were implemented to grow high-quality ZnO epilayers for the fabrication of *n*-ZnO/*p*-GaN heterojunction light-emitting diodes. A competition between the ELs from the *n*-ZnO (around 391 nm) and *p*-GaN (around 425 nm) is observed. This competition may be ascribed to the ZnO/GaN interface states coupled

with the differences between the *n*-ZnO and *p*-GaN in carrier concentration and light emission efficiency. On the other hand, the effect of external feedback on the ultraviolet (UV) electroluminescence (EL) from *n*-ZnO/*p*-GaN heterojunction light-emitting diodes at room temperature is also studied in this chapter. The back of the c-Al_2O_3 substrate was deposited with aluminum as an external-feedback reflector. Significant enhancement of the UV EL intensity and super-linear increase in the EL intensity, as well as the spectral narrowing, with the injection current have been observed, which are attributed to amplified spontaneous emission in the high-quality ZnO epilayer grown by ALD.

In chapter 5, white-light electroluminescence from the *n*-ZnO/*p*-GaN hetrojunction light-emitting diodes operated at reverse breakdown bias. The EL spectrum was composed of the blue light at 425 nm and broad yellow band around 550 nm. The chromaticity coordinate of the EL spectrum was estimated to be (0.31,0.36), very close to (0.33,0.33) of the standard white light. In addition, significant ultraviolet (UV) electroluminescence (EL) coupled with a red shift from n-ZnO:Al/p-GaN:Mg hetrojunction light-emitting diodes was observed under the reverse breakdown bias. The red shift in the EL spectral peak from 372 nm to 396 nm was observed with the increase in the reverse breakdown bias. Theoretical calculations were carried out to fit the EL spectra, indicating that the excitonic Franz-Keldysh effect under a large electric field in the depletion region is responsible for the red shift in the UV EL spectra.

1.3 Characteristics of ZnO

ZnO is a semiconductor with a direct band gap of 3.37 eV (Fig.1.1), when it crystallizes in wurtzite structure (Fig.1.2), which in principle enables optoelectronic

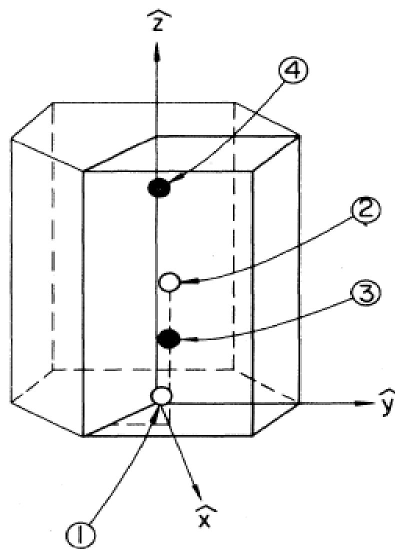

Figure 1.1 the crystal structure of ZnO (wurtzite structure) which can be regarded as a hexagonal closed packed structure with four basis atoms. In which the atoms 1 and 2 are anions (oxygen) and the atoms 3 and 4 are cations (zinc). [18]

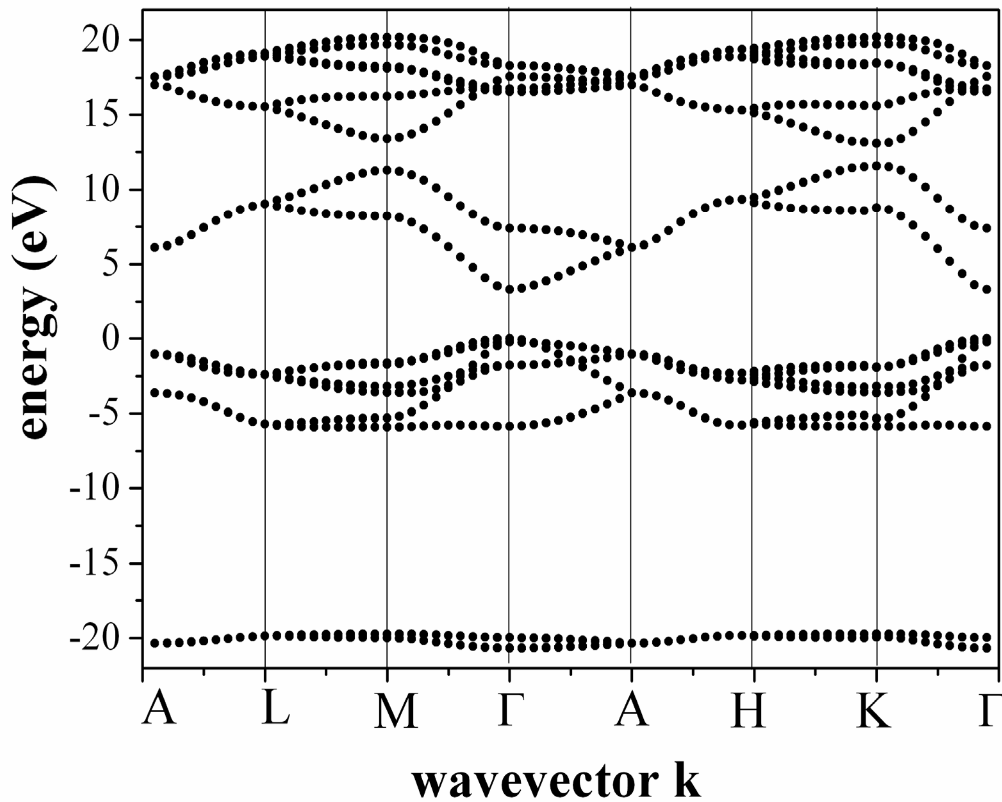

Figure 1.2 the tight binding method (TBM) band structure of ZnO (wurtzite structure) of wavevector in [001] and [100] direction.

applications in the blue and UV regions of the spectrum. The free exicton binding energy of ZnO is 60 meV, and this large exciton binding energy (compared with 25 meV of GaN) makes the efficient excitonic emission in ZnO.

Crystal structure and lattice parameters

ZnO crystallizes in the wurtzite (B4 type) structure, as shown in Fig.1.1. This is a hexagonal closed packed structure, belonging to the space group P63*mc*, and is characterized by four basis atoms, two of which are Zn^{2+} ions and others are O^{2-} ions, as shown in the Fig.1.1. And the lattice parameters of the hexagonal unit cell are a = 3.2495Å and c = 5.2069 Å.

n-type ZnO

The *n*-type nature of un-doped ZnO has usually been attributed to native point defects, such as oxygen vacancy (V_O) or zinc interstitial (Zn_I). However, this arguments is based on indirect evidence, e.g. the electrical conductivity increases as the oxygen partial pressure decreases, and the role of native point defects as sources of conductivity are only hypotheses that are not supported by experimental observations [19]. Nowadays H atoms are thought as the background donors that mainly responsible for the *n*-type conductivity of un-doped ZnO because of its lower formation energy of H^+ than H^- and the low activation energy. However, no matter which statement is true, it is undeniable that the native defects can strongly influence the optical property of ZnO which induce the green or yellow defect band in the luminescence of ZnO.

The group III elements Al, Ga, and In are donor dopants in ZnO, and can produce high electron concentration larger than 10^{20} cm^{-3} [20,21]. This high carrier concentration and low resistivity make it possible to apply as transparent conducting oxide (TCO).

Stimulated emission in ZnO

Optically pumped stimulated emission (SE) of ZnO has been observed in many researches. The efficient lasing (or low stimulated emission threshold) of excitonic emission can be attributed to the larger exciton binding energy compared to other wide band gap semiconductors. Exciton-exciton scattering-induced stimulated emission is very important for the realization of low-threshold lasers since it occurs at a threshold lower than that for the electron hole plasma (EHP) recombination.

In the intermediate excitation density regime emissions due to biexcitonic, exciton-exciton, and exciton-carrier interactions may be observed. The inelastic collision between the excitons results in an excitation of exciton into a higher state and a photon, as shown in Fig.1.3, with energy [22]:

$$E_n = E_{ex} - E_B^{ex}\left(1 - \frac{1}{n^2}\right) - \frac{3}{2}k_B T \qquad (n = 2,3,4,\ldots,\infty) \tag{1.1}$$

where E_{ex} is the free exciton energy, E_B^{ex} is the binding energy of the exciton (60 meV for ZnO), n is the quantum number of the envelope function, and $k_B T$ is the thermal energy.

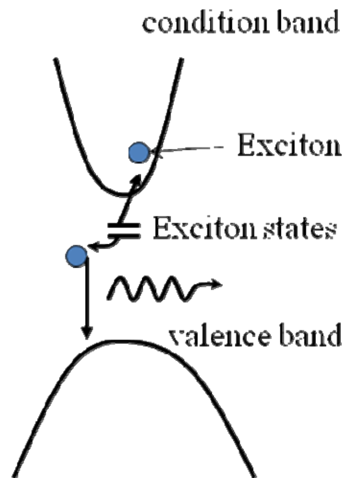

Figure 1.3 the band diagram of excion-exciton scattering. After the inelastic collision between the excitons, one is excited into a higher state and the other is transformed into a photon.

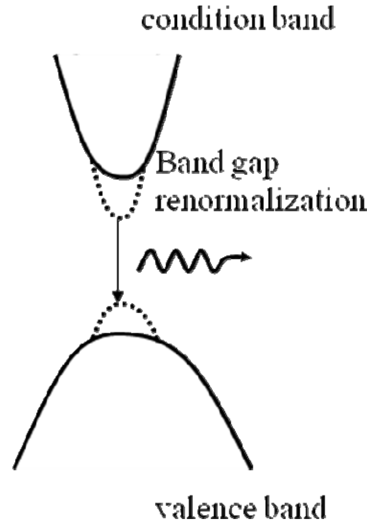

Figure 1.4 the band diagram of band gap renormalization induced by many body effect as the electron-hole concentration exceeds the Mott density.

At very high excitation intensities, an EHP forms beyond the “Mott density’’, which is calculated using

$$n_M = \frac{k_B T}{2a_B^3 E_B^{ex}} \tag{1.2}$$

where the exciton Bohr radius a_B =1.8Å for ZnO. And with the excitation intensity increase, the shirking of the band gap due to the many body effect causes the band gap renormalization (cf. to Fig.1.4). Therefore, red shift of the characteristic peak of EHP can be observed in the PL spectrum after the excited carrier density exceeds the Mott density. Consequently, the stimulated emission originating from exciton interactions and/or EHP recombination can be observed depend on the excitation intensity and the quality of the samples.

1.4 Franz-Keldysh Effect [24]

The energy band profile tilts along the direction of the electric field if a uniform electric field present in the semiconductor, as shown in Fig.1.5 In the presence of the

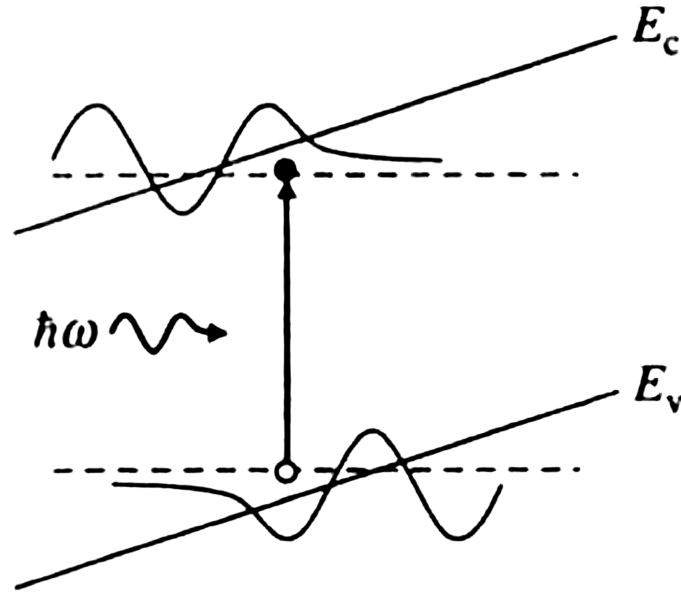

Figure 1.5 Franz-Keldysh effect or photon-assisted absorption in a bulk semiconductor with a uniform electric field bias. [24]

electric field, the absorption can occur slightly below the band gap because of the tunneling effect. The wave function for the conduction band electron can penetrate through the band gap, and so does the hole wave function. Therefore, an absorption tail below the band gap exists. The absorption spectrum above the band edge shows an oscillatory behavior as a function of the photon energy due to the wave nature of the electron and hole wave functions in the presence of the biased electric field (Fig.1.6. The Schrodinger equation for the wave function $\phi(\mathbf{r})$ is

$$\left[-\frac{\hbar^2}{2m_r^*}\nabla^2 + e\mathbf{F}\cdot\mathbf{r}\right]\phi(\mathbf{r}) = E\phi(\mathbf{r}) \tag{1.3}$$

$\mathbf{F}$ is the applied electric field in z direction, $\mathbf{F} = \hat{z}F$. Because the potential energy eFz is independent of x and y, the wave function is plane-wave like in the x-y plane, and it can be written in the form

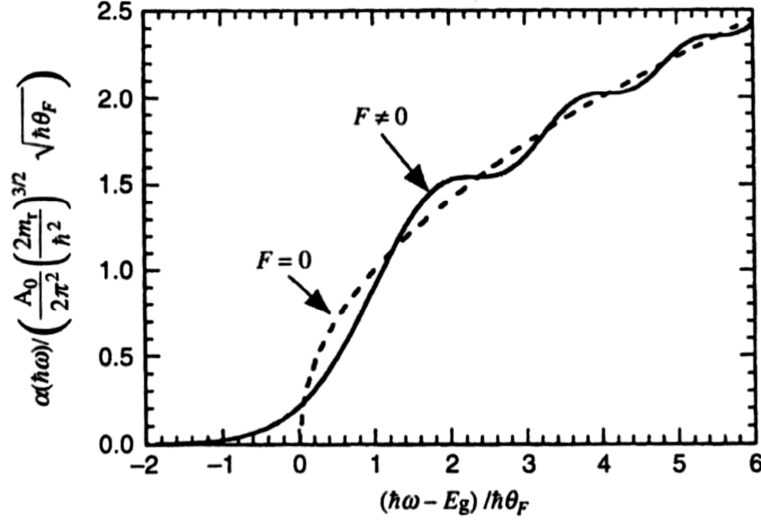

Figure 1.6 Absorption spectrum for a finite field F$\neq$0 (solid line). The dashed line is the free electron and hole absorption spectrum without an applied electric field (F=0). [24]

$$\phi(\mathbf{r}) = \frac{e^{ik_x x + ik_y y}}{\sqrt{A}} \phi(z) \tag{1.4}$$

where A is the normalization constant. Therefore, the z-dependent wave function $\phi(z)$ satisfies

$$\left[-\frac{\hbar^2}{2m_r^*} \frac{d^2}{dz^2} + eFz \right] \phi(z) = E_z \phi(z). \tag{1.5}$$

The total energy E is related to E_z for the z-dependent wave function

$$E = \frac{\hbar^2}{2m_r^*} \left(k_x^2 + k_y^2 \right) + E_z. \tag{1.6}$$

The solutions of the Schrodinger Eq. (1.5) are Airy functions Ai(Z) and Bi(Z), and Z is the function of z as following

$$Z = \left(\frac{2m_r^* eF}{\hbar^2} \right)^{1/3} \left(z - \frac{E_z}{eF} \right) \tag{1.7}$$

However, because the wave function has to decay as z approaches $+\infty$, the Airy function Ai(Z) has to be chosen. Therefore, the wave function satisfying the

normalization condition is

$$\phi_{E_z}(z)=\left(\frac{2m_r^*}{\hbar^2}\right)^{1/3}\frac{1}{(eF)^{1/6}}Ai\left[\left(\frac{2m_r^*eF}{\hbar^2}\right)^{1/3}\left(z-\frac{E_z}{eF}\right)\right]. \tag{1.7}$$

The absorption spectrum can be obtained by summing over all the quantum states with the overlapping between conduction and valance band wave functions. And can be written as following

$$\alpha(\hbar\omega)=\frac{A_0}{2\pi}\left(\frac{2m_r^*}{\hbar^2}\right)^{3/2}\sqrt{\hbar\theta_F}\int_{\eta}^{\infty}Ai^2(\tau)d\tau \tag{1.8}$$

where

$$A_0=\frac{\pi e^2\left|\hat{e}\cdot\mathbf{p}_{cv}\right|}{n_r c\varepsilon_0 m_0^2\omega} \tag{1.9}$$

and

$$\hbar\theta_F=\left(\frac{\hbar^2e^2F^2}{2m_r^*}\right)^{1/3}, \qquad \tau=-\frac{E_z}{\hbar\theta_F}, \qquad \eta=\frac{E_g-\hbar\omega}{\hbar\theta_F}.$$

In conclusion, the Franz-Keldysh oscillation phenomena in the absorption spectrum above the band gap and the exponentially decaying behavior below the band gap will be obtained if the electric field is present in the semiconductor.

Reference

[1] J. F. Muth, J. H. Lee, I. K. Shmagin, R. M. Kolbas, H. C. Casey, Jr., B. P. Keller, U. K. Mishra, and S. P. DenBaars, Appl. Phys. Lett. **71**, 2572 (1997).

[2] J. M. Yuk, J. Y. Lee, J. H. Jung, T. W. Kim, D. I. Son, W. K. Choi, Appl. Phys. Lett. **90**, 031907 (2007).

[3] S.-H. Lim, D. Shindo, H.-B. Kang and K. Nakamura, J. Vac. Sci. Technol. B **19**.(2), 506 (2001).

[4] A. Setiawan, Z. Vashaei, M. W. Cho, T. Yao, H. Kato, M. Sano, K. Miyamoto, I. Yonenaga H. J. Ko, J. Appl. Phys. **96**, 3763 (2004).

[5] S. H. Lim, J. Washburn, Z. Liliental-Weber, and D. Shindo, J. Vac. Sci. Technol. A **19**, 2601 (2001).

[6] V. Sallet, C. Thiandoume, J.F. Rommeluere, A. Lusson, A. Rivie`re, J.P. Rivie`re, O. Gorochov, R. Triboulet, V. Mun˜oz-Sanjose´, Mater. Lett. **53**, 126 (2002).

[7] C. M. Hou, K. K. Huang, Z. M. Gao, X. S. Li, S. H. Feng, Y. T. Zhang, and G. T. Du, Chem. Res. Chinese. U. **22**, 552 (2006).

[8] C. Y. Liu, B. P. Zhang, N.T. Binh, Y. Segawa, Appl. Phys. B **79**, 83 (2004).

[9] W. Y. Shiao, C. Y. Chi, S. C. Chin, C. F. Huang, T. Y. Tang, Y. C. Lu, Y. L. Lin, L. Hong, F. Y. Jen, C. C. Yang, B. P. Zhang, and Y. Segawa, J. Appl. Phys. **99**, 054301 (2006).

[10] J. Hu and R. G. Gordon, *J. Appl. Phys.*, **71**, 880 (1992)

[11] K. Minegishi,Y. Koiwai,Y. Kikuchi, K. Yano, M. Kasuga and A. Shimizu, Jpn. J. Appl. Phys. **36**, L1453 (1997)

[12] Y.G. Wang, N. Ohashi, Y. Wada, I. Sakaguchi, T. Ohgaki and H. Haneda, J, Appl. Phys. **100**, 023524 (2006)

[13] Carcia P. F., McLean R. S., Reilly M. H. and Nunes G., Appl. Phys. Lett. **82** 1117 (2003)

[14] Chen L.Y., Chen W.H., Wang J.J., Hong F. C.N. and Su Y.K., Appl. Phys. Lett. **85**, 5628 (2004)

[15] Hsieh H.H. and Wu C.C., *Appl. Phys. Lett.* **89** 041109 (2006)

[16] C. Yuen, S. F. Yu, E. S. P. Leong, H. Y. Yang, S. P. Lau, and H. H. Hng, IEEE J. Quantum Electron. **41**, 970 (2005)

[17] Y. G. Wang, S. P. Lau, H. W. Lee, S. F. Yu, B. K. Tay, X. H. Zhang, K. Y. Tse and H. H. Hng, J. Appl. Phys. **94**, 1597 (2003)

[18] A. Kobayashi, O. F. Sankey, S. M. Volz, and J. D. Dow, Phys. Rev. B **28**, 935 (1983).

[19] A. Janotti and C. G Van de Walle, Rep. Prog. Phys. **72**, 126501 (2009)

[20] K-K. Kim, S. Niki, J-Y. Oh, J-O. Song, T-Y. Seong, S-J. Park, S. Fujita, and S-W. Kim, J. Appl. Phys. **97**, 066013 (2005).

[21] T. Makino, Y. Segawa, S. Yoshida, A. Tsukazaki, A. Ohtomo, and M. Kawasaki, Appl. Phys. Lett. **85**, 759 (2004).

[22] C. Klingshirn, Phys. Stat. Sol. (b) **71**, 547 (1975).

[23] Y. Chen, N. T. Tuan, Y. Segawa, H.-J. Ko, S.-K. Hong, and T. Yao, Appl. Phys. Lett. **78**, 1469 (2001).

[24] S. L. Chuang, “Physics of Photonic Devices”, 2ed, Wiley, New Jersey, ch14, 2009.

Chapter 2

Structure of ZnO epilayer grown by atomic layer deposition on the sapphire substrate

2.1 Introduction

Zinc oxide (ZnO) has attracted considerable attention as a promising material for ultraviolet (UV) photonic devices such as light-emitting diodes and lasers [1-8]. ZnO also has numerous applications in transparent electronics, piezoelectric devices, gas sensors, solar cells, spin electronics, *etc*. [9]. The large excitonic binding energy (60 meV) of ZnO suggests that it has excellent UV light emission properties. ZnO also has several other advantages: amenability to conventional wet chemical etching, relatively low material costs, long-term stability, environmental friendliness, biocompatibility, and excellent radiation resistance.

Many techniques have been used to grow high-quality ZnO films, including molecular beam epitaxy (MBE) [10-14], metal-organic chemical vapor deposition (MOCVD) [15-18], chemical vapor deposition (CVD) [19,20], pulsed laser deposition (PLD) [21], radio-frequency magnetron sputtering (RFMS) [22-24], and filtered cathodic vacuum arc technique [25,26]. Lim *et al.* reported that ZnO films grown on the (0001) sapphire (c-Al_2O_3) at 200-275°C by electron cyclotron resonance-assisted MBE were basically single crystals, which comprised subgrains with 15~150 nm in size and accompanied by threading dislocations [12]. Generally, a lot of columnar grains were embedded in the ZnO films grown by MOCVD [15-18]. PLD and RFMS may be the most popular techniques for preparation of ZnO films, but they usually require a high growth temperature (above 350°C or more).

Atomic layer deposition (ALD) is another noteworthy method of growing high-quality ZnO films [27-29]. Unlike the other methods such as CVD, ALD proceeds the reactions solely on the surface of the substrate, leading to self-limiting and layer-by-layer growth. ALD offers many advantages, including easy and accurate thickness control, excellent conformality, high uniformity over a large area, good reproducibility, low defect density, pinhole-free structures, and low deposition temperatures. Recently, Wójcik *et al.* have examined how to control the preferred orientation of polycrystalline ZnO thin films grown by ALD on the c-Al_2O_3, lime glass, and (001) and (111) Si substrates at 230-400°C [30]. They have also reported that the ALD ZnO thin films grown on Si substrates at low temperatures (90-200°C) are high-quality polycrystalline with surface roughness of 1 4 nm [31,32]. In this paper, we demonstrate a high-quality ZnO epilayer grown on the c-Al_2O_3 substrate using the ALD technique, followed by high-temperature rapid thermal annealing (RTA). The resulting ZnO film exhibited optically-pumped stimulated emission with a low threshold intensity, implying the high crystalline quality revealed by X-ray diffraction (XRD) and transmission electron microscopy (TEM).

2.2 Sample preparation

A ZnO epilayer was deposited on the c-Al_2O_3 substrate (2 inch in diameter) at a low deposition temperature of 180°C by ALD. We used a Cambridge NanoTech Savannah 100 ALD system, with a reactor chamber of 4 inch in diameter and 5mm in height. Two precursors, $Zn(C_2H_5)_2$ (Diethylzinc, DEZn) and H_2O vapor, were carried in by a N_2 flow. The following reactions proceed on the surface:

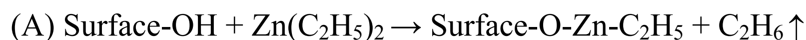
(A) Surface-OH + $Zn(C_2H_5)_2 \rightarrow$ Surface-O-Zn-C_2H_5 + $C_2H_6\uparrow$

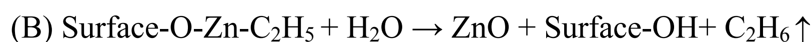
(B) Surface-O-Zn-C_2H_5 + $H_2O \rightarrow$ ZnO + Surface-OH+ $C_2H_6\uparrow$

The ALD process consisted of a number of identical cycles and repeated the reactions in an ABAB… sequence. Each ALD cycle contained the following sequence: (A) Pulsing time of DEZn was 0.01 s, followed by N_2 purge for 5 s, and (B) Pulsing time of H_2O was 0.1 s, followed by N_2 purge for 5 s. These precursor pulse duration and purging time were set as the most appropriate condition for ZnO deposition in the ALD system used in this experiment. Each ALD cycle deposited ~0.18 nm of ZnO. After deposition, the films were treated by RTA at 950°C for 5 min in a nitrogen atmosphere to improve the crystal quality.

2.3 Experimental procedure

The crystalline structure of the ZnO epilayer was characterized by XRD and TEM. A PANalytical X'Pert PRO diffractometer with a wavelength of 1.54Å was used for the XRD measurement. TEM images were recorded using a Tecnai 30 electron microscope equipped with a lens of Cs=1.2 mm and operated at 300 keV. The specimens for TEM observation were prepared by mechanical polishing and ion milling with a Gatan Precision Ion Polish System Model-691. Photoluminescence (PL) spectra were measured in a standard backscattering configuration by collecting the emitted light from top surface of the sample. A continuous-wave He-Cd laser (λ= 325 nm) and a pulsed Nd-YAG laser (λ= 266 nm, 10 ns pulse width, 15 Hz repetition rate) were used as the excitation sources to measure the spontaneous emission and stimulated emission of the ZnO epilayer at room temperature.

2.4 Results and Discussion

2.4.1 X-ray diffraction

Figure 2.1 shows the XRD pattern of the ZnO epilayer, indicating that it was preferentially oriented with respect to the c-Al_2O_3 substrate with the relation of

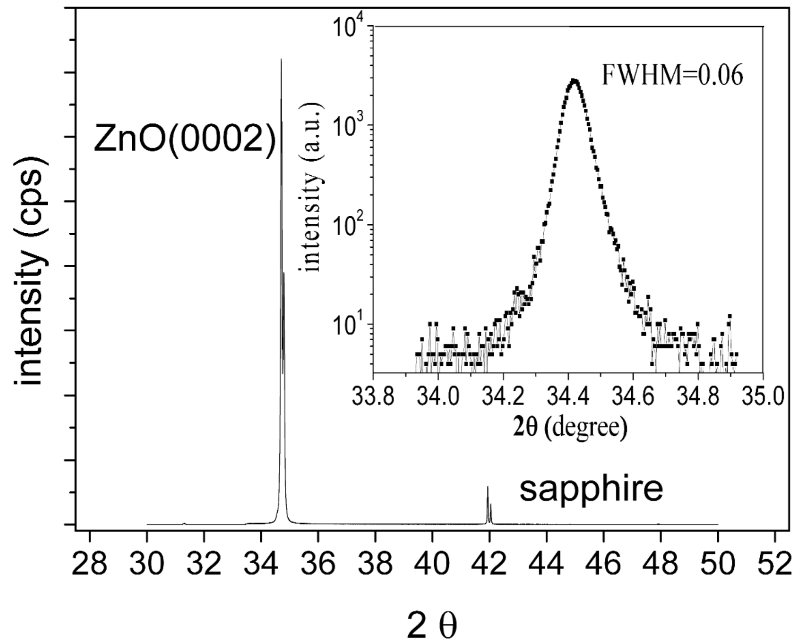

Figure 2.1 X-ray diffraction pattern of the ZnO epilayer grown on the *c*-Al_2O_3 substrate.

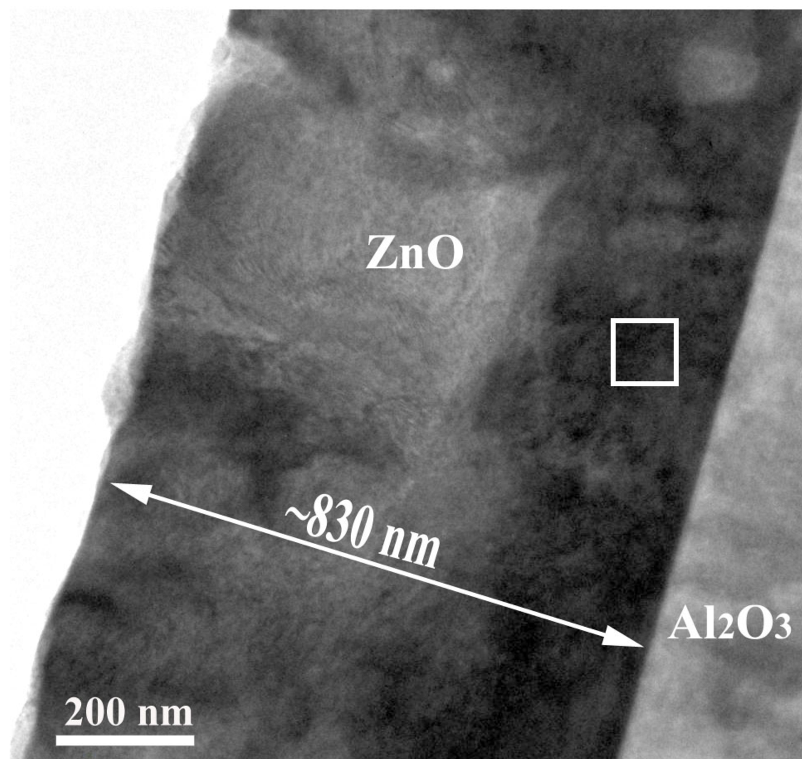

Figure 2.2 Cross-sectional transmission electron microscopy (TEM) image of the ZnO epilayer grown on the *c*-Al_2O_3 substrate.

(0001)ZnO//(0001)Al_2O_3. The XRD θ-2θ scan (the inset of Fig. 2.1) exhibited a sharp ZnO (0002) peak with a full-width at half-maximum (FWHM) width of 0.06°. This reveals high crystallinity with the *c*-axis orientation of the ZnO epilayer.

2.4.2 Cross-sectional TEM

Figure 2.2 shows a cross-sectional TEM image of the ZnO epilayer about 830 nm thick on the *c*-Al_2O_3 substrate. In some deposition technology, the higher growth rate along the *c* axis than other directions results in a columnar morphology in ZnO [11-18]. However, the columnar structures were not observed in the ZnO epilayer grown by ALD and followed by RTA treatment. This is attributable to the layer-by-layer growth and the low deposition temperature of 180°C in ALD. The RTA treatment recrystallized the granular particles with strained lattices in the as-deposited ZnO film to a highly crystalline single crystal with the preferred *c*-axis orientation.

2.4.3 High resolution TEM

Figure 2.3 displays a high-resolution (HR) TEM mage of an area including the ZnO and *c*-Al_2O_3 substrate. Insets, **a**, **b**, **c** and **all** at the right-hand side of the figure**,** present the computer diffractograms (FFT images) of the areas indicated by **a**, **b**, and **c** and of the whole area in the HRTEM image, respectively. Diffractogram **c** reveals that the ZnO is oriented with the $[0\bar{1}10]$ axis parallel to the incident beam and the [0001] axis normal to the film surface. The interfacial area **b** exhibiting brighter contrast can be also identified as ZnO crystal with almost the same orientation with the crystal in **c**. The difference in contrast between **c** and **b** might be caused by very small difference in the diffraction condition. Thus, the dark area **c** and the bright area **b** are almost similar in the crystal structure, although they are not the same because the lattices of interfacial area **b** are more distorted under the influence of the

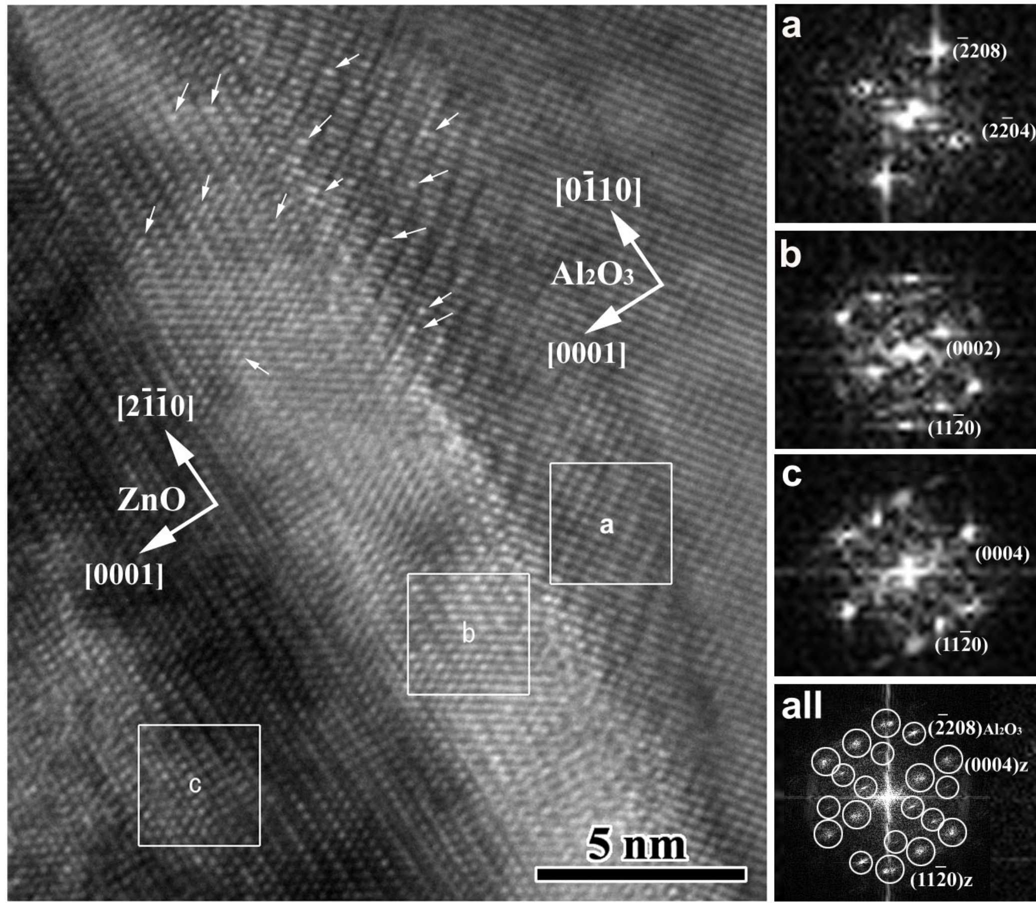

Figure 2.3 High-resolution TEM (HRTEM) image of an area including the ZnO/Al_2O_3 interface. Computer diffractograms are of the small areas indicated by a, b, and c and the whole area (all). Indexes in diffractogam a correspond to the lattice fringes of Al_2O_3 crystal and indexes in diffractograms b and c correspond to the lattice fringes of ZnO crystal. In the diffractogram all, the spots enclosed by large circles come from ZnO and the spots enclosed by small circles originate from Al_2O_3.

c-Al_2O_3 substrate lattice as seen in the HRTEM image. The Al_2O_3 crystal including the area **a** is nearly oriented with the $[2\bar{1}\bar{1}0]$ axis parallel to the incident beam and the [0001] axis normal to the film surface, which indicates that the ZnO crystal was grown in the epitaxial relation with respect to the *c*-Al_2O_3: $[0001]_{ZnO}//[0001]_{Al_2O_3}$ and $[0\bar{1}10]_{ZnO}//\ [2\bar{1}\bar{1}0]_{Al_2O_3}$. The lattice of ZnO crystal in the interfacial area is conjugated rather homogeneously and coherently with the lattice of *c*-Al_2O_3 crystal, with very few threading dislocations (also sees Fig. 2.2). It should be noted that the threading dislocations used to occur in the ZnO crystals grown by other methods due

to a lattice misfit as large as 18 % between ZnO and *c*-Al_2O_3 [12]. The ZnO grown on *c*-Al_2O_3 by ALD might relax the misfit by distorting its lattice in the interfacial layer. Consequently, the ZnO crystal developed to the single crystal as seen in Fig. 2.2, in a short annealing time of 5 min. Figure 2.4 shows an HR-TEM image of the ZnO epilayer, whose area is indicated by the square in Fig. 2.2. The image reveals that the crystal is a nearly perfect ZnO crystal although some lattice distortion still appears as the traces of coalescence growth between the granular particles in the as-deposited ZnO film.

The spots in the diffractogaram of the whole area in Fig. 2.3, **all**, can be indexed as the spots form the ZnO and Al_2O_3 lattice fringes. We cannot recognize any other crystal in our specimen although Wang *et al*. identified Al_2ZnO_4 phase in a TEM image at the interface between ZnO and Al_2O_3 [21]. The Al_2ZnO_4 phase might be formed by the reaction of ZnO and Al_2O_3 during PLD at a high growth temperature of 600°C and a long annealing treatment at 900 °C for 2 h. In this study, the ALD growth temperature was as low as 180°C and the post-deposition annealing treatment was short (950°C for 5 min). However, we can see extraordinarily bright spots (some examples of which are indicated by arrowheads in Fig. 2.3) in the lattice fringes in the HRTEM image, which may be ascribed to the substituted Al atoms in the interfacial ZnO layer and the Al vacancies in the Al_2O_3 crystal near the interface. Therefore, it is reasonable to assume that the Al atoms might diffuse from the substrate to the ZnO crystal during the RTA treatment.

2.4.4 Optical property

The high crystallinity shown in the XRD and TEM measurements suggests good light emission properties of the ZnO epilayer grown by ALD. Figure 2.5 shows the

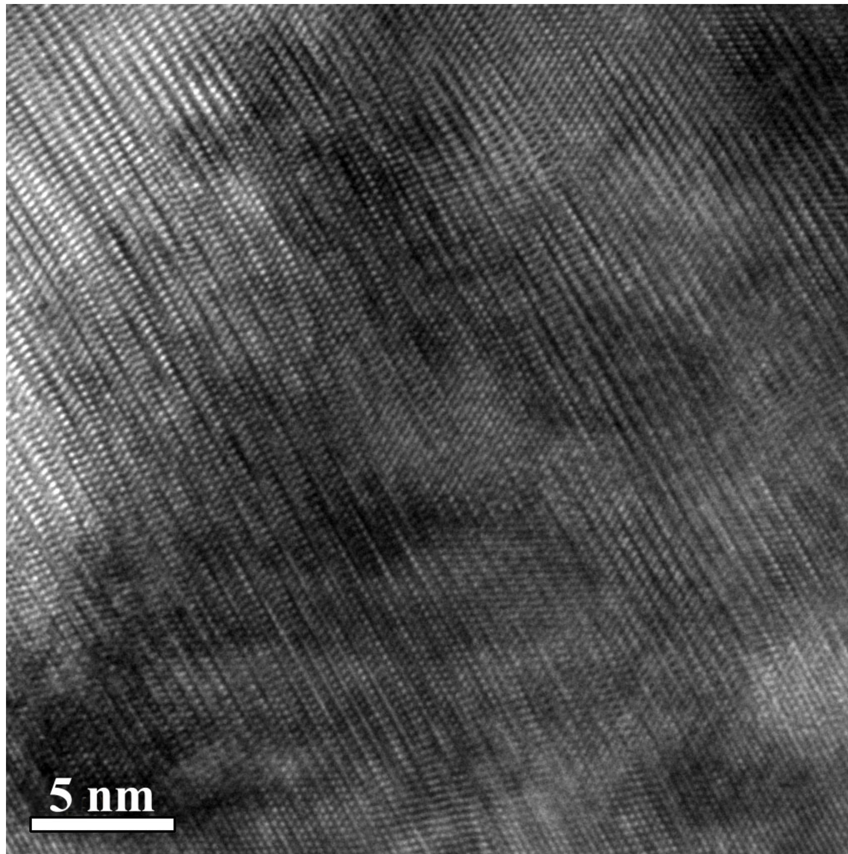

Figure 2.4 HRTEM image of the area enclosed by a square in Fig. 2.2.

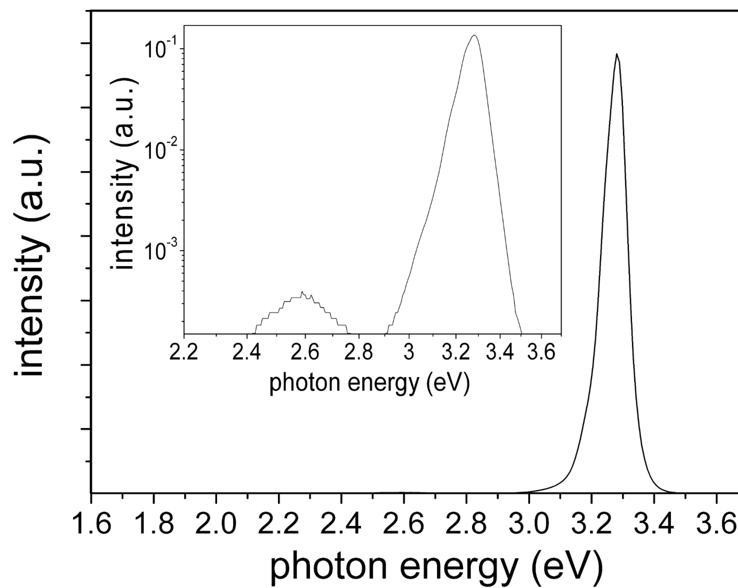

Figure 2.5 Spontaneous emission PL spectrum of the ZnO epilayer pumped by a CW He-Cd laser at room temperature. The inset is the plot of the same PL spectrum in the logarithm scale.

spontaneous emission PL spectrum of the ZnO epilayer at room temperature. The PL spectrum exhibited a strong near-band-edge (NBE) emission at 3.28 eV, nearly free of the defect-related band. The inset of Fig. 2.5 presents the same PL spectrum in logarithm scale, indicating a very weak defect-related band at 2.57 eV associated with the oxygen vacancy (V_O) [8]. It can be observed that the intensity of the NBE emission (3.28 eV) is about two orders of magnitude larger than that of the defect-related band (2.57 eV).

2.5 Summary

This study presents the structure and spontaneous emission of the ZnO epilayer grown on c-Al_2O_3 by ALD and treated by post-deposition RTA process. XRD measurement indicates that the ZnO epilayer was highly c-axis orientated. The cross-sectional TEM images show that the columnar structures were not formed in the ZnO epilayer, which may be attributed to the layer-by-layer growth and low deposition temperature of ALD. The HRTEM images display that a distorted ZnO layer exists at the ZnO/sapphire interface. Because of the relaxation of the misfit by the interfacial distorted layer coupled with the layer-by-layer growth of ALD, no obvious threading dislocations appeared in the TEM images even though the lattice mismatch between ZnO and c-Al_2O_3 is up to 18 %. A dominant UV emission at 3.28 eV with a negligible defect band was shown in the spontaneous emission PL spectrum ascribed the good crystalline quality of the ZnO epilayer, indicating that the ZnO epilayers grown by the ALD technique are applicable to next-generation UV photonic devices.

Reference

[1] A. Tsukazaki, A. Ohtomo, T. Onuma, M. Ohtani, T. Makino, M. Sumiya, K. Ohtani, S. F. Chichibu, S. Fuke, Y. Segawa, H. Ohno, H. Koinuma, and M. Kawasaki, Nat. Mater. 4 (2005) 42.

[1] X. Li. Guo, J. H. Choi, H. Tabata, and T. Kawai, Jpn. J. Appl. Phys. 40 (2001) L177.

[2] Y. Ryu, T. S. Lee, J. A. Lubguban, H. W. White, B. J. Kim, Y. S. Park, C. J. Youn, Appl. Phys. Lett. 88 (2006) 241108.

[3] W. Z. Xu, Z. Z. Ye, Y. J. Zeng, L. P. Zhu, B. H. Zhao, L. Jiang, J. G. Lu, and H. P. He, Appl. Phys. Lett. 88 (2006) 173506.

[4] S. J. Jiao, Z. Z. Zhang, Y. M. Lu, D. Z. Shen, B. Yao, J. Y. Zhang, B. H. Li, D. X. Zhao, X. W. Fan and Z. K. Tang, Appl. Phys. Lett. 88 (2006) 031911.

[5] Ya. I. Alivov, E. V. Kalinina, A. E. Cherenkov, D. C. Look, B. M. Ataev, A. K. Omaev, M. V. Chukichev, and D. M. Bagnall, Appl. Phys. Lett. 83 (2003) 4719.

[6] D. C. Look, Mater. Sci. Eng. B 80 (2001) 383.

[7] Ü. Özgür, Ya. I. Alivov, C. Liu, A. Teke, M. A. Reshchikov, S. Doğan, V. Avrutin, S.-J. Cho, and H. Morkoçd, J. Appl. Phys. 98 (2005) 041301.

[8] C. Jagadish and S. J. Pearton, Zinc Oxide Bulk, Thin Films and Nanostructures: Processing, Properties, and Application, Elsevier Science, 2006.

[9] Y. Chen, D. Bagnall, and T. Yao, Mater. Sci. Eng. B 75 (2000) 190.

[10] J. M. Yuk, J. Y. Lee, J. H. Jung, T. W. Kim, D. I. Son, W. K. Choi, Appl. Phys. Lett. 90 (2007) 031907.

[11] S.-H. Lim, D. Shindo, H.-B. Kang and K. Nakamura, J. Vac. Sci. Technol. B 19 (2) (2001) 506.

[12] A. Setiawan, Z. Vashaei, M. W. Cho, T. Yao, H. Kato, M. Sano, K. Miyamoto, I. Yonenaga H. J. Ko, J. Appl. Phys. 96 (2004) 3763.

[13] S. H. Lim, J. Washburn, Z. Liliental-Weber, and D. Shindo, J. Vac. Sci. Technol. A 19 (2001) 2601.

[14] V. Sallet, C. Thiandoume, J.F. Rommeluere, A. Lusson, A. Rivie`re, J.P. Rivie`re, O. Gorochov, R. Triboulet, V. Mun˜oz-Sanjose´, Mater. Lett. 53 (2002) 126.

[15] C. M. Hou, K. K. Huang, Z. M. Gao, X. S. Li, S. H. Feng, Y. T. Zhang, and G. T. Du, Chem. Res. Chinese. U. 22 (2006) 552.

[16] C. Y. Liu, B. P. Zhang, N.T. Binh, Y. Segawa, Appl. Phys. B 79 (2004) 83.

[17] W. Y. Shiao, C. Y. Chi, S. C. Chin, C. F. Huang, T. Y. Tang, Y. C. Lu, Y. L. Lin, L. Hong, F. Y. Jen, C. C. Yang, B. P. Zhang, and Y. Segawa, J. Appl. Phys. 99 (2006) 054301.

[18] J. Hu and R. G. Gordon, J. Appl. Phys. 71 (1992) 880.

[19] K. Minegishi,Y. Koiwai,Y. Kikuchi, K. Yano, M. Kasuga and A. Shimizu, Jpn. J. Appl. Phys. 36 (1997) L1453.

[20] Y.G. Wang, N. Ohashi, Y. Wada, I. Sakaguchi, T. Ohgaki and H. Haneda, J, Appl. Phys. 100 (2006) 023524.

[21] Carcia P. F., McLean R. S., Reilly M. H. and Nunes G., Appl. Phys. Lett. 82 (2003) 1117.

[22] Chen L.Y., Chen W.H., Wang J.J., Hong F. C.N. and Su Y.K., Appl. Phys. Lett. 85 (2004) 5628.

[23] Hsieh H.H. and Wu C.C., Appl. Phys. Lett. 89 (2006) 041109

[24] C. Yuen, S. F. Yu, E. S. P. Leong, H. Y. Yang, S. P. Lau, and H. H. Hng, IEEE J. Quantum Electron. 41 (2005) 970

[25] Y. G. Wang, S. P. Lau, H. W. Lee, S. F. Yu, B. K. Tay, X. H. Zhang, K. Y. Tse and H. H. Hng, J. Appl. Phys. 94 (2003) 1597

[26] M. Ritala and M. Leskela, Nanotechnology 10 (1999) 19.

[27] L. Niinistö, J. Päiväsaari, J. Niinistö, M. Putkonen, and M. Nieminen, Phys. Stat. Sol. (a) 201 (2004) 1443.

[28] J. Lim, K. Shin, H. W. Kim and C. Lee, J. Lumin. 109 (2004) 181.

[29] A. Wojcik, M. Godlewski, E. Guziewicz, R. Minikayev, W. Paszkowicz, J. Crystal Growth 310 (2008) 284.

[30] E. Guziewicz, I. A. Kowalik, M. Godlewski, K. Kopalko, V. Osinniy, A. Wójcik , S. Yatsunenko, E. Usakowska., W. Paszkowicz and M. Guziewicz, J. Appl. Phy. 103 (2008) 033515.

[31] I. A. Kowalik, E. Guziewicz, K. Kopalko, S. Yatsunenko, M. Godlewski and A. Wojcik, Acta Phys. Pol. A 112 (2007) 401.

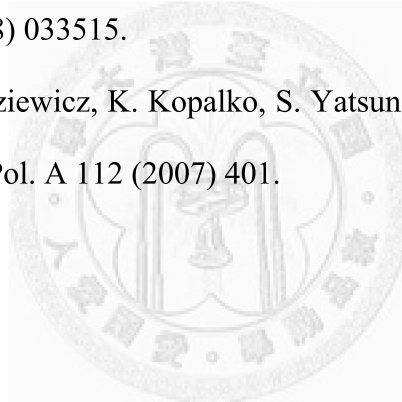

Chapter 3

Stimulated Emission in ZnO and ZnO:Al Thin Films Grown by Atomic Layer Deposition

3.1 Introduction

The ALD technique was used to grow ZnO and aluminum doped ZnO (ZnO:Al) films on sapphire substrates. High-temperature post-deposition annealing and an Al_2O_3 surface passivation layer deposited by ALD improve the light-emission characteristics of ZnO. This chapter discusses the room-temperature stimulated emission with a low threshold value in ZnO films grown by ALD.

The doping of ZnO with group-III impurities such as Al shows improved conductivity. Recently, lowering of stimulated emission threshold in ZnO by doping with thermally diffused Al had been investigated [1]. In this chapter, the ALD technique and the high-temperature post-deposition annealing were employed to prepare the Al-doped ZnO (ZnO:Al) films with Al doping percentages of 2% and 4%. The threshold of stimulated emission was found to decrease with the increasing Al doping percentage and a low lasing threshold in the ZnO:Al films was achieved at room temperature.

In order to observe the affect of random lasing in the reduction of the stimulated emission threshold of ZnO:Al films, the stimulated emission of two different kinds of doping configuration of 6% ZnO:Al thin film is investigated. Two thresholds were observed in the integrated-intensity versus excitation plot. The two thresholds were identified as threshold of random lasing and threshold of electron-hole plasma.

3.2 Stimulated emission in undoped ZnO thin film

3.2.1 Sample preparation

ZnO thin films were deposited on a (0002)-oriented sapphire substrate held at 180°C, with two precursors, $Zn(C_2H_5)_2$ (Diethylzinc, DEZn) and H_2O, carried in by a N_2 flow:

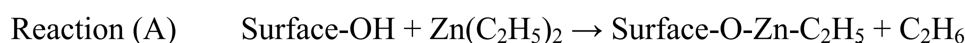
Reaction (A) Surface-OH + $Zn(C_2H_5)_2 \rightarrow$ Surface-O-Zn-C_2H_5 + C_2H_6

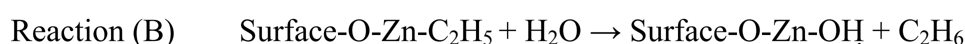
Reaction (B) Surface-O-Zn-C_2H_5 + $H_2O \rightarrow$ Surface-O-Zn-OH + C_2H_6

The ZnO films were deposited by repeating these reactions in an ABAB… sequence. Reactions A and B comprise one ALD cycle. Each ALD cycle contains the following sequence: DEZn, 0.01 sec.→ N_2 purge, 5 sec.→ H_2O, 0.1 sec.→ N_2 purge, 5 sec., and deposited ~1.8 Å of ZnO. The ZnO films grown by ALD in this study were approximately 200 nm thick. After deposition, the films were annealed using a furnace at 1000°C for 2 hours in a nitrogen atmosphere to improve crystal quality. Subsequently, a 10-nm Al_2O_3 film was deposited on top of the ZnO films by ALD at a substrate temperature of 300°C. $Al(CH_3)_3$ (Trimethylaluminum, TMA) and H_2O are the precursors for Al_2O_3 deposition through the following chemical reactions:

Reaction (C) Surface-OH + $Al(CH_3)_3 \rightarrow$ Surface-O-$Al(CH_3)_2$ + CH_4

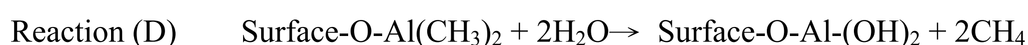
Reaction (D) Surface-O-$Al(CH_3)_2$ + $2H_2O \rightarrow$ Surface-O-Al-$(OH)_2$ + $2CH_4$

Pulse durations were 0.03 sec. for TMA, 0.1 sec. for H_2O, and 5 sec. for the N_2 purge. The Al_2O_3 thin film was utilized to passivate the surface and reduce unwanted nonradiative recombination at the surface.

3.2.2 Experiment procedure

The crystalline structure of the ZnO film was characterized by X-ray diffraction (XRD), and its photoluminescence (PL) was measured at room temperature using a fourth harmonic Q-switched Nd:YAG laser (wavelength = 266 nm, 10 ns pulse with 15 Hz repetition rate) as the excitation source. The PL spectra were measured in a standard backscattering configuration, where the light emission from the top surface of the sample was collected. The optical gain spectrum of the ZnO film was investigated using the variable stripe length (VSL) technique.

3.2.3 Crystal quality

Figure 3.1 shows the XRD measurement of the post-annealed ZnO film *without* the Al_2O_3 surface passivation layer. The appearance of a sharp ZnO (0002) peak reveals that the ZnO film has high crystallinity with c-axis orientation. Figure 3.2 shows that the full-width at half-maximum (FWHM) of the ZnO (0002) XRD peak decreases from 0.245° for the as-deposited film to 0.084° (the $K\alpha 1$ peak) for the post-annealed film, and the peak intensity is much higher for the post-annealed film. This demonstrates that the high-temperature post-annealing improves the crystal quality. The average grain sizes of the as-deposited and post-annealed films can be estimated by Scherrer's equation:

$$D = \frac{0.9\lambda}{B\cos\theta_B} \tag{3.1}$$

where D is the grain size, λ is the X ray wavelength, B is the FWHM of the diffraction peak, and θ_B is the Bragg diffraction angle. The average grain sizes of the as-deposited and post-annealed films were calculated to be 34 nm and 99 nm, respectively, indicating that the high-temperature post-annealing greatly increases the grain size.

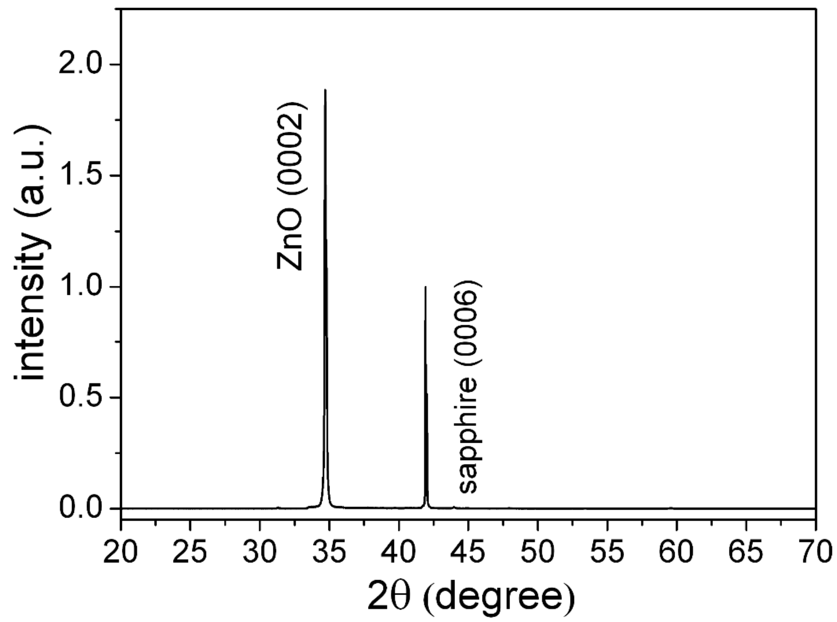

Figure 3.1 XRD pattern of the post-annealed ZnO film *without* the Al_2O_3 surface passivation layer.

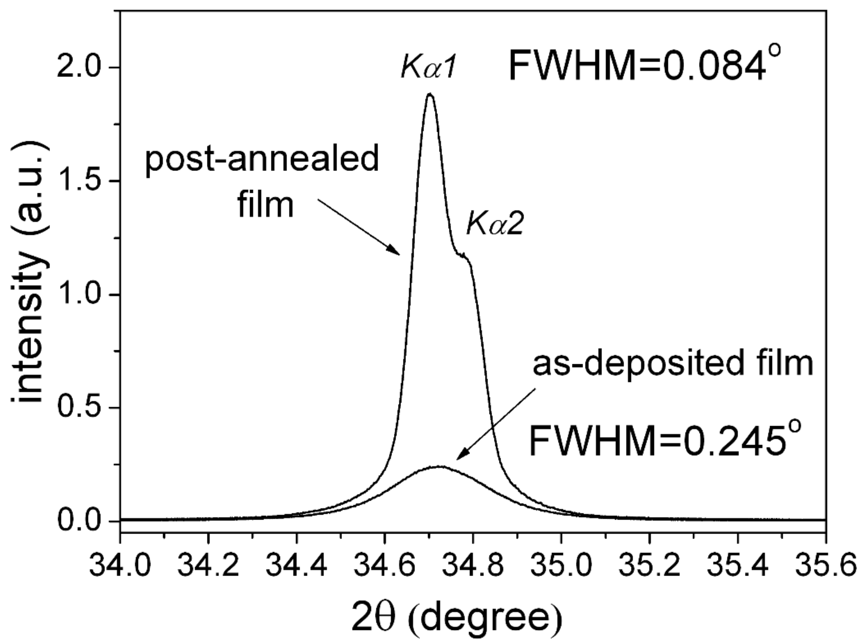

Figure 3.2 XRD patterns of the as-deposited and post-annealed ZnO films *without* the Al_2O_3 surface passivation layer.

3.2.4 Stimulated emission

Figure 3.3 shows the PL spectra at various excitation intensities of the post-annealed ZnO film with the Al_2O_3 surface passivation layer. As the inset in Fig. 3.3 indicates, the PL spectrum exhibited UV spontaneous emission at 380 nm with negligible defect-related band at an excitation intensity of 17.2 kW/cm^2. This UV emission may be attributed to the radiative recombination of free excitons [2]. When the film was excited at a pumping intensity of 39.5 kW/cm^2, a spectral peak associated with the exciton-exciton scattering appeared around 392 nm. In the exciton-exciton scattering process, one of the two excitons scatters into a higher energy state while the other exciton recombines radiatively to emit a photon with the energy given by [3,4]

$$E_n = E_{ex} - E_B^{ex}\left(1 - \frac{1}{n^2}\right) - \frac{3}{2}k_B T \tag{3.2}$$

where E_{ex} is the free exciton energy, E_B^{ex} is the binding energy of exciton, n is the

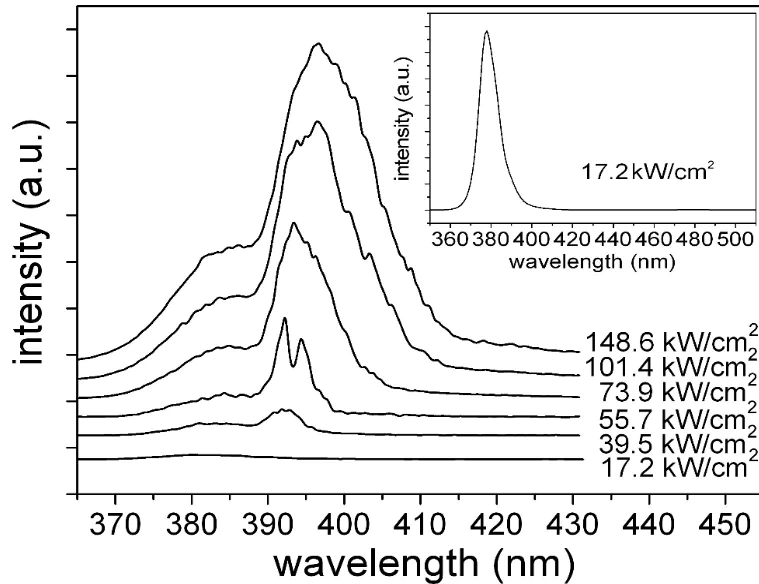

Figure 3.3 Room-temperature PL spectra of the post-annealed ZnO film *with* the Al_2O_3 surface passivation layer at various excitation intensities. The inset is the PL spectrum at an excitation intensity of 17.2 kW/cm^2.

quantum number of the excited exciton, and $k_B T$ is the thermal energy. The difference between E_{ex} and E_n ($n>>2$) according to Eq.(3.2) is 99 meV, which agrees well with the experimental result.

As the excitation intensity was increased to 55.7 kW/cm^2, Figure 3.3 shows that two spectral peaks appeared. The spectral peak at 392 nm corresponds to the exciton-exciton scattering process, and the spectral peak emerging at 395 nm is attributed to the electron-hole plasma (EHP) [3]. At high excitation intensities, the exciton concentration reaches the Mott density where the excitons overlap with each other, lose their individual character, and eventually become EHP. The Mott density in ZnO as estimated by Klingshirn et. al. is [5]

$$n_M^{ZnO} \approx 3 \times 10^{17}\ cm^{-3} \tag{3.3}$$

The exciton concentration n_p in the sample in this study can be estimated using the following expression [5]

$$n_p = \frac{I_{exc}\tau}{\hbar\omega_{exc} l} \tag{3.4}$$

where I_{exc} and $\hbar\omega_{exc}$ are the intensity and photon energy of the pumping light, and l is the film thickness. τ is the exciton lifetime, with a typical value of 300 ps [6]. At the excitation intensity $I_{exc} = 55.7\text{kW/cm}^2$, the exciton concentration estimated by Eq.(3.4) was approximately 1.12 $\times 10^{18}$ cm^{-3}, which is greater than the Mott density given by Eq.(3.3). Thus the EHP was formed and the emission from EHP was observed. A further increase in the excitation intensity causes an increase in the EHP concentration, which in turn contributes to the bandgap renormalization. As a result, the spectral peak associated with EHP gradually broadens and shifts toward longer wavelength. Since the diameter of the focused incident laser beam in this study was about 1 mm, which is much larger than the film thickness, the stimulated emission

likely resulted from amplified spontaneous emission (ASE) in the direction parallel to the film surface. This observed stimulated emission in the direction perpendicular to the film surface may be attributed to the scattering of the ASE propagating in the in-plane direction by the crystalline grains [2].

3.2.5 Al_2O_3 surface passivation

Figure 3.4 shows that the integrated PL intensity increases super-linearly with the excitation intensity. The appearance of the spectral peaks as well as the super-linear increase in the emission intensity with the excitation intensity indicate that the stimulated emission occurs at a low threshold intensity of 35.1 kW/cm^2 for the post-annealed ZnO film with the Al_2O_3 surface passivation layer. This threshold intensity for stimulated emission of the ZnO film grown by ALD is much smaller than that of GaN thin films (800 kW/cm^2) [7,8], suggesting that the ZnO film grown by the ALD technique has a high optical quality.

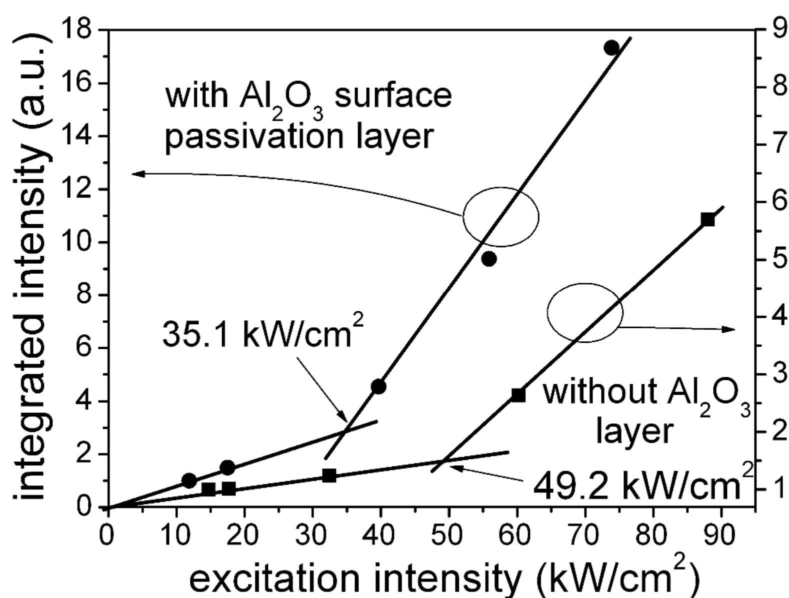

Figure 3.4 The integrated PL intensity as function of the excitation intensity of the post-annealed ZnO films *with* and *without* the Al_2O_3 surface passivation layer.

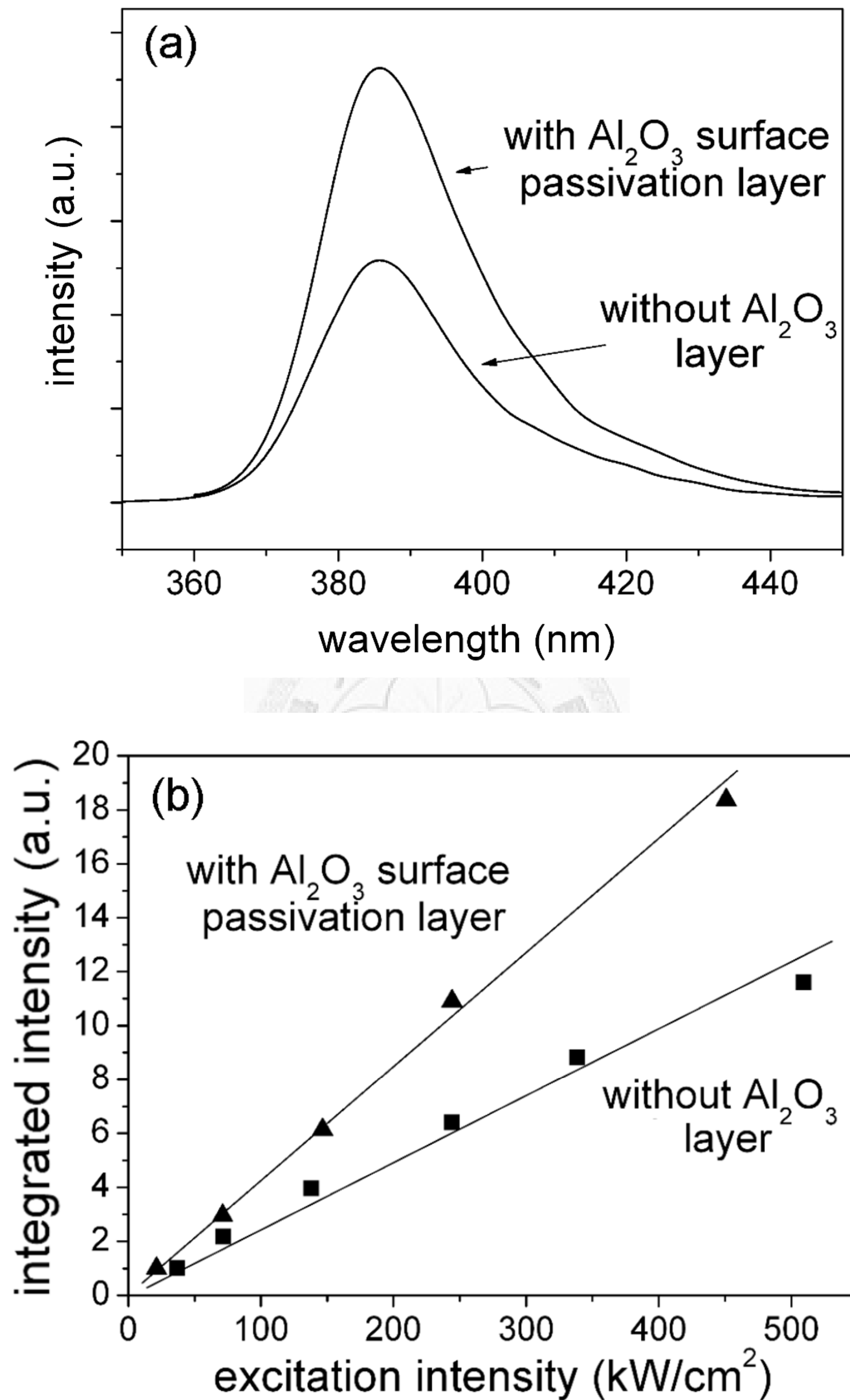

Figure 3.5 PL measurements of the as-deposited ZnO films *with* and *without* the Al_2O_3 passivation layer: (a) PL spectra at an excitation intensity of 244 kW/cm^2. (b) The integrated PL intensity as function of the excitation intensity.

The integrated PL intensity versus the excitation intensity for the post-annealed ZnO film without the Al_2O_3 surface passivation layer is also plotted in Fig. 3.4. It is shown that the ALD Al_2O_3 layer effectively passivates the ZnO surface, reducing surface nonradiative recombination and thus lowering the threshold of stimulated emission from 49.2 kW/cm^2 to 35.1 kW/cm^2. The PL spectra and the integrated PL intensity vs. excitation intensity relationship of the as-deposited ZnO films with and without the Al_2O_3 surface passivation layer are shown in Fig 3.5 It is clearly shown that the nonradiative recombination at the ZnO surface is suppressed by the Al_2O_3 layer and thus the PL intensity is larger for the sample with the Al_2O_3 layer. As compared with Fig. 3.4, no super-linear increase in the PL intensity with the excitation intensity was observed in Fig. 3.5(b) for the as-deposited samples, indicating that the high-temperature post-deposition annealing greatly improves the crystal quality to achieve the low-threshold stimulated emission in ZnO films.

3.2.6 Gain spectrum

Figure 3.6 shows the optical gain spectra of the ZnO film as measured by the variable stripe length (VSL) technique [9]. The sample was optically excited by a fourth harmonic Q-switched Nd:YAG laser with excitation intensities of 59.2 kW/cm^2 and 102.6 kW/cm^2. A cylindrical lens focused the laser beam to form a 100μm-wide stripe on the ZnO film surface. A variable slit changed the length of the stripe from 0.025 cm to 0.2 cm. The ASE spectra were collected from the edge of the stripe. The ASE spectra were analyzed using the standard one-dimensional optical amplifier model [10],

$$I_{\mathrm{ASE}} = \frac{I_{sp}}{g}(e^{gL} - 1) \tag{3.5}$$

where I_{ASE} is the ASE intensity, I_{sp} is the spontaneous emission intensity, g is the

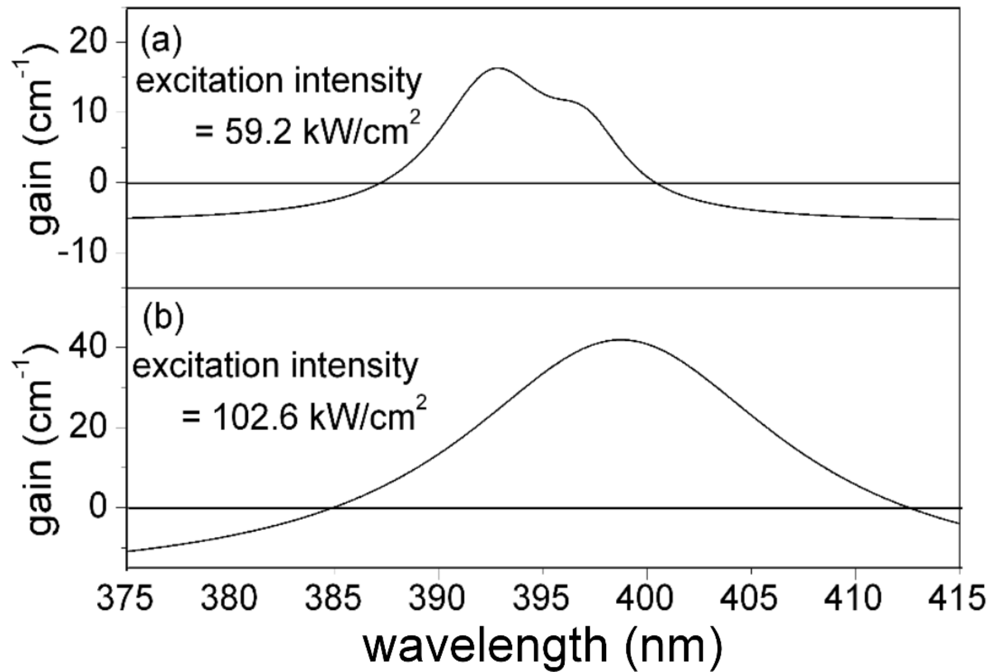

Figure 3.6 The optical gain spectra of the post-annealed ZnO film *with* the Al_2O_3 surface passivation layer at excitation intensities of (a) 59.2 kW/cm^2 and (b) 102.6 kW/cm^2.

optical gain coefficient, and L is the length of the excitation stripe. Compared with the stimulated emission spectra in Fig. 3.3, the positive optical gain around 392 nm and 397 nm in Fig. 3.6(a) may correspond to the exciton-exciton scattering and EHP, respectively. At higher excitation intensity as shown in Fig. 3.6(b), the maximum optical gain shifts to 399 nm, which is attributed to the bandgap renormalization associated with EHP. The optical gain spectra confirm that the stimulated emission in ZnO films causes the spectral peaks in the PL spectra as shown in Fig. 3.3.

3.2.7 Al doping effect

Table 3.1 summarizes the electrical properties of the as-deposited and post-annealed ZnO films, including carrier type, carrier concentration, mobility, and

resistivity. A remarkable feature is that the carrier concentration increases by about one order of magnitude after the high-temperature post-annealing. Secondary ion mass spectrometry (SIMS) shows that Al atoms appear in the post-annealed ZnO film. The Al concentration is highest at the ZnO/sapphire interface, and gradually decreases as the probe depth approaches the sample surface. This indicates that the high-temperature post-annealing caused the Al atoms to diffuse from the sapphire into the ZnO film. The Al doping in the ZnO film results in the increase in electron concentration and the decrease in the oxygen vacancies, which in turn reduce the nonradiative recombination [11,12]:

$$Al_2O_3 + V_o^{\bullet\bullet} \rightarrow 2Al_{Zn}^{\bullet} + 3O_o^{\times} \tag{3.6}$$

Thus the Al doping effect also leads to the lowering of the stimulated emission threshold in the ZnO films.

Table 3.1 Hall effect measurements of the as-deposited and post-annealed ZnO films.

Sample	Carrier type	Carrier concentration (cm^{-3})	Mobility (cm^2/Vs)	Resistivity (Ωcm)
As-deposited	n-type	1.32×10^{17}	48.5	0.97
Post-annealed	n-type	2.76×10^{18}	16.1	0.14

3.3 Reduction in stimulated emission threshold of ZnO:Al

3.3.1 Sample preparation

The Al-doped ZnO thin films were deposited by ALD on the (0002)-oriented sapphire substrate held at 180°C. The ALD process consisted of two kinds of cycles, one of which contained the following sequence: DEZn, 0.01 sec.→ N_2 purge, 5 sec.→ H_2O, 0.1 sec.→ N_2 purge, 5 sec. for the growth of ZnO (cycle A), and the other contained TMA, 0.03 sec.→ N_2 purge, 5 sec.→ H_2O, 0.1 sec.→ N_2 purge, 5 sec. for the doping of Al (cycle B). The ALD cycle B was uniformly or concentratedly distributed in total 1000 ALD cycles. The ratios of the number of A and B cycles were 49:1, 24:1 and 16:1 to prepare the ZnO:Al films with 2%, 4% and 6% Al doping percentages, respectively. After deposition, the films were annealed at 1000°C for 2 hours in nitrogen atmosphere using a furnace to improve the crystalline quality. The post-annealed ZnO:Al films were analyzed by X-ray diffraction (XRD), photoluminescence (PL) and Hall effect with the van der Pauw configuration.

3.3.2 Crystal quality

Figure 3.7 shows the XRD patterns of the post-annealed ZnO:Al films. Only the appearance of ZnO (0002) peak reveals that the samples have high crystallinity with (0002) preferred orientation, even with the Al doping percentage up to 4%. Figure 4.1 also shows the full-width at half-maximum (FWHM) of the ZnO (0002) Kα1 peak versus the Al doping percentage, indicating that the FWHM increased from 0.08^o to 0.12^o with increasing Al concentration. The broadening of the ZnO (0002) peak might result from the distortion of ZnO crystal structure due to the doping of Al. Since the solid solubility limit of Al in ZnO is only 2 mole% [13], a large amount of Al atoms might segregate from the surrounding ZnO, leading to the dramatic broadening of ZnO (0002) peak in the ZnO:Al films with 4% Al doping percentages.

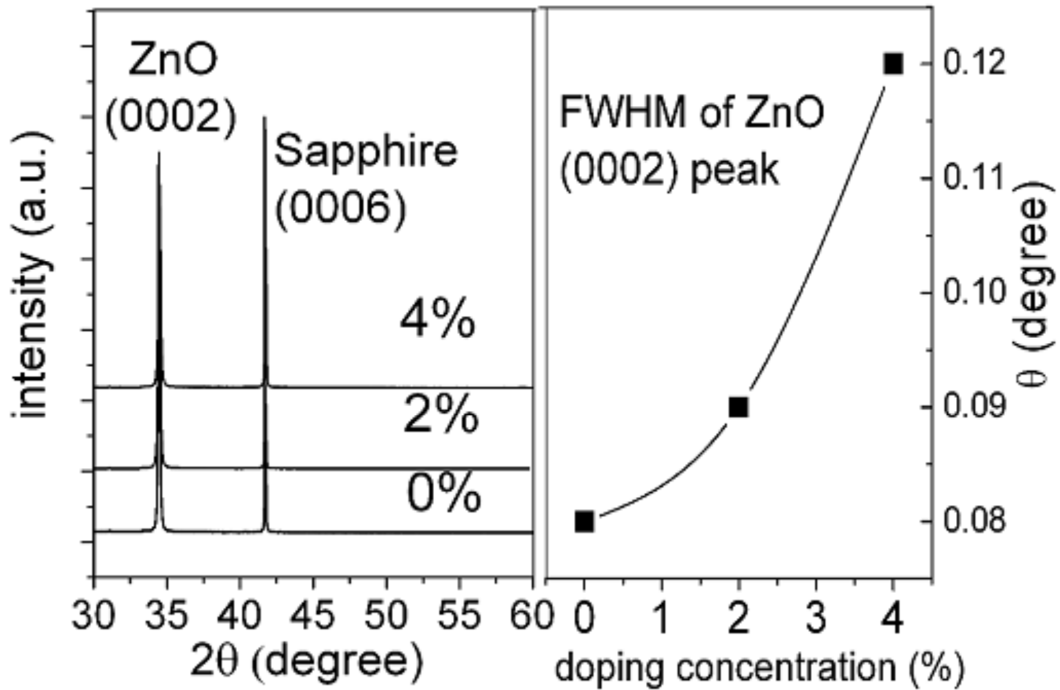

Figure 3.7 XRD patterns and FWHM widths of the (0002) peaks of the ZnO:Al films with Al doping percentage of 0%, 2%, and 4%.

3.3.3 Reduction of the stimulated emission

The PL spectra of the ZnO:Al films were measured at room temperature using a fourth harmonic Q-switched Nd:YAG laser (266 nm, 10 ns, 15 Hz) as the excitation source. The PL measurement was conducted in the standard backscattering configuration where the light emission from the top surface of the sample was collected. The PL spectra of the ZnO:Al films with 0% and 4% Al doping percentage are shown in Fig. 3.8 and Fig. 3.9, respectively. The spontaneous emission associated with the free excitons or donor bond excitons at 383 nm (3.23 eV) was observed at low excitation intensity [2,14]. An increase in the excitation intensity causes the exciton concentration to reach the Mott density, where the excitons overlap with each other, lose their individual character, and eventually become electron-hole plasma

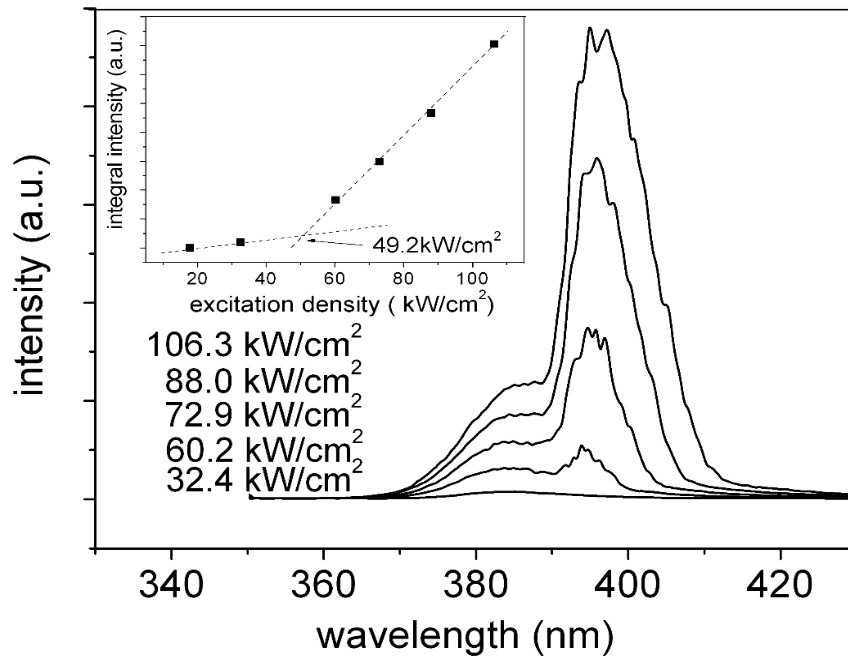

Figure 3.8 PL spectra of the ZnO:Al film with 0% Al doping percentage. The inset is the integrated PL intensity as a function of the excitation intensity.

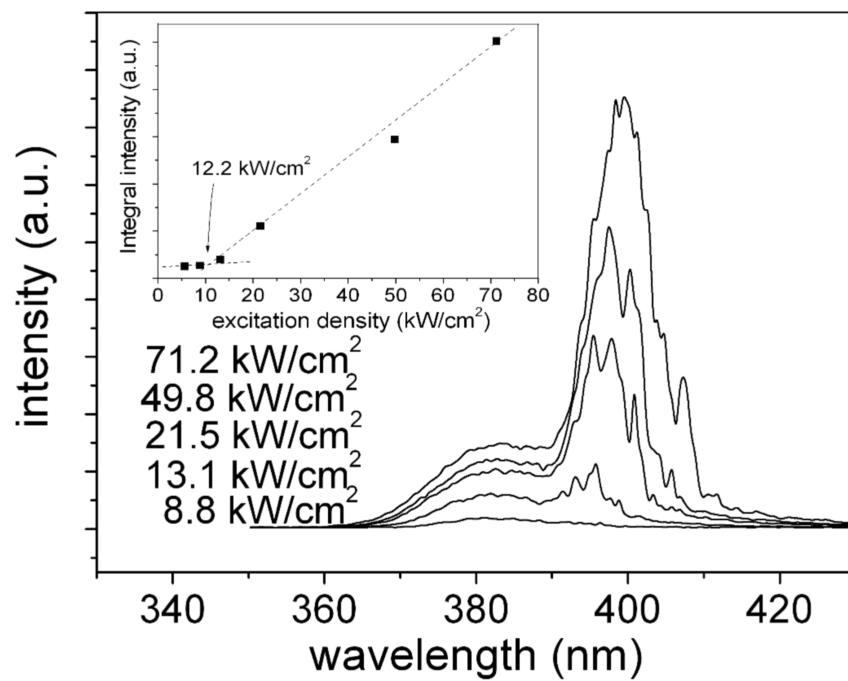

Figure 3.9 PL spectra of the ZnO:Al film with 4% Al doping percentage. The inset is the integrated PL intensity as a function of the excitation intensity.

(EHP). Thus a spectral peak attributed to EHP appears around 394 nm (3.14 eV) at high excitation intensities [3]. With further increase in the excitation intensity, the EHP peak gradually dominates the emission spectrum and shifted toward lower energy due to band gap renormalization [3,15-18]. The inset of the Fig. 3.8 and Fig. 3.9 shows the plot of the integrated PL intensity versus the excitation intensity. The integrated PL intensity is seen to increase super-linearly with the excitation intensity. The appearance of the spectral peaks as well as the super-linear increase of the emission intensity with the excitation intensity indicate that the stimulated emission in the ZnO:Al film take place. The thresholds for stimulated emission of the samples with 0% and 4% doping percentages are 49.2 kW/cm^2 and 12.2kW/cm^2, respectively.

Since the diameter of the incident laser beam in this study was about 1 mm, which is much larger than the film thickness, it is likely that the stimulated emission was caused by the closed loop paths in the direction parallel to the film surface via multiple scattering between optical scattering centers and crystalline grains. The scattering of the stimulated emission propagating in the in-plane direction might lead to the observed stimulated emission in the direction perpendicular to the film surface [13].

Figure 3.10 shows the threshold for stimulate emission of ZnO:Al films as a function of the Al doping percentage. With increase in the Al doping percentage, the threshold of stimulated emission drops from 49.2kW/cm^2 to 12.2kW/cm^2. Table 3.2 summarizes the electrical properties of the ZnO:Al films characterized by the Hall effect measurement using the van der Pauw configuration. The electron concentrations of all samples are of the same order of magnitude (10^{18} cm^{-3}) and do not increase with the Al doping percentage, suggesting that the Al atoms do not contribute to the electron donors in the heavily doped ZnO:Al films. As mentioned above, a large amount of Al atoms may segregate in the heavily doped ZnO:Al films

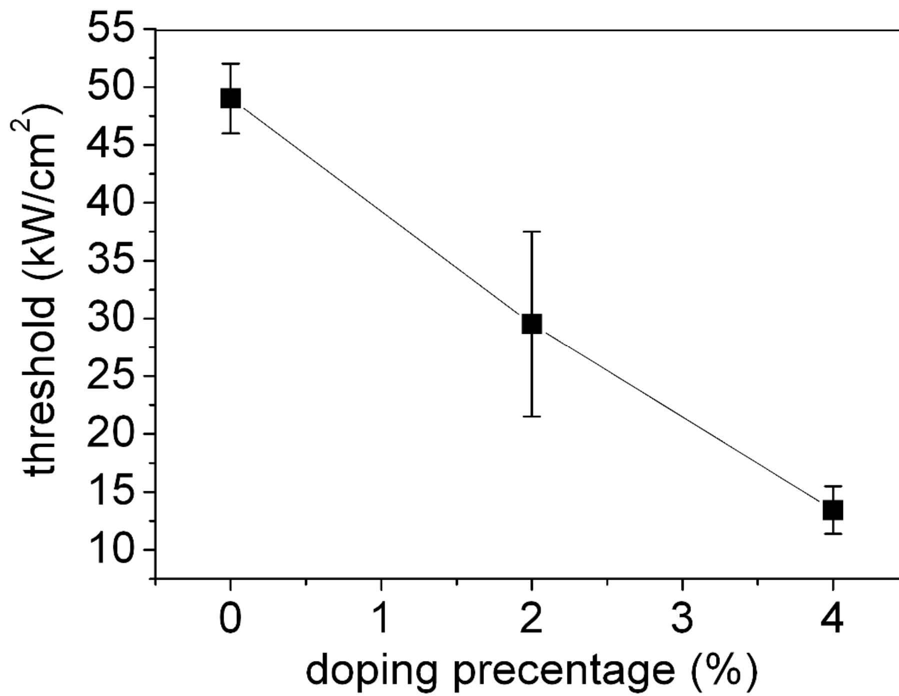

Figure 3.10 Threshold for stimulate emission of ZnO:Al films versus the Al dopingpercentage.

Table 3.2 Hall effect measurement of the ZnO:Al films with Al doping percentage of 0%, 2%, and 4%.

Sample	Type	Carrier concentration	Mobility (cm^2/Vs)	Resistivity (Ωcm)
0%	n	2.76×10^{18}	16.12	0.14
2%	n	2.369×10^{18}	48.49	0.054
4%	n	1.16×10^{18}	13.5	0.398

due to the solid solubility limit of Al in ZnO [13]. The segregation of Al might result in strong optical scattering in the ZnO:Al films. The increase in optical scattering due to the increasing Al doping percentage may facilitate the formation of closed-loop paths for light through multiple optical scattering, leading to the decrease in the threshold of stimulated emission [19,20]. It is also seen in Fig. 3.9 that there are many narrow spectral peaks appearing upon the emission spectra of the ZnO:Al film with 4% Al doping percentage. However, the 0% doping sample exhibits relatively smooth emission spectra, as shown in Fig. 3.8. The appearance of the narrow spectral peaks upon the spectra of 4% doping sample may be attributed to the constructive closed-loop paths due to optical scattering provided by the Al segregation in the heavily doped ZnO:Al films [21,22].

3.4 Random lasing in heavily doped 6% ZnO:Al thin film

3.4.1 Sample configuration

As shown in Fig. 3.11, two kinds of doping configuration were performed in growing 6% aluminum doped ZnO thin films. In configure **A**, aluminum is uniformly distributed into ZnO thin film, and concentrated doping in configuration **B**.

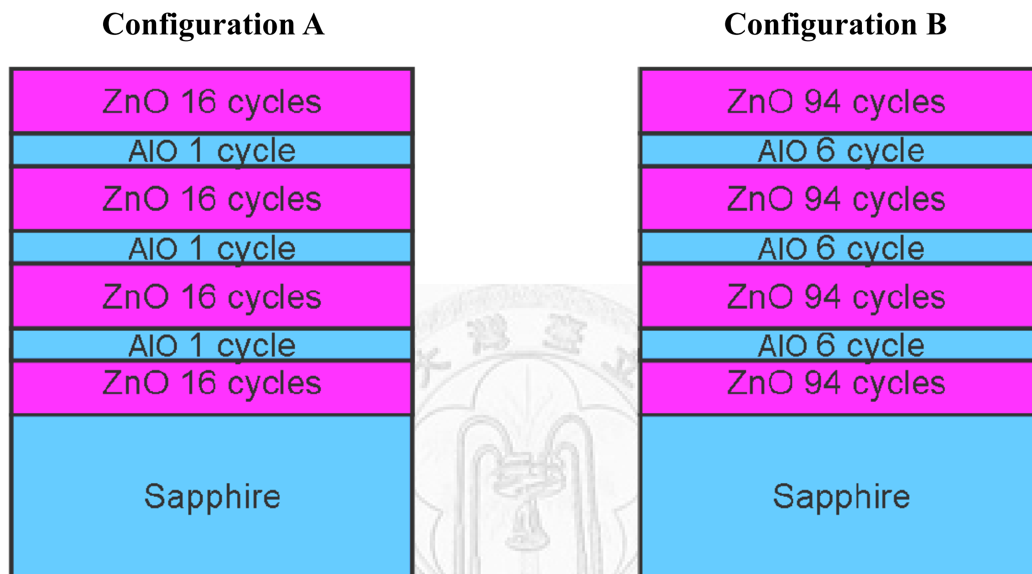

Figure 3.11 Two different configuration of Al doped ZnO:Al thin films. Configure A is the uniformly doped ZnO:Al film, and configure B is the concentrated doped ZnO:Al.

3.4.2 Crystal quality

Figure 3.12 shows the ZnO x-ray diffraction pattern, the appearance of (0002) peak of two samples reveals that the ZnO films were crystallized with c-axis orientation. The full-width at half-maximum (FWHM) of the spread doping peak and concentrated doping peak are 0.177^{o} and 0.169^{o}. Using the Scherrer's formula, Eq. (3.1), which is used to estimate the size of very small crystal, the grain size of the two samples was estimated to be 47nm and 49nm. These two samples have similar grain size.

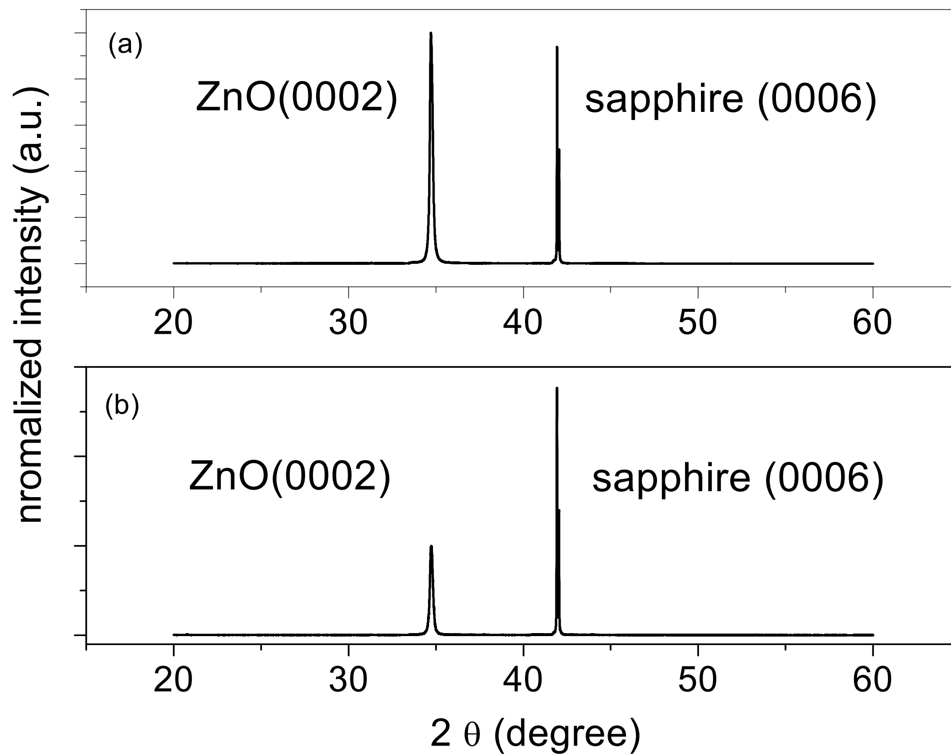

Figure 3.12 The XRD patterns measured in θ-2θ configuration, normalized by the intensity of ZnO (0002) peak. (a) the 6% Al doped ZnO grown by spread doping configuration; (b) the 6% Al doped ZnO grown by concentrated doping configuration.

3.4.3 Stimulated emission with random lasing

Figure 3.13 shows the photoluminescence (PL) of spread doped sample which was measured at room temperature using a fourth harmonic Q-switched Nd:YAG laser (266 nm, 10 ns, 15 Hz) as the excitation source. The PL spectrum was measured in backscatter configuration, and various excitation powers were performing to study its optical property. The spectrum of spread doping sample shows many spectral peaks (FWHM is 4meV, 0.5nm) between 3.2eV to 3.1eV at low excitation power, and as the excitation power increase, the spectral of the same range turn into a broad peak with some small peaks. The integral intensity of the spectrum is shown in the inset of Fig. 3.13, we can find out that there are two thresholds, one at 6.9kW/cm^2 and the

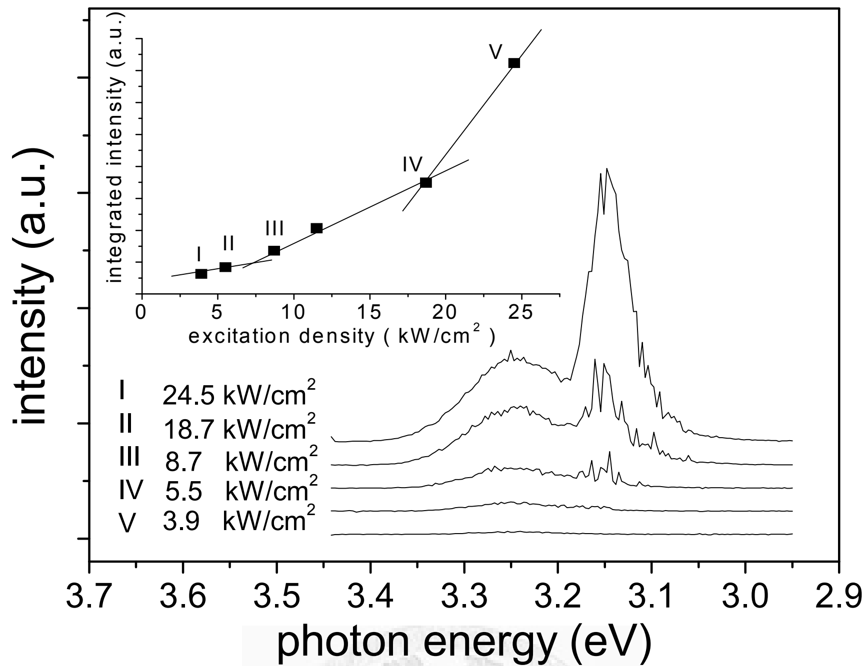

Figure 3.13 The photoluminescence spectrums of the spread doping sample of various excitation powers. The inset is the integral intensity of different excitation powers.

other at 18.4kW/cm^2. Combine these two information, we conceive that there are two lasing threshold, the first one begin at 6.9 kW/cm^2 excitation intensity and shown many spectral peaks, and the other started from 18.4kW/cm^2 and turn into a broad peak.

In Fig. 3.14 and the inset plot, the photoluminescence spectrum of the concentrated doping sample, also shows two thresholds when the pumping power increase, the first lasing threshold at 39.5 kW/cm^2 and the second one at 119.6 kW/cm^2. The spectrums initially appear many spectral peaks between 3.2eV to 3.1eV; as the excitation power raised the peaks were growing up and extend to lower photonic energy. Compare to Fig. 3.13, the major difference between them is the intensity of spontaneous emission (3.26eV) in Fig.3.13 is increasing with pumping

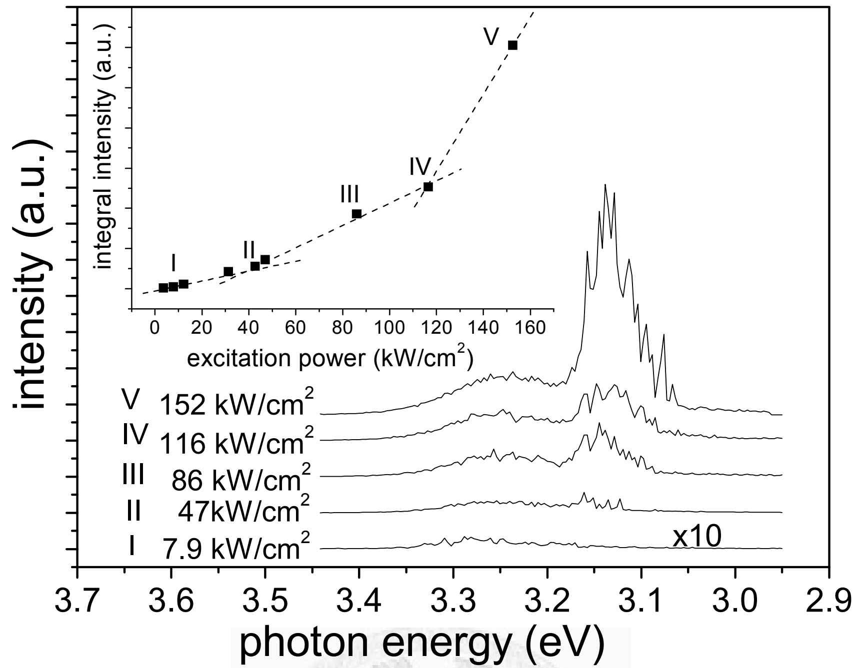

Figure 3.14 The photoluminescence spectrums of the concentrated doping sample of various excitation powers. The inset is the integral intensity of different excitation powers.

energy increase, but the spontaneous emission intensity of Fig. 3.14 is nearly the same as the excitation power raise. This is due to the more completed cavities formed in the concentrated doping sample, and the spontaneous emission light are absorbed and depressed between scattering trips [23,24]. In addition, at high excitation power, the spectral peaks are more obvious in concentrated doping sample than the spread doping sample. As well, the phenomenon is resulted from the more completed scattering cavities in the film. The scattering cavities in ZnO films are originated from the segregation of AlO_x, which is introduced by Al doping step in ALD growing procedures and the post annealing process. The reason of the formation of the AlO_x segregation is that the Gibbs free energy of formation (ΔG_f) of Al_2O_3 is −1582.3 kJ/mol and is −320.5 kJ/mol of ZnO [25], therefore lots of AlO_x segregation must be

formed in the films after annealing process. As the segregation formed, the light in the film was scattered between the segregations and construct a close loop as a cavity.

Seeing into the insets of Fig. 3.13 and Fig. 3.14, they appear different threshold intensity, but roughly the same ratio of the first and second threshold of the two figures, one is 2.67 and the other is 3.02. This means two samples were experienced the same mechanism in lasing process except the different level of scatter. And the different threshold intensity is originated from the different electron concentration of them. From the Hall Effect measurement, the concentration of two samples were obtained, 9.9×10^{18} cm^{-3} for spread sample and 2×10^{18} cm^{-3} for concentrated sample, therefore, different excitation power had to be imposed to achieve the Mott density [9,26].

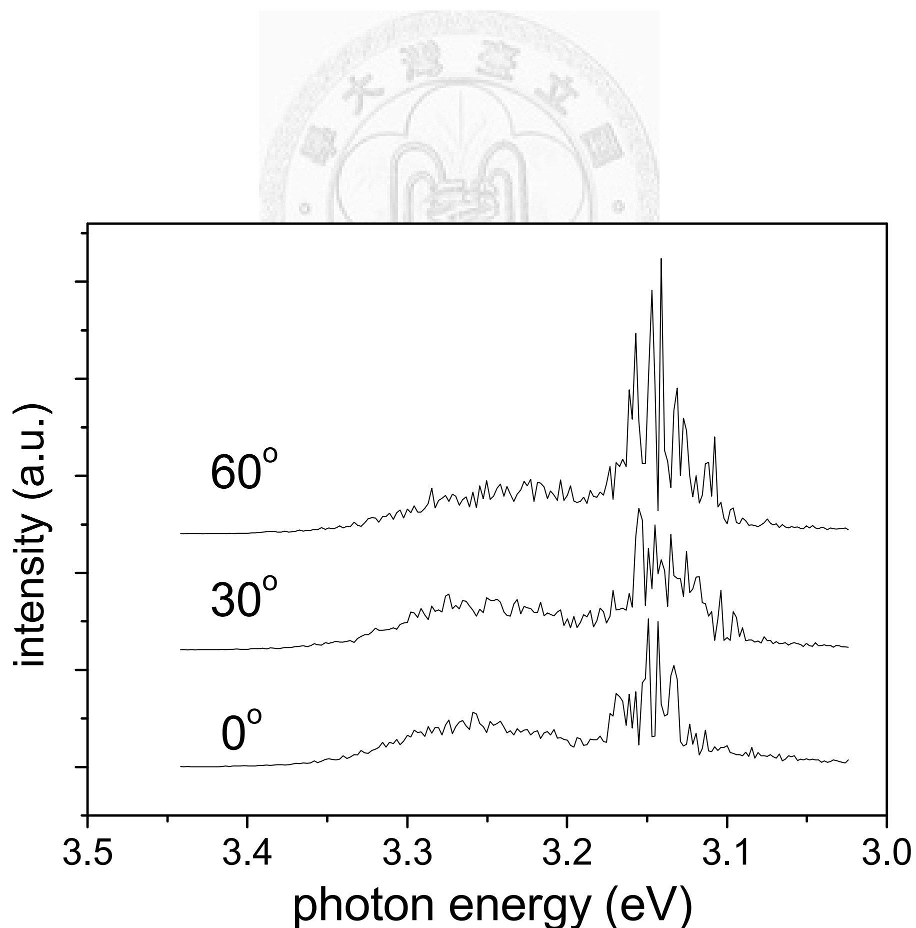

Figure 3.15 The photoluminescence spectrums of concentrated doping sample in 0°, 30° and 60° directions.

3.4.4 Examining of random lasing

Facing to the physical meanings of the two lasing threshold, we treat the second threshold first. According to the broad shape and the photonic energy of 3.14eV of the spectral peak in the spectrum behind the second threshold, it is easy to identify the second threshold comes from the electron-hole plasma (EHP) mechanism of stimulated emission [9]. Dealing with the first threshold, we performed the experiment that excited the concentrated doping ZnO film with about 50 kW/cm^2 of 266nm Nd-YAG laser in backscattering configuration and measure the photoluminescence from 0°, 30°, 60° respect to the incident line. The result is shown in Fig. 3.15 that the lasing spectral peaks were observed in all direction. From the random lasing theory, the emitting case unlike conventional laser, the laser can be detected in all directions [22]. With above-mentioned, the lasing phenomenon between first and second threshold is identified as random lasing.

3.5 Summary

ZnO films were grown on sapphire substrates by ALD, followed by high-temperature post-annealing and surface passivation by overcoating an ALD Al_2O_3 layer. The post-annealing improves the crystallinity of the ZnO films and the Al_2O_3 surface passivation layer effectively suppresses surface nonradiative recombination. PL measurements in the backscattering configuration show that the room-temperature stimulated emission associated with the exciton-exciton scattering and EHP has a low threshold of 35.1 kW/cm^2. The high-quality ZnO film and Al_2O_3 surface passivation layer grown by the ALD technique, as well as the Al doping effect caused by the thermal diffusion of Al from the sapphire into the ZnO may contribute to this low-threshold stimulated emission.

Reduction in stimulated emission threshold in the heavily Al-doped ZnO films

with Al doping percentage up to 4% was present. Even with the Al doping percentage up to 4%, the ZnO:Al film is highly crystalline with c-axis orientation. The increase in the Al concentration causes the decrease in the threshold of stimulated emission, from 49.2kW/cm^2 of 0% to 12.2kW/cm^2 of 4% Al doping percentage. The segregation of excess Al in the heavily doped ZnO:Al films might contribute to the optical scattering centers, resulting in close-loop paths and coherent feedback, and be responsible for the reduction in the threshold of stimulated emission with the increasing Al doping percentage.

The 6% ZnO:Al films with uniformly distributed and concentrated configurations are fabricated to investigate the effect of optical scattering centers in ZnO:Al thin film on threshold reduction. Because of the AlO_x segregations present in the ZnO:Al film scattered the light to from constructive close loops as cavities, there is random lasing phenomenon appearing when the excitation intensity reached the first threshold. As the pumping power gradually increase, the second threshold turned on with the occurrence of electron-hole plasma mechanism. According to the integral intensity plots of the two samples, the ratio of the first and second thresholds of each is about 3, this means the two samples were experienced the same mechanism in lasing process except the different level of scatter. From this study we can get a high crystalline, low random lasing threshold, and good emitting property ZnO film. These results indicate that the ALD technique is useful in preparing high-quality ZnO films for next-generation UV LEDs and lasers.

Reference

[1] Y. G. Wang, N. Ohashi, Y. Wada, I. Sakaguchi, T. Ohgaki, and H. Haneda, J. Appl. Phys. **100**, 023524 (2006).

[2] X. Q. Zhang, Ikuo Suemune, H. Kumano, J. Wang and S. H. Huang, *J. Appl. Phys.*, vol. 96, pp. 3733-3736, 2004.

[3] P. Zu, Z.K. Tang, G.K.L. Wong, M. Kawasaki, A. Ohtomo, H. Koinuma and Y. Segawa, *Solid Slate Commun.*, vol. 103, pp. 459-463, 1997.

[4] C. Klingshirn, *Phys. Status Solidi B*, vol. 71, pp. 547, 1975.

[5] C. Klingshirn, R. Hauschild, J. Fallert, and H. Kalt, *Phys. Rev. B*, vol. 75, pp. 115203-115212, 2007.

[6] M. H. Huang, S. Mao, H. Feick, H. Yan, Y. Wu, H. Kind, E. Weber, R. Russo, and P. Yang, *Science*, vol. 292, pp. 1897-1899, 2001

[7] X. H. Zhang, T. J. Schmidt, W. Shan, J. J. Song, and B. Goldenberg, *Appl. Phys. Lett.*, vol. 66, pp. 1-3, 1995.

[8] D. Wiesmann, I. Brener, L. Pfeiffer, M. A. Khan and C. J. Sun, *Appl. Phys. Lett.*, vol. 69, pp. 3384-3386, 1996.

[9] Y. Chen, N. T. Tuan, Y. Segawa, H.-J. Ko, S.-K. Hong, and T. Yao, *Appl. Phys. Lett.*, vol. 78, pp. 1469-1471, 2001.

[10] K. L. Shaklee, R. E. Nahory, and R. F. Leheny, *J. Lumin.*, vol. 7, pp. 284, 1973.

[11] Y. Wang, N. Ohashi, Y. Wada, I. Sakaguchi, T. Ohgaki, and H. Haneda, *J. Appl. Phys.*, vol. 100, pp. 023524-023530, 2006.

[12] H. Ryoken, I. Sakaguchi, N. Ohashi, T. Sekiguchi, S. Hishita, H. Haneda, *J. Mater. Res.*, vol. 20, pp. 2866, 2005.

[13] M. H. Yoon, S. H. Lee, H. L. Park, H. K. Kim and M. S. Jang, J. Mat. Sci. Lett. **21**, 1073 (2002).

[14] B. K. Meyer, H. Alves, D. M. Hofmann, W. Kriegseis, D. Forster, F. Bertram, J. Christen, A. Hoffmann, M. Straßburg, M. Dworzak, U. Haboeck, and A. V. Rodina,, phys. stat. sol. (b) **241**, 231 (2004)

[15] X. Q. Zhang, Z. K. Tang, M. Kawasaki, A. Ohtomo, and H. Koinuma, J. Cryst. Growth **259**, 286 (2003)

[16] Y. Segawa, A. Ohtomo, M. Kawasaki, H. Koinuma, Z. K. Tang, P. Yu, and G. K. L. Wong, Phys. Status Solidi B **202**, 669 (1997)

[17] Z. K. Tang, G. K. L. Wong, P. Yu, M. Kawasaki, A. Ohtomo, H. Koinuma, and Y. Segawa, Appl. Phys. Lett. **72**, 3270 (1998)

[18] D. M. Bagnall, Y. F. Chen, Z. Zhu, T. Yao, M. Y. Shen, and T. Goto, Appl. Phys. Lett. **73**, 1038 (1998)

[19] F. A. Pinheiro, L. C. Sampaio, Phys. Rev. A, **73**, 013826 (2006)

[20] H. Cao, J. Y. Xu, S.-H. Chang, and S. T. Ho., Phys. Rev. E, **62**, 1985 (2000).

[21] H. Cao, Y. G. Zhao, H. C. Ong, S. T. Ho, J. Y. Wu, and T. P. H. Chang, Appl. Phys. Lett. 73, 3656 (1998).

[22] H. Cao, Y. G. Zhao, H. C. Ong, and R. P. H. Chang, Phys. Rev. B **59**, 15107 (1999).

[23] Gijs van Soest and Ad Lagendijk, physical review E, volume 65, 047601(2002).

[24] S. F. Yu, Clement Yuen, S. P. Lau, and H. W. Lee, Appl. Phys. Lett., Vol. 84, No. 17, 2004

[25] Kyoung-Kook Kim, Shigeru Niki, Jin-Yong Oh, June-O Song, Tae-Yeon Seong, Seong-Ju Park, Shizuo Fujita and Sang-Woo Kim, J. Appl. Phys. 97, 066103, 2005

[26] Nobuyuki Arai, Jun Takeda, Hang-Ju Ko and Takafumi Yao, Journal of Luminescence, Volumes 119-120, Pages 346-349.

Chapter 4

Ultraviolet Electroluminescence of *n*-ZnO/*p*-GaN Heterojunction Light-Emitting Diodes at Forward Bias

4.1 Introduction

Although ZnO technology has considerably been progressing, it is still difficult to prepare reproducible and stable *p*-type ZnO films with high carrier concentration and low resistivity [1],[2]. Since ZnO and GaN have the same crystal structure (wurtzite) with a small in-plane lattice mismatch (1.8%), *p*-type GaN would be substituted for the *p*-ZnO. Actually, several investigators have been reported on *n*-ZnO/*p*-GaN heterojunction light-emitting diodes (LEDs) [3],[4],[5]-[8]. However, since the electron injection from *n*-ZnO dominates over the hole injection from *p*-GaN due to the higher carrier concentration in *n*-ZnO, the electroluminescence (EL) originates mainly from the *p*-GaN side in the *n*-ZnO/*p*-GaN heterojunction LEDs [3],[5]-[7]. Only Rodgers et al. demonstrated room-temperature (RT) EL from the *n*-ZnO side in the *n*-ZnO/*p*-GaN heterojunction, which was ascribed to the high crystal quality of *n*-ZnO layer grown by PLD [4]. However, the injection pulsed current is quite large (from 500 to 875 mA) in reference 15 for the observation of UV EL from ZnO.

In the first part of this chapter, the ALD technique was applied to grow high-quality *n*-type ZnO epilayer on the *p*-type GaN to fabricate a heterojunction LED. RT EL at 391 nm has been observed from the n-ZnO side in the *n*-ZnO/*p*-GaN heterojunction LED at a low DC injection current. The competition between the ELs from the n-ZnO and p-GaN is elucidated, taking account of the results of photoluminescence (PL), electrical measurements, X-ray diffraction and electron

microscopy observations. In second part, aluminum was evaporated on the back of the c-Al_2O_3 substrate to serve as an external-feedback reflector. The external optical feedback and ASE significantly enhance the UV EL from the high-quality ZnO epilayer at room temperature.

4.2 UV electroluminescence of *n*-ZnO/*p*-GaN heterojunction LED

4.2.1 Sample preparation

Figure 4.1 shows the schematic structure of the *n*-ZnO/*p*-GaN heterojunction LED we fabricated. First, a thin GaN buffer layer 30 nm thick and a thick undoped-GaN layer 2.5 μm thick were successively deposited on the c-Al_2O_3 substrate by MOCVD. Next, a Mg doped GaN (*p*-GaN:Mg) layer 300 nm thick was also deposited by MOCVD. The Hall effect measurement with the van der Pauw configuration reveals that the effective hole concentration and mobility in this p-GaN:Mg layer are approximately 2.6×10^{17} cm^{-3} and 11.9 $cm^2V^{-1}s^{-1}$, respectively.

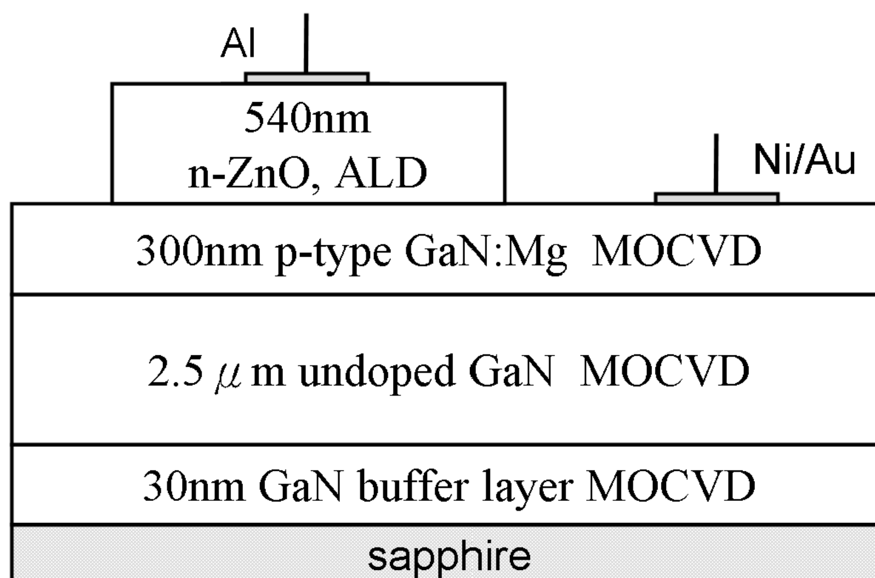

Figure 4.1 The device structure of the *n*-ZnO/*p*-GaN heterojunction LED.

Afterwards, a ZnO layer 540 nm thick was grown at 180°C on the p-GaN by ALD. The two precursors, diethylzinc (DEZn, $Zn(C_2H_5)_2$) and H_2O, were carried in by an N_2 flow. The ALD process consisted of 3000 identical cycles, each of which contained the following sequence: DEZn, 0.01 s $\rightarrow$ N_2 purge, 5 s $\rightarrow$ H_2O, 0.1 s $\rightarrow$ N_2 purge, 5 s and deposited ~ 0.18 nm of ZnO. After deposition, the ZnO layer was treated at 950°C for 5 min in N_2 atmosphere by rapid thermal annealing (RTA). The electron concentration and mobility in this annealed un-doped ZnO layer are 2×10^{18} cm^{-3} and 22.1 $cm^2V^{-1}s^{-1}$, showing intrinsic *n*-type characteristics. A circular ZnO mesa with 1 mm diameter was fabricated by masking the surface and chemically etching ZnO away using a diluted HCl solution. Ohmic contact to *p*-GaN was made by thermal evaporation of Ni/Au, followed by annealing at 500°C for 30 min in O_2 ambient. Finally an Al layer with radius of 100 μm was deposited on top of the *n*-ZnO to form the *n*-Ohmic contact.

4.2.2 Experimental setup and procedure

PL and EL spectra were measured using a SpectroPro 2300i monochromator with a 1200-groves/mm and 500-nm blaze grating. The PL measurements were performed at RT using a He-Cd laser (wavelength is 325 nm) as the excitation source.

The experimental setup for measuring the EL spectra is shown in Fig.4.2. A computer-controlled SpectroPro 2300i monochromator together with the conventional lock-in technique were used to measure the EL spectra. Light emission from *top surface of the ZnO epilayer* was collected using a lens. It was then focused on the input slit of the monochromator by another lens. A chopper was put in front of the monochromator to modulate the light. The lock-in amplifier was synchronized with the frequency of chopper to filter the noise and detect the signal.

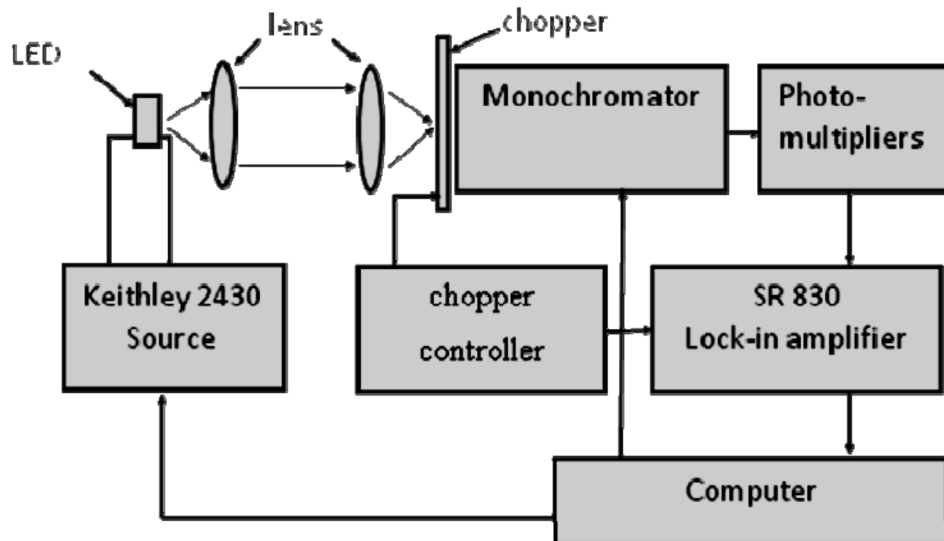

Figure 4.2. Experimental configuration for the measurement of EL spectra.

The crystal quality was evaluated by conventional X-ray diffraction (XRD) and X-ray rocking curve (XRC). The specimens for transmission electron microscopy (TEM) were prepared by mechanical polishing, followed by ion milling. TEM observations were performed in a Tecnai 30 scanning transmission electron microscope equipped with a lens of C_s = 1.2 mm, operated at 300 keV.

4.2.3 Crystal quality of the ZnO film on *p*-GaN

Figure 4.3 (a) shows the XRD patterns of the as-deposited and post-annealed ZnO films. The intensity of the ZnO (0002) XRD peak for the post-annealed film is four times lager than that for the as-deposited ZnO film. Figure 4.3 (b) displays the XRC curves of the as-deposited and post-annealed ZnO films. The full width of half maximum (FWHM) of the ZnO (0002) peak is 680 arcsec for as-deposited film and425 arcsec for the post-annealed film, indicating that the high-temperature post-deposition annealing by RTA improves the crystallinity. The corresponding *c*-axis lattice constants were calculated to be 0.524 nm and 0.518 nm from the XRC peaks in Fig. 4.3 (b), for the as-deposited and annealed ZnO films, respectively. It

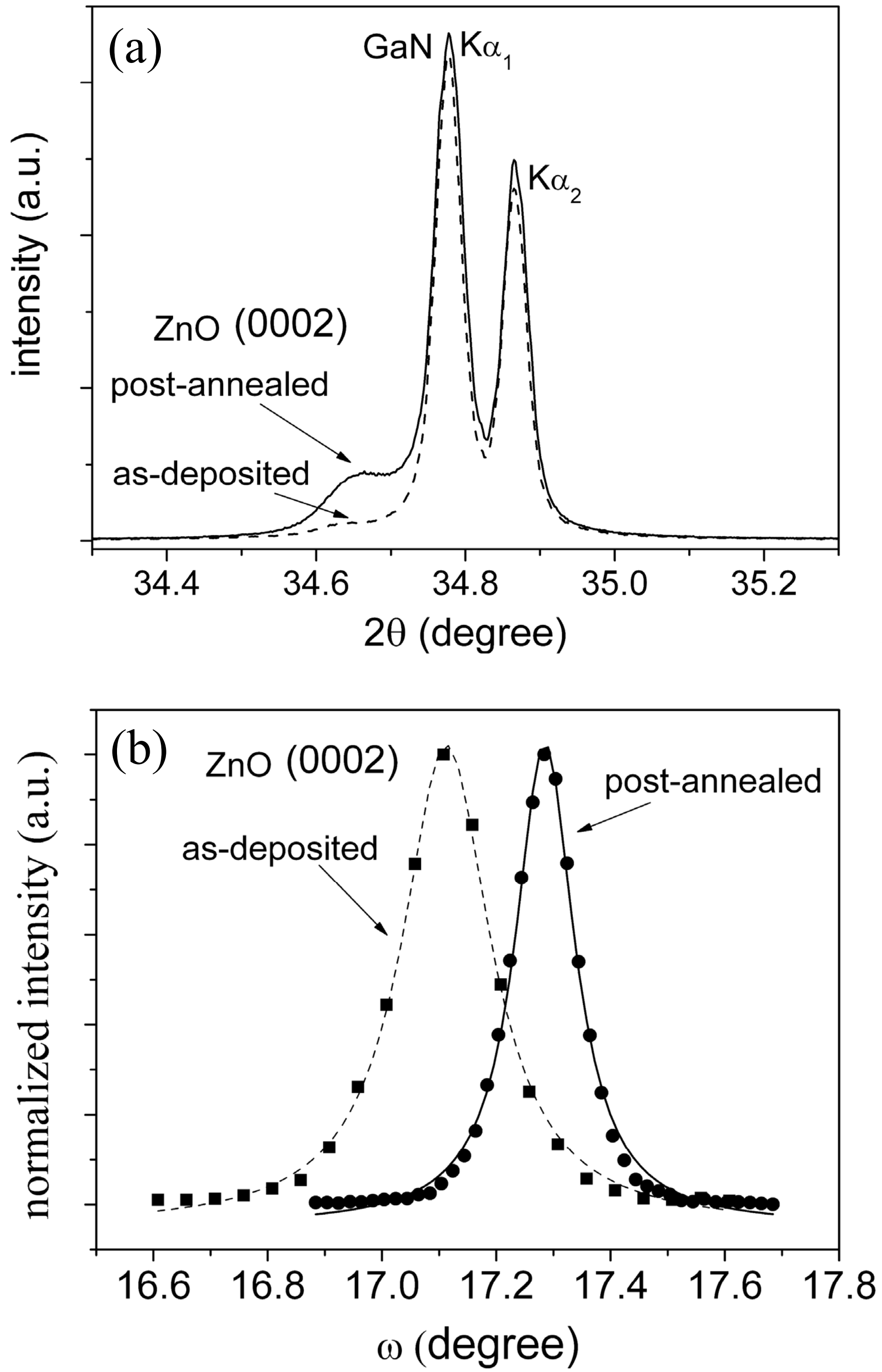

Figure 4.3 (a) X-ray diffraction patterns and (b) X-ray rocking curves of the as-deposited and post-annealed ZnO films grown by ALD on *p*-GaN.

seems to indicate a larger tensile strain and a smaller compress strain along the *c*-axis in the as-deposited and annealed ZnO films, as compared with the lattice constant in *c*-axis of pure bulk ZnO (0.5206 nm, according to ASTEM card CAS Number 1314-13-2). The lattice spacing of the as-deposited ZnO film might be almost the same in the basal plane as that of the GaN substrate. Because of the larger *a*-axis lattice constant of ZnO (0.3252 nm) than GaN (0.3189 nm), the lattice spacing *a* in the as-deposited ZnO film might be shrank. Therefore, for keeping the unit volume of the ZnO the lattice along the *c*-direction would be extended (to 0.524 nm) in the as-deposited ZnO film. After the RTA treatment, the interfacial layer was formed (will be shown in the following) and accordingly the tensile strain in ZnO was relaxed. We think the intrinsic lattice constant in *c*-axis of the annealed ZnO film upon the interfacial layer is 0.518 nm. It should be noted that the as-deposited ZnO on the GaN layer is still crystalline and preferably (0001)-oriented due to a small lattice mismatch between ZnO and GaN, which results in the perfect crystal by coalescence during the RTA treatment. Figure 4.4 shows a cross-sectional TEM image of the *n*-ZnO/*p*-GaN heterojunction LED on the *c*-Al_2O_3 substrate. The inset selected-area electron diffraction patterns reveal that the ZnO grew in completely parallel orientation, $[0001][11\bar{2}0]_{ZnO}//[0001][11\bar{2}0]_{GaN}$, with the GaN, which was deposited with a good epitaxial relation, $[0001][11\bar{2}0]_{GaN}//[0001][1\bar{1}00]_{Al_2O_3}$, on the *c*-$Al_2O_3$ substrate. The *n*-ZnO, *p*-GaN and underlying non-doped GaN layers are a little different in contrast and can been identified in the image, accordingly. The threading dislocations, which were generated on the interface between the GaN buffer layer and the *c*-Al_2O_3 substrate, run along the *c* axis of the GaN layers. Some of the dislocations still reach the vacuum, penetrating through the ZnO layer. The others however disappear at the interface between the *n*-ZnO and *p*-GaN or at the interface between the *p*-GaN and undoped GaN layers. Hence, the TEM image reveals that the ZnO layer is almost a

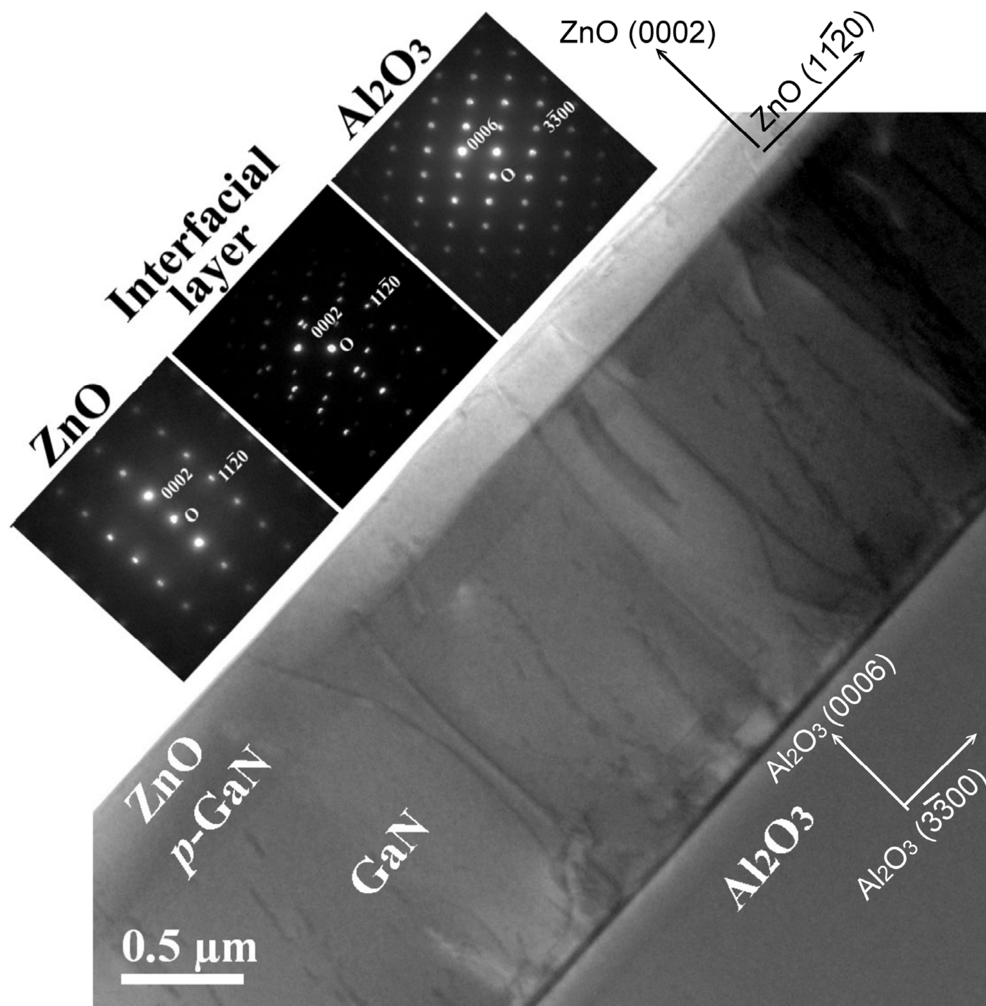

Figure 4.4 Cross-sectional bright field transmission electron microscopy (TEM) image of the *n*-ZnO/*p*-GaN heterojunction on the underlying GaN and Al_2O_3 substrate, and selected-area electron diffraction patterns from the Al_2O_3 layer, the interfacial layer and the ZnO layer. The spots in the interfacial layer comprise the spots from the ZnO (whose 0002 and $11\bar{2}0$ spots are marked) and additional spots from an unknown crystal formed with an orientation with their *c*-axis.

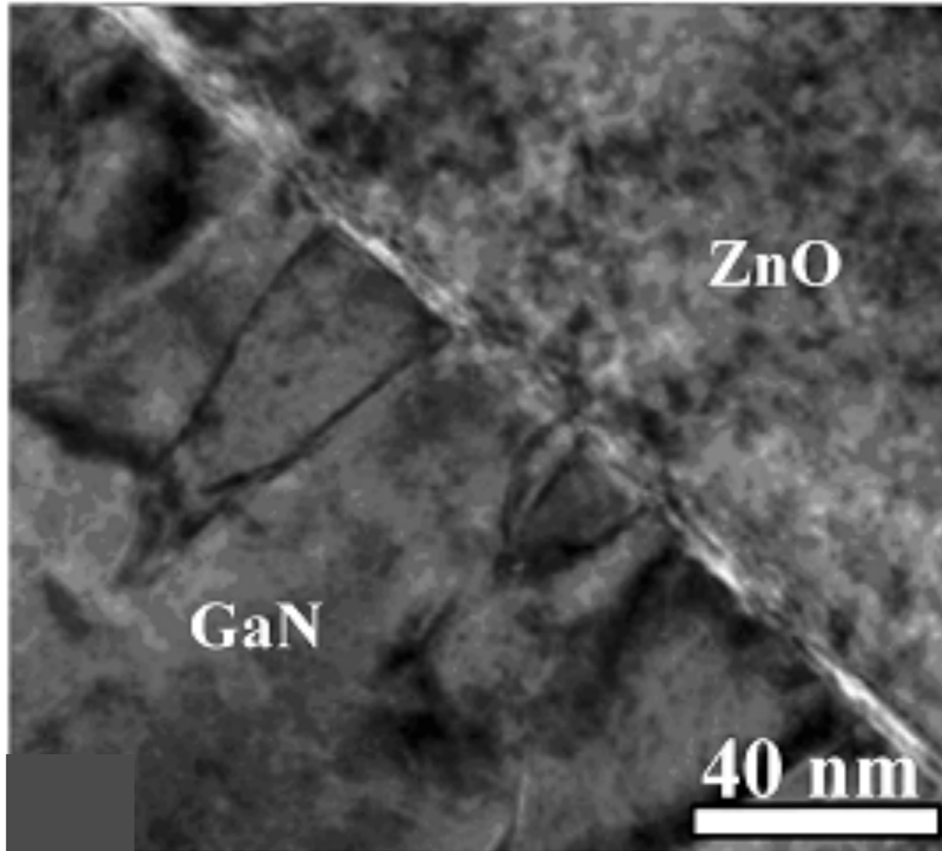

Figure 4.5 Cross-sectional TEM image of an area in the *n*-ZnO/*p*-GaN heterojunction.

perfect single crystal with very a few survival threading dislocations, which is attributable to the layer-by-layer growth of ALD and the recrystallization during the post heat treatment of RTA. Therefore, the crystal quality of the ZnO layer seems much superior to that of ZnO layers prepared by other methods such as electron cyclotron resonance-assisted MBE [11]. The formation of the high-quality crystalline ZnO is surely one of requirements for the UV EL from the ZnO.

The details of the interface between *p*-ZnO and *n*-GaN layers were observed to deliberate on the EL mechanism. Figure 4.5 indicates the dislocations annihilated on the interface. Furthermore, it indicates the presence of an interfacial layer along the (0001) interface between the *p*-ZnO and *n*-GaN layers.

4.2.4 Optical property of *n*-ZnO and *p*-GaN

In figure 4.6 the normalized PL spectra of the *n*-ZnO and *p*-GaN layers under the same excitation intensity are shown. The PL spectrum of *n*-ZnO exhibits a strong, near-band-edge (NBE) emission at 378 nm with negligible defect-related bands in the visible region. This NBE emission is associated with the radiative recombination of free excitons [9]. In contrast, the PL spectrum of *p*-GaN reveals a deep-level emission around 430 nm, which can be ascribed to the transitions from the conduction band or unidentified shallow donors to the Mg acceptor levels [10]. The NBE emission from *p*-GaN was not observed. The PL intensity of *n*-ZnO is significantly (21 times) greater than that of *p*-GaN layer, indicating a higher light emission efficiency in ZnO due to its larger excitonic binding energy.

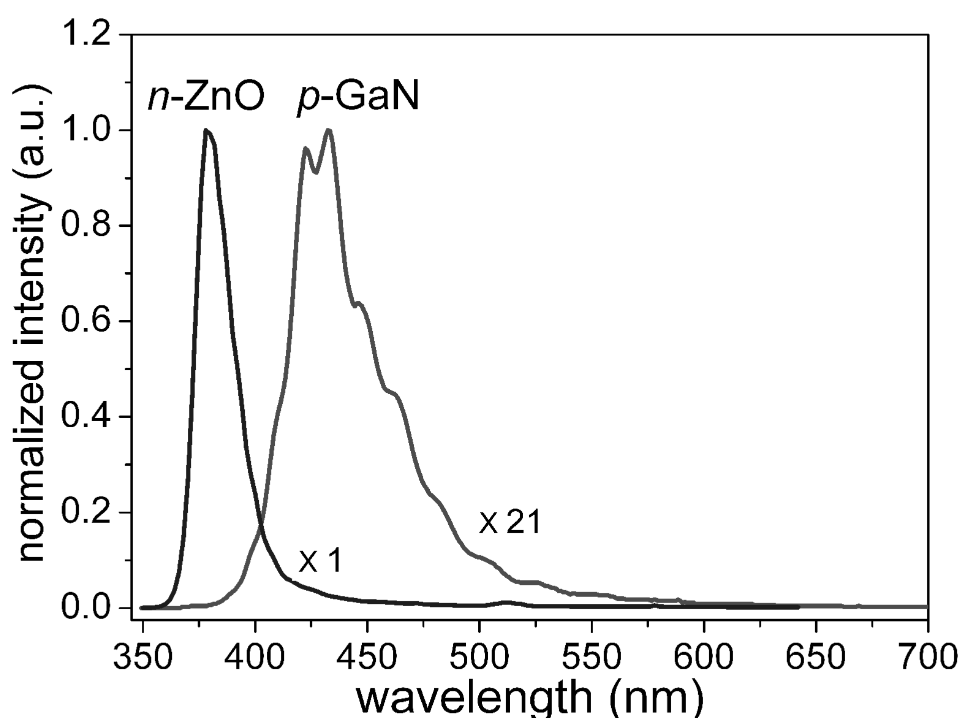

Figure 4.6 Room temperature (RT) photoluminescence spectra of the *p*-GaN layer and the *n*-ZnO layer grown on the *p*-GaN.

4.2.5 Electroluminescence

Figure 4.7 shows the current *vs*. voltage (*I-V*) characteristics of the *n*-ZnO/*p*-GaN heterojunction LED at RT. A rectifying diode-like behavior is clearly observed. Figure 4.8 shows the EL spectra of the *n*-ZnO/*p*-GaN heterojunction LED under DC forward bias at RT. The EL image of this LED is shown in the inset of figure 4.7. At a low injection current of 2.5 mA, the EL exhibits a spectral peak at 425 nm. Emission at 391 nm apparently increases with the injection current and becomes dominant when the current exceeds 12.5 mA. A comparison between EL and PL spectra reveals that the spectral peak around 425 nm is attributed to the light emission from the Mg acceptor levels in *p*-GaN, and the EL at 391 nm originates from the *n*-ZnO layer. Unlike the *n*-ZnO/*p*-GaN hetrojunction LEDs in references 12 and 29-31, where the EL originated only from either the *n*-ZnO or *p*-GaN side, the EL

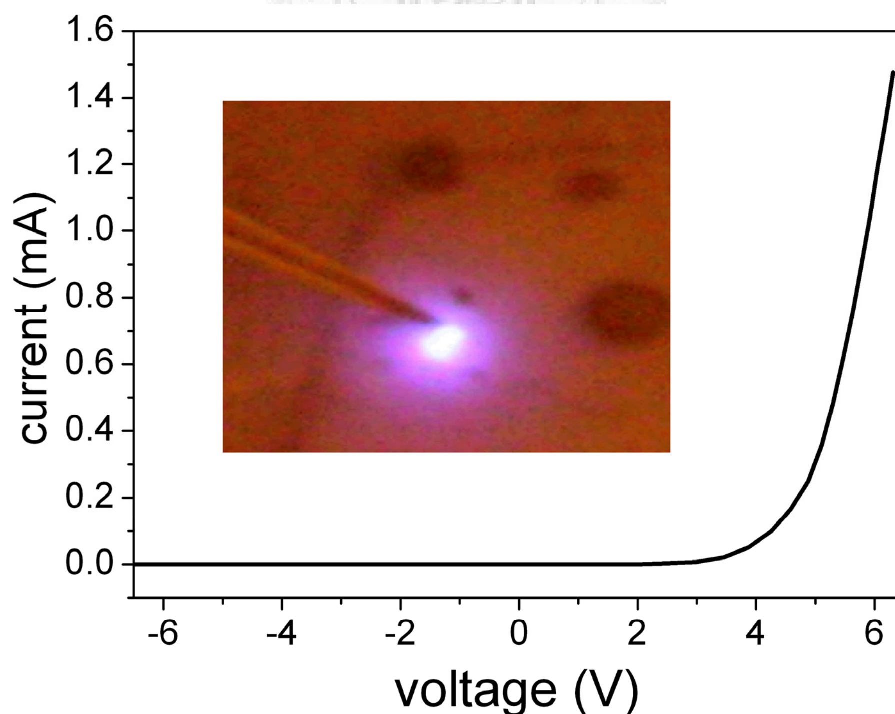

Figure 4.7 I-V curve of the n-ZnO/p-GaN heterojunction LED. The insets show the EL image of the n-ZnO/p-GaN heterojunction LED.

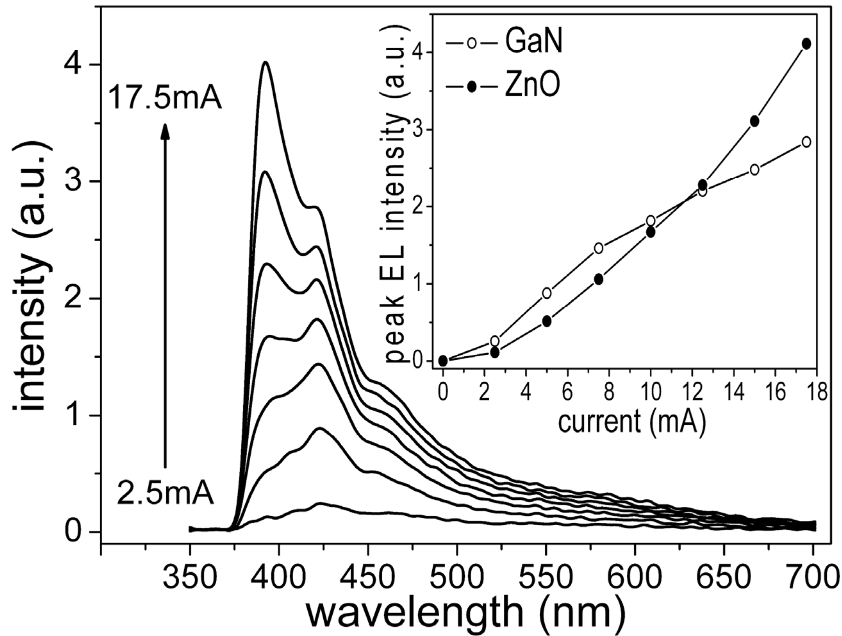

Figure 4.8 Room temperature EL spectra of the *n*-ZnO/*p*-GaN heterojunction LED at various DC injection currents. The inset shows the EL peak intensities of the *n*-ZnO (λ=391 nm) and *p*-GaN (λ=425 nm) as a function of the injection current.

spectra in the present study show the superposition of light emissions form both the *n*-ZnO and *p*-GaN layers. Inset of figure 4.8 depicts the EL peak intensities of the *n*-ZnO and *p*-GaN as a function of the injection current. Competition between the emissions at 391 nm and 425 nm might result from the differences in the carrier concentration and the light emission efficiency in *n*-ZnO and *p*-GaN, as well as the ZnO/GaN interface states, which will be discussed later.

4.2.6 Interfacial layer

The thickness of the interfacial layer is about 4~5 nm as seen in high-resolution (HR) TEM images in Fig. 4.9(a) and (b). The interface is composed of crystals apparently different from the adjoining GaN and ZnO single crystals where

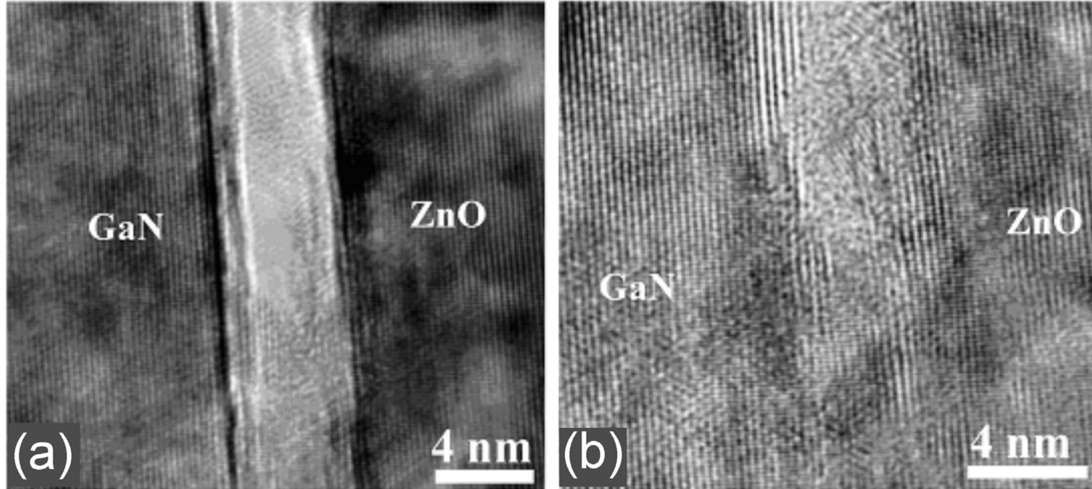

Figure 4.9 (a) and (b) are High-resolution TEM images of the interfacial layer between ZnO and GaN.

well-ordered lattice fringes, particularly of their (0001) planes, are seen. This can be seen in the electron diffraction pattern from the interfacial layer in Fig. 4.4. As compared with the diffraction pattern from ZnO it includes additional spots from an unknown crystal formed with an orientation with their *c*-axis. We have not yet characterized the phase in the interfacial layer. Since the ALD can make an abrupt interface over a large area, the interfacial layer might be formed rather during the post heat treatment of RTA than by ALD. Such high-temperature annealing can cause the diffusion of the Mg atoms in the *p*-GaN layer toward the interface between *n*-ZnO and *p*-GaN, and consequently the interfacial layer between ZnO and GaN can be formed. Such diffusion cannot proceed uniformly over the interface as is usual with a heat treatment. An evidence of diffusion of Mg atoms can be seen as bright contrast in the *p*-GaN layer in figure 4.10, which is a high-angle annular dark-field (HAADF) scanning transmission electron microscopy (STEM) image of the *n*-ZnO/*p*-GaN on the GaN layer. The HAADF-STEM images are mainly formed by thermal diffuse

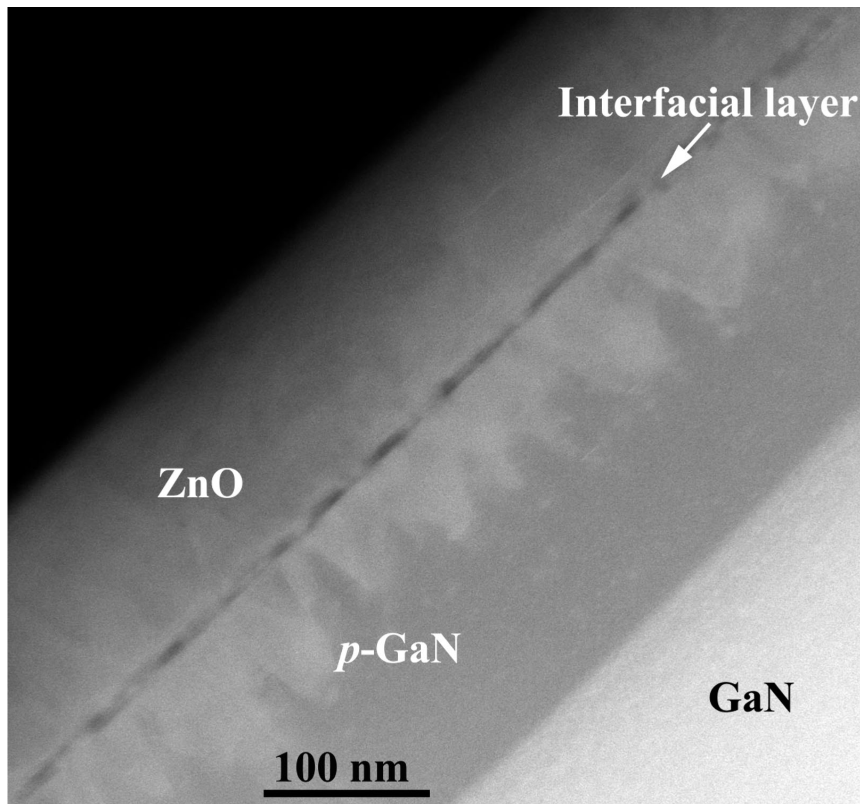

Figure 4.10 High-angle annular dark-field scanning transmission electron microscopy image of the *n*-ZnO/*p*-GaN heterojunction on the GaN layer.

provide the Z-contrast, approximately proportional to the square of the atomic number [12,13]. Therefore, contrast of the p-GaN darker than the underlying $Ga^{31}N^{7}$ is ascribed to doped Mg^{12} atoms, and the parts exhibiting brighter contrast in the p-GaN are poor in concentration of Mg atoms, which were diffused out to form the interfacial phase. However, the brighter contrast was not observed in the lower portion of the p-GaN layer, indicating the preferential diffusion of Mg atoms toward ZnO, not toward the underlying GaN. This result may be ascribed to the formation of a new phase at the interface between ZnO and GaN. The phase is a compound including Mg atoms, though its crystal structure has not yet been established. The demand of Mg atoms by the new phase causes the supply of Mg from p-GaN, which is greater than the demand by the underlying GaN layer.

4.2.7 Confirm the interfacial layer by C-V method

To confirm the formation of the interfacial layer by the post-deposition RTA process, we measured the capacitance *vs.* voltage (*C-V*) characteristics of the *n*-ZnO/*p*-GaN structures. The *C-V* curves of the *n*-ZnO/*p*-GaN samples *with* and *without* the RTA treatment are shown in figure 4.11. The measurement was conducted using an HP 4284A LCR meter at RT. The GaN electrode was grounded and the voltage was applied to the ZnO electrode. The measurement ac frequency was 10 kHz. As compared with the unannealed sample, the significant increase in the capacitance with the applied voltage from 0 to 5V for the annealed sample is very similar to the typical feature of carrier inversion in the low-frequency *C–V* characteristics. This suggests the presence of a wide-bandgap interfacial layer caused by the diffusion of the Mg atoms in the *p*-GaN layer toward the *n*-ZnO/*p*-GaN interface during the RTA treatment [14]. It is reasonable to identify this wide-bandgap layer with the interfacial layer observed by TEM.

The band diagram of the *n*-ZnO/*p*-GaN heterojunction including this interfacial layer was constructed using the Anderson model and is presented in Fig. 4.12 (a), which is similar to one presented by Lee and Kim [14]. As shown in Fig. 4.5 and figure 4.9 (b), the interfacial layer is so thin (4~5 nm) as to allow the carriers to tunnel through, as indicated by the forward bias in the *I-V* curve. Since the electron concentration in ZnO is up to 2×10^{18} cm^{-3}, it is difficult to form an inversion layer (holes) in ZnO near the ZnO/GaN interface. However, it has been reported that the surface inversion in *p*-GaN can be achieved if there exist minority carrier sources such as *n*-type region and dislocations [15-17]. As a result, the remarkable increase in the capacitance with the applied voltage from 0 to 5V for the annealed sample might be attributed to the accumulation of minority carriers (electrons) in *p*-GaN or the carrier emission and capture associated with the interface states near the ZnO/GaN

interface [18]. The electrons were provided by the interface states or from the undoped (intrinsic *n*-type) GaN region beneath the *p*-GaN layer, as shown schematically in Fig. 4.12 (b). On the other hand, the slow increase in the capacitance with the applied voltage greater than 5V for the annealed samples probably results from the carrier emission from the deep-level states distributed in ZnO or GaN. At low positive applied voltages, the low carrier emission probability effect) [19] causes the carriers in these deep-level states do not contribute significantly to the capacitance. As the positive applied voltage increases, the increase in the probability of carrier emission from the deep-level states (proportional to a squared electric field E^2 in the multiphonon- assisted tunneling process) [19] facilitates the response of the carriers in the deep-level states to the measurement ac frequency. Thus the capacitance increases with the applied voltage greater than 5V. The carrier emission from the deep-level states in ZnO or GaN may be also the reason

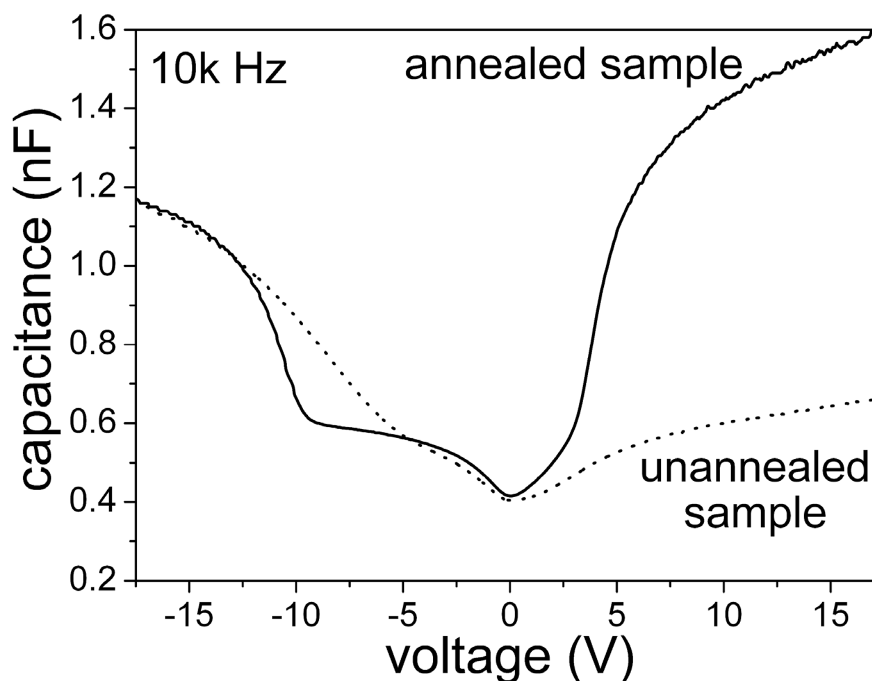

Figure 4.11 Capacitance *vs.* voltage (*C-V*) curves of the *n*-ZnO/*p*-GaN structures *with* and *without* the RTA treatment.

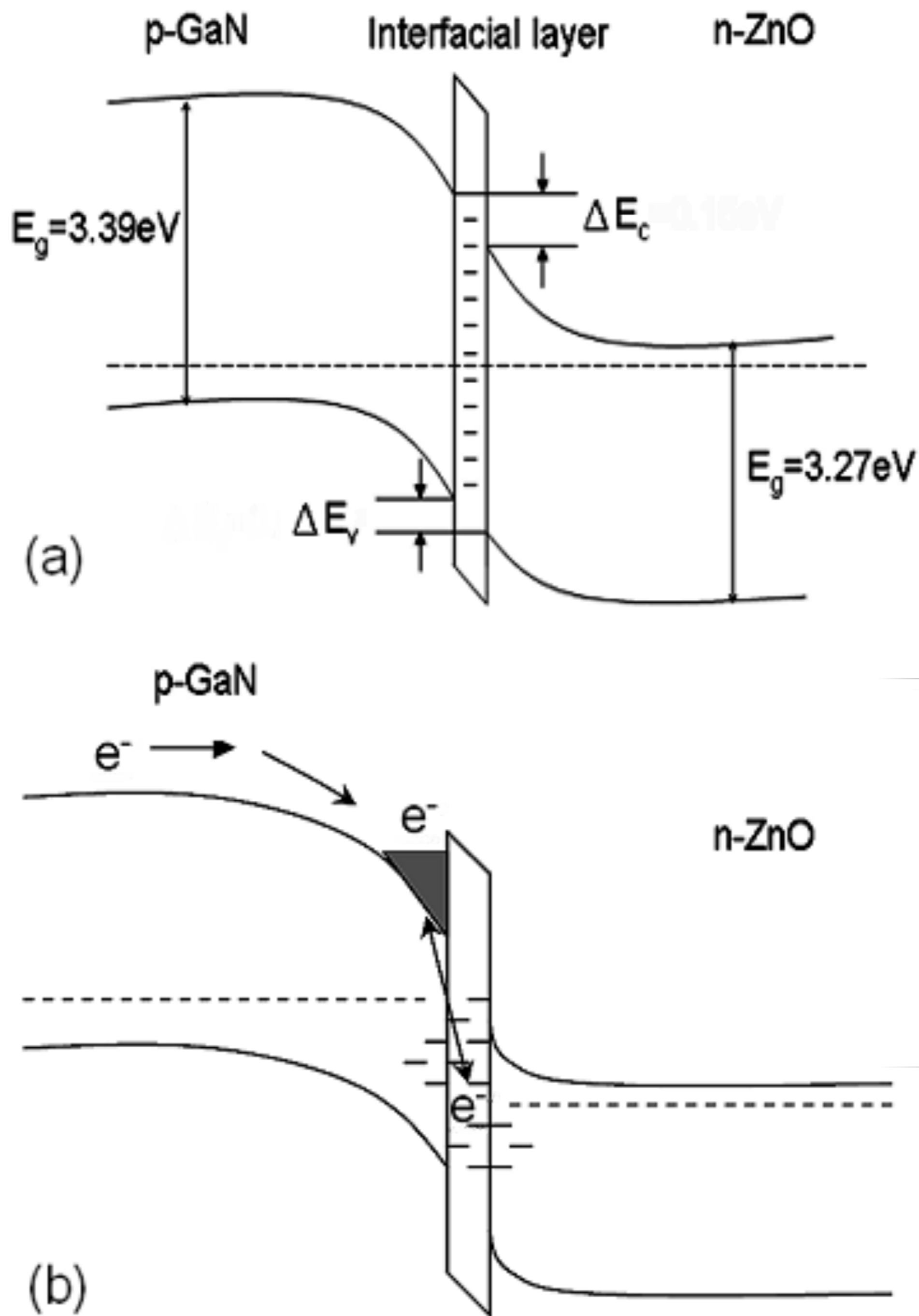

Figure 4.12 (a) Band diagram of the *n*-ZnO/*p*-GaN heterojunction without applying voltage. (b) Band diagram of the *n*-ZnO/*p*-GaN heterojunction. The GaN electrode is grounded and the positive voltage is applied to the ZnO electrode (reverse bias for the *pn* junction).

(proportional to a square root of the electric field $\sqrt{E}$ due to the Poole-Frenkel for the slow increase in the capacitance with the positive bias for the unannealed sample. As for the negative applied voltage (forward bias for the *pn* junction), the increase in the capacitance with the negative applied voltage may result from the rearrangement of the minority carriers in response to the measurement ac frequency (diffusion capacitance) [20]. The ZnO/GaN interface states caused by the interdiffusion between the ZnO and GaN during the RTA treatment may be responsible for the distortion of the *C-V* curve of the annealed sample at a voltage about -10V [18,20].

4.2.8 Competition mechanism

Competition between the emissions at 391 nm and 425 nm shown in Fig. 4.8 might result from the differences in the carrier concentration and the light emission efficiency in *n*-ZnO and *p*-GaN, as well as the ZnO/GaN interface states. Because of the higher carrier concentration in *n*-ZnO, the amount of electrons injected from *n*-ZnO is much larger than the holes injected from *p*-GaN at forward bias [3,5-7]. When the carriers transport across the interfacial layer, they may be trapped at the ZnO/GaN interface states [14]. At a low injection current of 2.5 mA, the interface states may capture large amount of the holes injected from *p*-GaN. However, only a small portion of electrons injected from *n*-ZnO are trapped by the interface states since the electron injection current is much larger than the hole injection current. Accordingly, the emission from ZnO is not obvious and the EL from GaN dominates the spectrum. As the injection current increases, the holes injected from *p*-GaN not only fill up the interface states but also enter into the *n*-ZnO layer. As a result, even although the electron injection into *p*-GaN is higher than the hole injection into *n*-ZnO, the EL form *n*-ZnO increases rapidly and eventually dominates over the emission from *p*-GaN due to the higher light emission efficiency in ZnO.

On the other hand, the EL peak at 391 nm longer than the PL peak of ZnO at 378 nm can be attributed to the presence of the interfacial layer between *n*-ZnO and *p*-GaN. The electrons and holes may accumulate in ZnO and GaN near the interface, respectively, due to the wide bandgap energy of the interfacial layer. The accumulated electrons might cause a slight decrease in the ZnO bandgap energy as a result of bandgap renormalization. These electrons recombine with the holes supplied from *p*-GaN to produce EL. Because of the valence band offset ΔE_v (shown schematically in Fig. 4.12 (a)) as well as the bandgap renormalization, the photon energy of EL peak is smaller than the ZnO bandgap. Actually, a similar phenomenon with an EL peak at 394 nm has been observed from the *n*-ZnO/*p*-GaN heterojunction LED with a thin SiO_2 layer inserted between ZnO and GaN [21]. The UV EL from ZnO at a DC low injection current about 10 mA indicates a high optical quality of the ALD-deposited ZnO epilayer treated by the post-deposition RTA process. Furthermore, the ZnO epilayers have large-area uniformity and good reproducibility owing to the advantages of ALD. On the other hand, the *n*-ZnO/*p*-GaN heterojunction LEDs *without* the RTA treatment do not exhibit any EL from ZnO. As a result, even although the RTA treatment induces the ZnO/GaN interfacial layer as indicated by the TEM and *C-V* measurements, the UV EL and PL with negligible defect-related bands from ZnO suggest that these interface states do not seriously degrade the light emission from ZnO.

4.3 Electroluminescence of *n*-ZnO/*p*-GaN heterojunction LED with aluminum back reflector

4.3.1 Sample preparation

Figure 4.13 shows the schematic diagram of the devices which were deposited on a double-side polished c-Al_2O_3 substrate. In device (A), aluminum was evaporated on the back of the c-Al_2O_3 substrate as a reflector to study the effect of external optical feedback. The back side of device (B) is maintained polish, and the back side of device (C) is roughened by diamond blend.

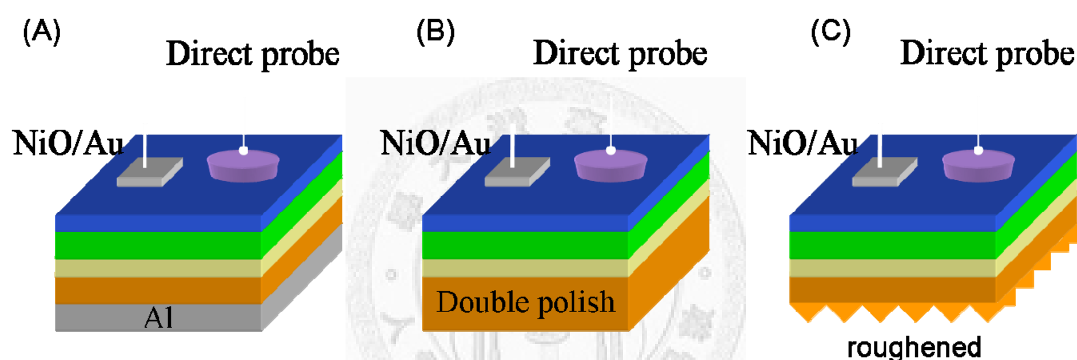

Figure 4.13 Schematic diagram of the devices. Aluminum was evaporated on the back of the c-Al_2O_3 substrate as a reflector in device (A). The back side is maintained polish in device (B). The back side is roughened by diamond blend in device (C).

4.3.2 electroluminescence

Figure 4.14 shows the EL spectra of the device **A** which was injected by pulsed currents from 300 mA to 800 mA with a pulse duration of 1 ms and a repetition rate of 64 Hz. The EL spectra were measured from top of the *n*-ZnO layer. At an injection current of 300 mA, the device exhibited a spectral peak around 425 nm. The comparison of EL and PL spectra indicate that the spectral peak around 425 nm originates from the Mg acceptor level in *p*-GaN. Increasing the injection current causes another spectral peak at 386 nm to grow rapidly and eventually dominate over

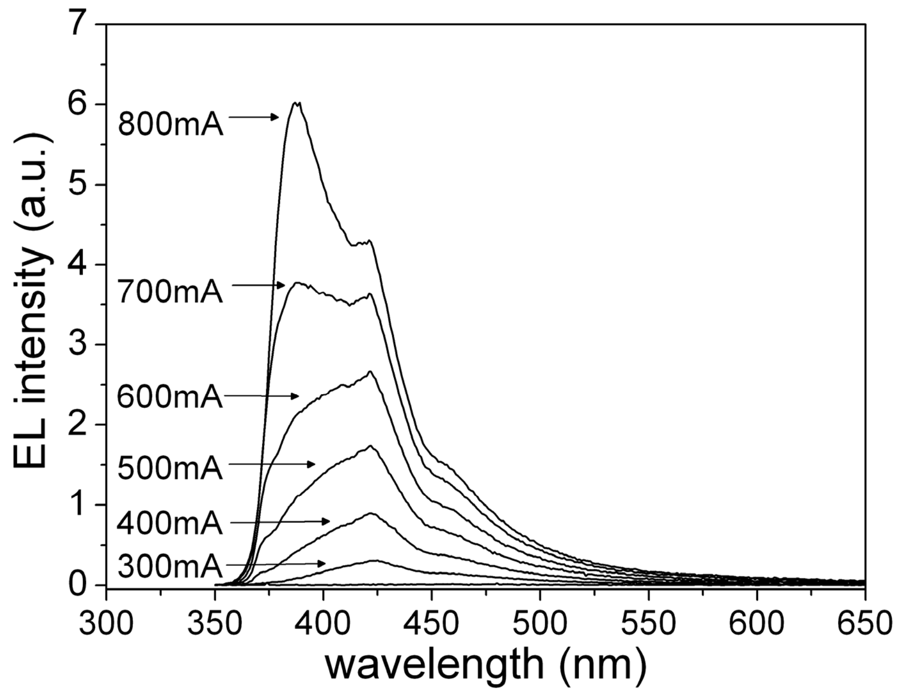

Figure 14.14 Room-temperature EL spectra of the device shown in the inset of Fig.4.13(a) at various pulsed currents from 300 mA to 800 mA. The inset is the normalized PL spectra of the *n*-ZnO and *p*-GaN layers at room temperature.

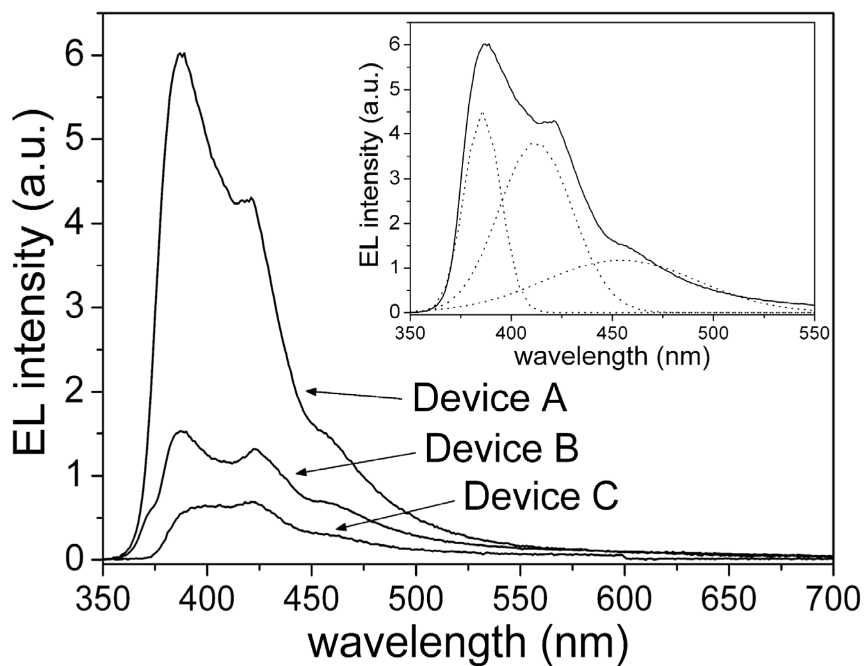

Figure 4.15 Room-temperature EL spectra of devices A, B, and C at a pulsed current of 800 mA. The inset presents the Gaussian functions (dash lines) were used to fit the EL spectra to extract the EL intensities and FWHM of ZnO and GaN..

the spectral peak at 420 nm as the current exceeds 700 mA. This EL peak at 386 nm can be attributed to light emission from the *n*-ZnO layer. The spectral shoulder around 465 nm is also ascribed to the EL from *p*-GaN.

This study also measured the EL spectra of the *n*-ZnO/*p*-GaN heterojunction LEDs with different external feedback conditions to further investigate the effect of external optical feedback. Figure 4.15 shows the EL spectra of three *n*-ZnO/*p*-GaN devices injected by the same pulsed current of 800 mA. It is clearly seen that the EL intensity of device **A** is considerably greater than that of devices **B**, and device **C** has the smallest EL intensity. It should be noted that as compared to devices **B** and **C**, the spectral peak corresponding to ZnO (λ~386 nm) of device **A** is much greater than the GaN spectral peak around 425 nm. The differences in the EL intensity and spectrum of devices **A**, **B** and **C** under the same injection current can be attributed to their distinct external optical feedback conditions.

4.3.3 Super-linearly growth of EL intensity

Figure 4.16 shows the EL peak intensity of GaN (λ~420 nm) and ZnO (λ~386 nm) as a function of injection current for all three devices at room temperature. The EL peak intensities and FWHM spectral widths of ZnO and GaN were extracted from the EL spectra fitted by the multiple Gaussian functions, as indicated by the dashed lines shown in the inset of Fig. 4.15. Figure 4.16(a) clearly presents that the EL peak intensity of GaN increases linearly with the injection current for all three devices. On the other hand, Fig. 4.16(b) shows that the EL peak intensity of ZnO in device A increases rapidly with the injection current, showing a remarkable *superlinear* dependence on the injection current. However, devices B and C exhibited little increase in the ZnO EL peak intensity with the injection current. In addition,

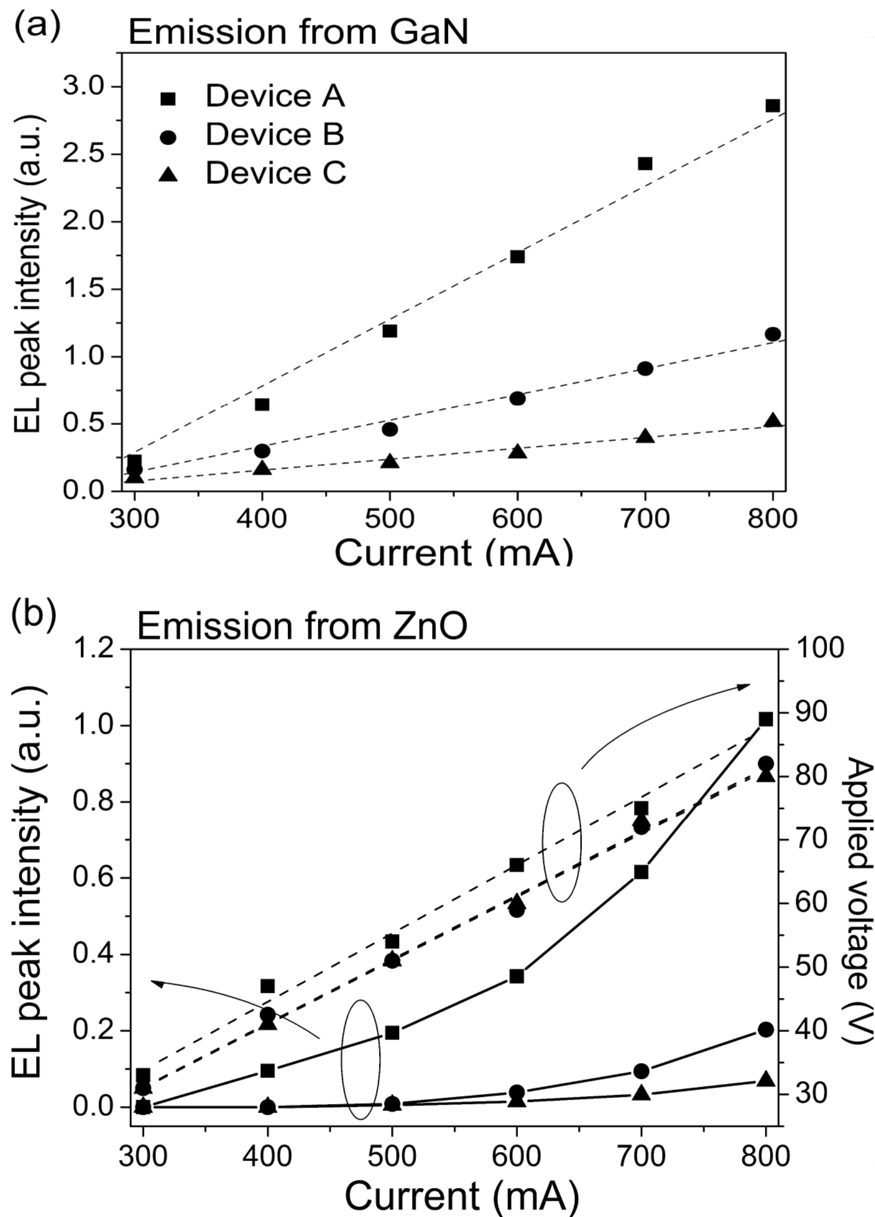

Figure 4.16 (a) The EL peak intensity as a function of the injection current of devices A, B, and C for GaN. (b) The EL peak intensity (solid line) and applied voltage (doted line) as a function of the injection current of the three devices for ZnO. The inset in (b) shows the variations of the FWHM of ZnO spectral peak with injection current for devices A, B and C.

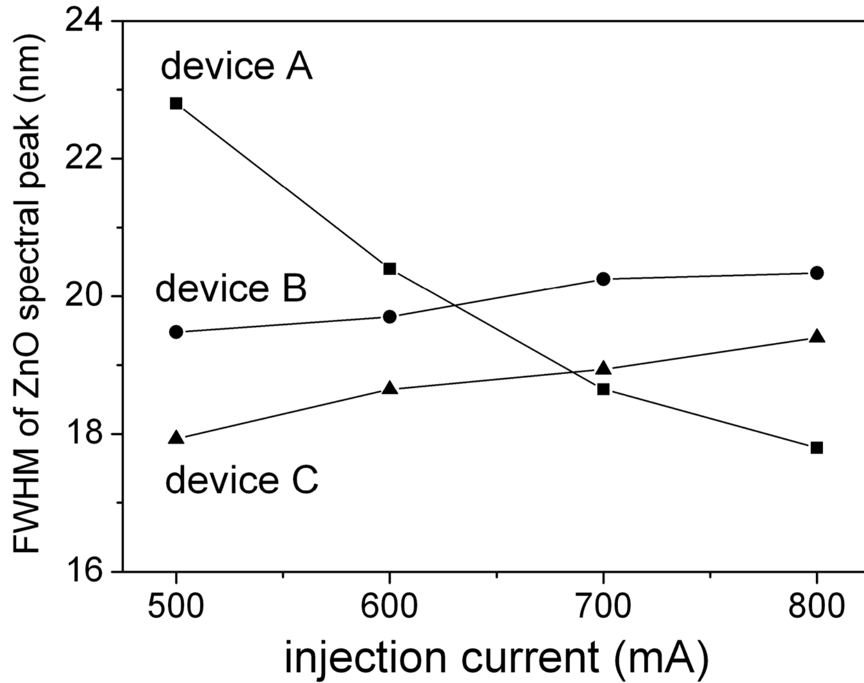

Figure 4.17 Variations of the FWHM of ZnO spectral peak with injection current for devices A, B and C.

Fig.4.16(b) also shows the applied voltage had a linear dependence on the injection current, suggesting that the *superlinear* increase in the ZnO EL intensity with the injection current did *not* result from the applied voltage. The Fig.4.17 presents the variations of FWHM of ZnO spectral peak with injection current for device A, B and C. It can be seen that the FWHM of ZnO spectral peak decreases with the injectioncurrent in device A, while the decreasing tendency of FWHM with injection current was *not* observed in devices B and C. The significant enhancement of the EL intensity from ZnO more than twofold, spectral narrowing, coupled with the super-linear increase in the ZnO EL intensity with the injection current, strongly suggests that the external optical feedback from the polished back surface with an aluminum reflector stimulates light emission from the ZnO epilayer.

Chapter 3 has demonstrated that stimulated emission is facile to achieve in a high-quality ZnO epilayer grown by the ALD technique. A ZnO epilayer grown on a

c-Al_2O_3 substrate by ALD exhibited optically pumped stimulated emission with a threshold intensity as low as 35.1 kW/cm^2 at room-temperature. For a reference, the optical gain coefficient at λ=386 nm of the *n*-ZnO layer in the *n*-ZnO/*p*-GaN structure was measured by the variable stripe length (VSL) technique. It was shown that the ASE intensity at λ=386 nm increases *superlinearly* with the excitation length. The analysis using one-dimensional optical amplifier model indicates that the gain coefficient at λ=386 nm can reach a value as high as 367 cm^{-1}. Stimulated emission in ZnO is associated with the excitonic scattering/recombination processes and analogous to a four-level laser system, which is illustrated in Appendix 4A and Ref. [22]. Population inversion might be established in the ZnO epilayer at high injection currents. For device A, the aluminum back reflector leads to the reflection of much photons into the *n*-ZnO layer. Thus the spontaneous emission from ZnO was amplified, resulting in spectral narrowing and *superlinear* increase in the UV EL intensity with the injection current. As for devices B and C, the poor external optical feedback conditions cause less photons to be reflected back into the *n*-ZnO layer, thus suppressing the increase in the EL intensity with the injection current.

4.4 Summary

The n-ZnO/*p*-GaN heterojunction LEDs were fabricated by the growth of n-ZnO epilayer using ALD on the p-GaN. The specimen was treated with a post-deposition RTA at 950°C for 5 min in N_2 atmosphere. The XRD, XRC and TEM characterizations demonstrate that the ZnO epilayer has high (0002) orientation and good crystal quality. TEM observations also reveal that the ZnO grows in good epitaxial relation with GaN and to almost a perfect single crystal with a very few dislocations. It has been found that the threading dislocations from the underlying layers reduce at the interface between GaN and ZnO, due to the layer-by-layer growth

of ALD and the recrystallization during the post heat treatment of RTA. The TEM and HAADF-STEM images reveal that an interfacial layer 4~5 nm thick along the interface between ZnO and p-GaN was formed by the diffusion of Mg atoms from the p-GaN during the RTA treatment. The capacitance and voltage (C-V) characteristics confirm the presence of the interfacial layer. At a low injection current, light emission from the Mg acceptor levels in p-GaN is obvious. Increase in the forward bias causes dominant emission from n-ZnO. Competition between the ELs from ZnO and GaN is elucidated to be attributed to the interfacial layer as well as the differences in the light emission efficiency and the carrier concentration in n-ZnO and p-GaN layers. The achievement of UV EL at a low DC injection current from ZnO indicates that the ZnO epilayers grown by the ALD technique are effectually applicable to the next-generation short-wavelength photonic devices.

An aluminum external-feedback reflector was evaporated on the back of the double-polished c-Al_2O_3 substrate. Remarkable enhancement of the UV EL intensity, superlinear increase in the EL intensity, coupled with the spectral narrowing, from ZnO with the injection current are attributed to the external optical feedback and ASE in the high-quality ZnO epilayer. The achievement of the electrically pumped ASE in a ZnO epilayer grown by ALD indicates that the ALD technique is applicable to the high-quality ZnO for next-generation UV photonic devices.

Appendix 4A: four-level laser system

Significant enhancement of the EL intensity from ZnO more than twofold, spectral narrowing, coupled with the *superlinear* increase in the ZnO EL intensity with the injection current, are attributable to amplified spontaneous emission (ASE) in the high-quality ZnO epilayer caused by the aluminum back reflector. According to *Semiconductor Optics* (Springer, 3rd edition, 2006) and Ref.22 authored by Prof. Claus Klingshirn, stimulated emission in ZnO is associated with the excitonic scattering/recombination processes and analogous to a four-level laser system. In a four-level laser system as shown in Fig.4A-1 in this letter, as long as the lifetime of the transition from E3 to E2 is longer than that from E4 to E3, a population accumulates in the level E3. Thus population inversion is established and accordingly stimulated emission can take place. In our work, a large number of electrons and holes were injected into the ZnO layer and formed excitons. The scattering between excitons caused some excitons rising to a higher energy level, just like the level E4 in Fig.A, and some went down to the lower energy level like E3 in Fig.A. The transition

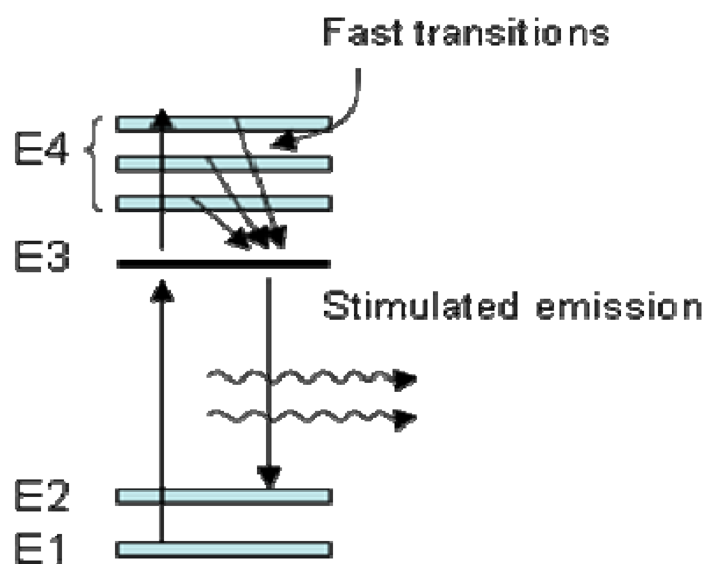

Figure 4A-1 Schematic diagram of four-level laser system

from level E4 to E3 is faster than that from E3 to E2. Therefore, population inversion was established in the ZnO layer. As the light emission from ZnO was reflected by the aluminum back reflector, the spontaneous emission from ZnO was amplified, resulting in the enhancement of the EL intensity more than twofold, spectral narrowing, and the superlinear increase in the ZnO EL intensity with the injection current.

Reference

[1] D. C. Look, B. Claflin, Ya. I. Alivov and S. J. Park, Phys. Stat. Sol. (a), vol.201, pp.2203-2212, 2004.

[2] X. H. Pan, J. Jiang, Y. J. Zeng, H. P. He, L. P. Zhu, Z. Z. Ye, B. H. Zhao and X. Q. Pan, J. Appl. Phys., vol.103, 023708, 2008.

[3] Ya. I. Alivov, J. E. Van Nostrand, D. C. Look, M. V. Chukichev and B. M. Ataev, Appl. Phys. Lett., vol.83, pp.2943-2945, 2003.

[4] D. J. Rogers, F. Hosseini Teherani, A. Yasan, K. Minder, P. Kung and M. Razeghi, Appl. Phys. Lett., vol.88, 141918, 2006.

[5] S. J. Jiao, Y. M. Lu, D. Z. Shen, Z. Z. Zhang, B. H. Li, J. Y. Zhang, B. Yao, Y. C. Liu and X. W. Fan, Phys. Stat. Sol. (c), vol.3, pp.972-975, 2006.

[6] H. Y. Xu, Y. C. Liu, Y. X. Liu, C. S. Xu, C. L. Shao and R. Mu, Appl. Phys. B, vol.80, pp.871-874, 2005.

[7] R. W. Chuang, R. X. Wu, L. W. Lai, and C. T. Lee, Appl. Phys Lett., vol.91, 231113, 2007.

[8] H. S. Yang, S. Y. Han, Y. W. Heo, K. H. Baik, D. P. Norton, S. J. Pearton, F. Ren, A. Osinsky, J. W. Dong, B. Hertog, A. M. Dabiran, P. P. Chow, L. Chernyak, T. Steiner, C. J. Kao, G. C. Chi, Jpn. J. Appl. Phys., vol.44, pp.7296-7300, 2005.

[9] Y. Chen, D. Bagnall and T. Yao, Mater. Sci. Eng. B, vol.75, pp.190-198, 2003.

[10] U. Kaufmann, M. Kunzer, M. Maier, H. Obloh, A. Ramakrishnan, B. Santic and P. Schlotter, Appl. Phys. Lett., vol.72, pp.1326-1328, 1998.

[11] S. H. Lim, D. Shindo, H. B. Kang and K. Nakamura, J. Vac. Sci. Technol. B vol.19 pp.506-510, 2001.

[12] S. J. Pennycook and P. D. Nellist, Impact of Electron and Scanning Probe Microscopy on Material Research (Kluwer, Dordrecht), pp.161–207, 1999.

[13] M. Shiojiri and H. Saijo, J. Microsc., vol.223, pp.172-178, 2006.

[14] S. Lee and D. Y. Kim, Materials Sci. Engineer. B, vol.137, pp.80-84, 2007.

[15] J. Kim, R. Mehandru, B. Luo, F. Ren, B. P. Gila, A. H. Onstine, C. R. Abernathy, S. J. Pearton and Y. Irokawa, Appl. Phys. Lett., vol.80, pp.4555-4557, 2002.

[16] J. Kim, R. Mehandru, B. Luo, F. Ren, B. P. Gila, A. H. Onstine, C. R. Abernathy, S. J. Pearton and Y. Irokawa, Appl. Phys. Lett., vol.81, pp.373-375, 2002.

[17] Y. Nakano, T. Kachi and T. Jimbo, J. Vac. Sci. Technol. B, vol.21, pp.2220-2222, 2003.

[18] E. H. Nicollian and J. R. Brews, MOS (Metal Oxide Semiconductor) Physics and Technology, Wiley, New York, 1982.

[19] I. E. Titkov, A. S. Zubrilov, L. A. Delimova, D. V. Mashovets, I. A. Linichuk and I. V. Grekhov, Semiconductors, vol.41, pp.564-569, 2007.

[20] S. M. Sze and K. K. Ng, Physics of Semiconductor Devices, 3rd ed., Wiley, New York, 2007.

[21] C. P. Chen, M. Y. Ke, C. C. Liu, and Y. J. Chang, F. H. Yang, J. J. Huang, Appl. Phys. Lett., vol.91, 091107, 2007.

[22] C. Klingshirn, R. Hauschild, J. Fallert and H. Kalt, Phys. Rev. B, vol. 75, 115203, 2007.

Chapter 5

White Light and UV Electroluminescence of *n*-ZnO /*p*-GaN Hetrojunction Light-Emitting Diodes at Reverse Breakdown Bias

5.1 Introduction

ZnO has recently attracted considerable attention as a promising material for ultraviolet (UV) light-emitting devices due to its large exciton binding energy of 60 meV and many benefits such as long-term stability, relatively low material costs, *etc* [1]. Various techniques have been applied to prepare ZnO films and nanorods with high crystal quality and good optical characteristics [2]-[5]. Among these techniques, atomic layer deposition (ALD) is a noteworthy technique for growing high-quality ZnO films [6],[7]. The advantages of ALD include easy and accurate thickness control, high uniformity over a large area, low defect density, conformal step coverage, good reproducibility, and low growth temperatures.

Although ZnO technology has substantially been progressing, it is difficult to prepare stable *p*-type ZnO films with high hole concentration [8],[9]. Since ZnO and GaN have the same crystal structure (wurtzite) with a small in-plane lattice mismatch (1.8%), *p*-type GaN would be substituted for *p*-ZnO. Actually, many studies have reported on the *n*-ZnO/*p*-GaN heterojunction light-emitting diodes (LEDs) operated at forward bias [10]-[15]. However, a type II *n*-ZnO/*p*-GaN heterojunction with a large band offset limits the carrier transport across the junction at forward bias, while facilitates the reverse breakdown associated with band-to-band tunneling [16]. On the other hand, field-stimulated ionization of deep-level states was also proposed to account for the breakdown and white-light luminescence at reverse bias [17]. Therefore, substantial attentions have been paid to the light emission from *n*-ZnO/*p*-GaN hete-

rojunction LEDs under reverse breakdown bias [18],[19].

In this chapter, we present white-light emission from the *n*-ZnO/*p*-GaN hetrojunction LEDs operated at reverse breakdown bias. Theoretical models based on field-assisted tunneling from a bound state to a continuum of free states and from *p*-side valance band to *n*-side conduction band are applied to explain the observed current-voltage (*I-V*) characteristics at reverse breakdown bias. And also excitonic Franz-Keldysh effect in ultraviolet electroluminescence from *n*-ZnO:Al/*p*-GaN heterojunction LEDs.

5.2 White-light Electroluminescence

5.2.1 Sample preparation

Figure 5.1 shows a schematic diagram of the *n*-ZnO/*p*-GaN heterojunction LED. First, a thin GaN buffer layer with 30 nm in thickness was deposited on a *c*-Al_2O_3 substrate, and then a 2.5 μm thick undoped GaN layer was grown upon the buffer layer by metal organic chemical vapor deposition (MOCVD). A 300 nm thick Mg-doped GaN layer was subsequently grown also by MOCVD. The hole concentration in this layer was approximately 2.6×10^{17} cm^{-3}. Afterwards, a 540 nm thick ZnO layer was grown on the *p*-GaN at 180°C using the ALD technique. Diethylzinc (DEZn, $Zn(C_2H_5)_2$) and H_2O vapor were utilized as the precursors for zinc and oxygen. The ALD process consisted of 3000 identical cycles, each of which contained the following sequence: DEZn, 0.01s $\rightarrow$ N_2 purge, 5s $\rightarrow$ H_2O, 0.1s $\rightarrow$ N_2 purge, 5s, and deposited ~ 1.8 Å of ZnO. After deposition, the specimen was treated by RTA at 950 ^{o}C for 5 min in N_2 atmosphere to improve the crystal quality of the ZnO layer. The above processing parameters had been investigated as the optimal ZnO growth condition in our previous studies [7],[20]-[22]. Hall effect measurement

revealed that the electron concentration in the ZnO layer was 2×10^{18} cm^{-3}, showing intrinsic *n*-type characteristics. The X-ray diffraction pattern presented that the *n*-ZnO layer was highly *c*-axis orientated. The full-width at half-maximum (FWHM) of the X-ray rocking curve for the ZnO (0002) peak was 424 arcsec, indicating the high crystallinity of the ZnO layer grown by ALD. Transmission electron microscopy (TEM) observations also revealed that the ZnO grew in good epitaxial relation with GaN and exhibited almost a perfect single crystal with a very few dislocations [22]. Circular ZnO mesa with 1 mm in diameter was then fabricated by conventional lithography and chemical etching using a dilute HCl solution. Ohmic contact to *p*-GaN was made by thermal evaporation of Ni/Au, followed by annealing at 500°C for 30 min in O_2 ambient. The ohmic contact of the Ni/Au electrode on *p*-GaN is confirmed from the linearity of current-voltage (*I-V*) curve between two Ni/Au

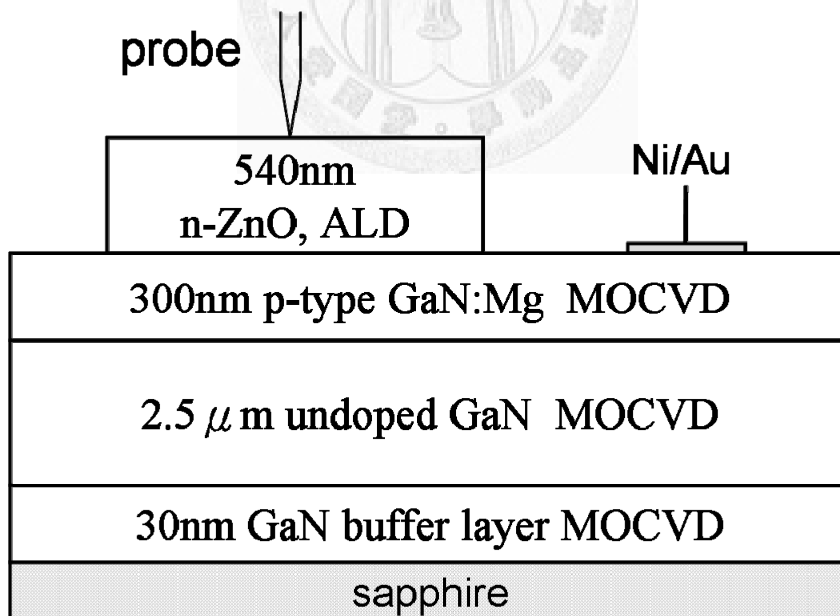

Figure 5.1 Device structure of the *n*-ZnO/*p*-GaN hetrojunction LED.

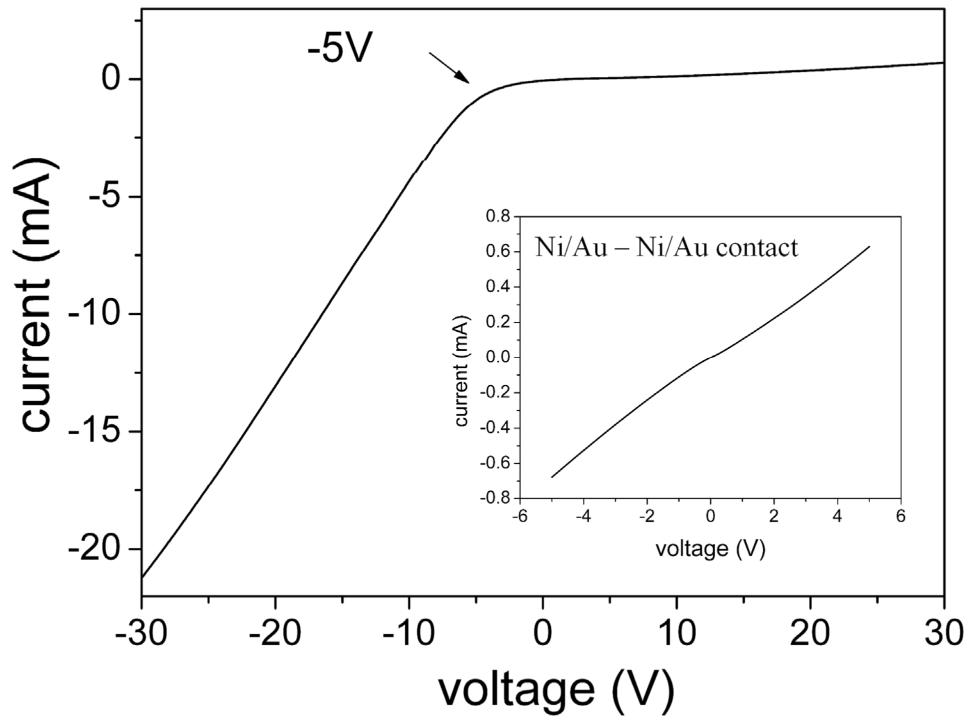

Figure 5.2 Room-temperature *I-V* curve of the *n*-ZnO/*p*-GaN heterojunction LED. The inset shows the *I-V* curve of two Ni/Au contacts on *p*-GaN.

electrodes on *p*-GaN displayed in the inset in Fig.5.2. No metal electrode was deposited on top of the ZnO layer to avoid blocking the light emission from the underlying region. Direct probe on top of *n*-ZnO layer was applied for the current injection into the LED.

5.2.2 Current *vs.* voltage (*I-V*) characteristics

Figure 5.2 shows the *I-V* curve of the *n*-ZnO/*p*-GaN hetrojunction LED at room temperature. A large series resistance was seen at forward bias and reverse breakdown around -5V was clearly observed. The type II band alignment with large band offsets between *n*-ZnO and *p*-GaN results in a low injection current at forward bias [16]. However, the current increased rapidly with the reverse bias as the applied negative voltage was greater than the breakdown voltage. Since the breakdown

voltage is less than $4E_g/q$, where E_g (~3.4 eV) is the bandgap energy of ZnO or GaN, the breakdown can not be attributed to the avalanche multiplication, but might be caused by the tunneling effect [23]. The detailed breakdown mechanism and its related luminescence will be discussed in the following.

5.2.3 Optical and crystal quality

Figure 5.3 shows the normalized photoluminescence (PL) spectra of the *n*-ZnO and *p*-GaN layers measured at room temperature using a He-Cd laser (λ=325 nm) as the excitation source. The *n*-ZnO layer exhibited a significant near-band-edge (NBE) UV emission from free excitons at 378 nm and negligible defect-related bands, indicating a good optical quality of the *n*-ZnO layer grown by ALD. On the other hand, a deep-level emission around 430 nm appeared in the PL spectrum of *p*-GaN,

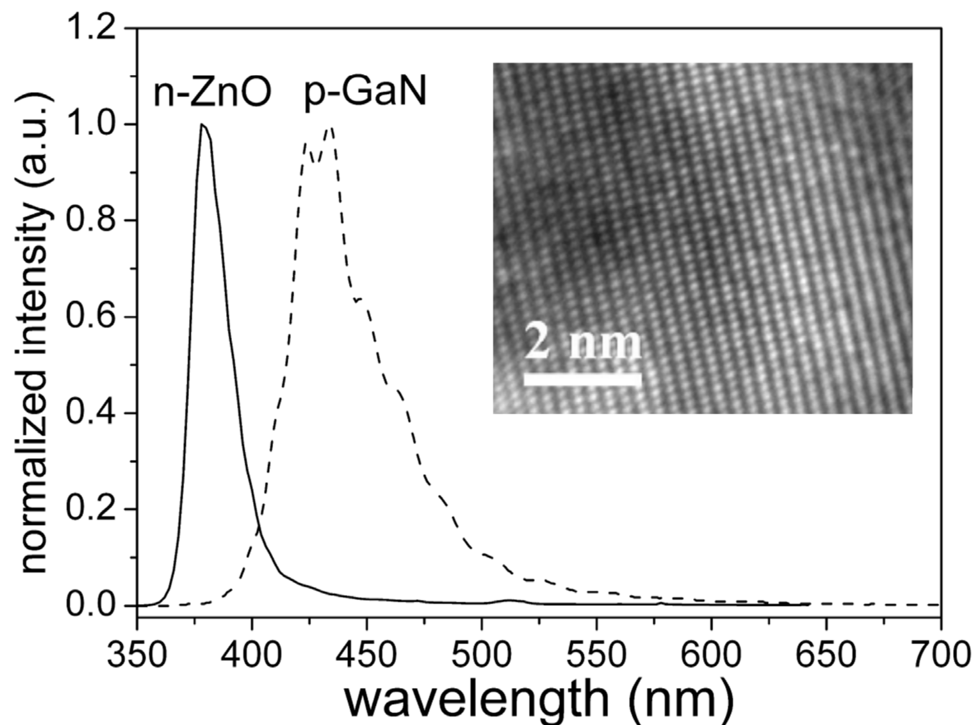

Figure 5.3 Room-temperature PL spectra of the *p*-GaN layer and the thick (540 nm) *n*-ZnO layer grown on the *p*-GaN. The inset is the HRTEM image of this thick *n*-ZnO layer in the region near the top surface.

which is ascribed to the transitions from the conduction band or unidentified shallow donors to the Mg acceptor levels [24]. Note that the NBE emission from *p*-GaN was not observed, which might result from the complete dissociation of the Mg-H complexes to the Mg acceptors in a thin *p*-GaN film with a thickness of only 300 nm [16].

5.2.4 White light electroluminescence

Figure 5.4 shows the EL spectra of the *n*-ZnO/*p*-GaN hetrojunction under the DC injection currents from 1 mA to 15 mA at the reverse breakdown biases. The oscillating-like peaks upon the EL spectra can be attributed to the effect of Fabry-Perot cavity formed by the ZnO/air and GaN/sapphire interfaces [25]. Two Gaussian functions were applied to fit the EL spectrum measured at 15 mA, as indicated by the dotted curves in Fig.5.4. It can be seen that the spectrum was composed of a blue light located at 450 nm and a broad yellow band around 550 nm. Comparing the EL and PL spectra reveals that the spectral peak at 450 nm is attributable to the light emission from the Mg acceptor levels in *p*-GaN. However, the yellow band around 550 nm was not observed in the PL spectra of either the *n*-ZnO or *p*-GaN layers.

5.2.5 Discussion

In order to investigate the origin of this yellow band, a thin ZnO layer with only 90 nm (500 ALD cycles) in thickness was grown on the *p*-GaN. The material growth and post-deposition annealing processes were the same as those mentioned above. Figure 5.5 presents the normalized PL spectrum (solid line) of this 90 nm ZnO layer after the post-deposition RTA treatment, with the pumping laser beam incident on the ZnO surface. The spectrum consisted of a ZnO NBE emission at 380 nm and a broad yellow band located around 550 nm. A small spectral peak at 430 nm corresponds to

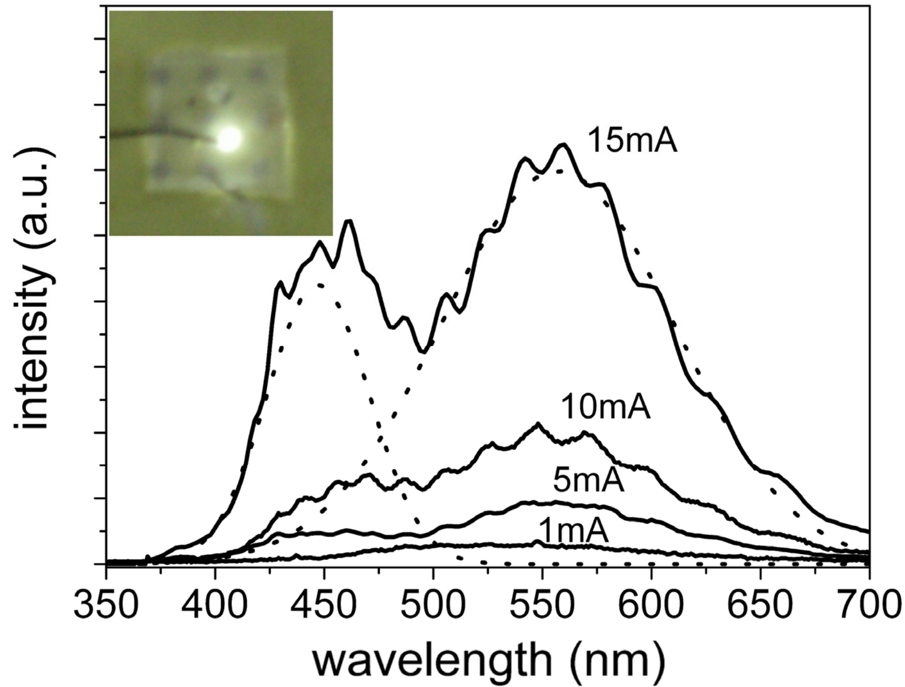

Figure 5.4 Room-temperature EL spectra of the *n*-ZnO/*p*-GaN heterojunction LED measured at various DC injection current from 1 to 15 mA under the reverse breakdown biases. The inset is the EL image of the LED in a bright room.

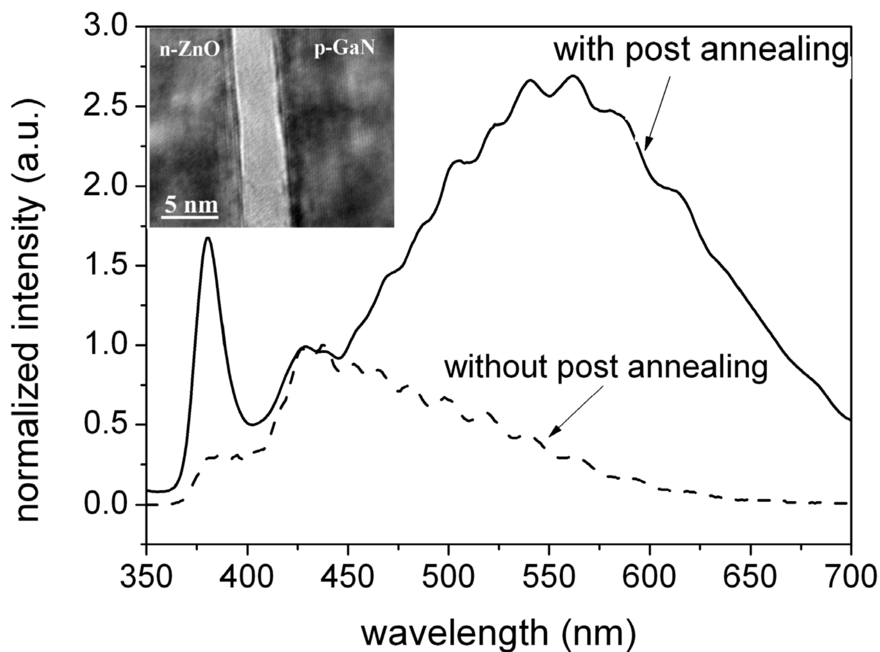

Figure 5.5 Room-temperature PL spectrum of the thin (90 nm) *n*-ZnO layer grown on the *p*-GaN *with/without* post-annealing. The inset is the HRTEM image of the interfacial layer between *n*-ZnO and *p*-GaN of the sample after the RTA treatment.

the PL from the Mg acceptor states in *p*-GaN, suggesting that the pumping laser beam can penetrate through the thin ZnO layer into the underlying *p*-GaN. A comparison between the PL spectra shown in Fig.5.3 and Fig.5.5 clearly indicates that the thick (540 nm) ZnO layer exhibited almost defect-free PL spectrum, while the defect-related yellow band around 550 nm was observed from the thin (90 nm) ZnO layer. Since the pumping laser beam at λ=325 nm cannot penetrate deeply into the thick ZnO layer due to optical absorption, the PL spectrum of the thick ZnO layer mainly originated from the region near the top surface, where the defect density was low as demonstrated by the well crystallized lattice image in a high–resolution TEM (HRTEM) image (the inset of Fig.5.3). Accordingly, only NBE emission at 378 nm appeared in the PL spectrum of the thick ZnO layer. On the other hand, the broad yellow band around 550 nm from the thin ZnO layer can be attributed to the light emission from the deep-level states related to oxygen vacancies near the interface between *n*-ZnO and *p*-GaN [26]. The inset of Fig.5.5 shows an HRTEM image of an area near the *n*-ZnO/*p*-GaN heterojunction, indicating the presence of an interfacial layer about 4~5 nm along the (0001) interface between the *n*-ZnO and *p*-GaN layers. Since the ALD technique can make an abrupt interface, the interfacial layer might be formed rather during the post-deposition RTA treatment than by ALD. Such high-temperature annealing causes the interdiffusion between *n*-ZnO and *p*-GaN, and consequently results in the formation of ZnO/GaN interfacial layer as well as the oxygen vacancies in *n*-ZnO near the interface. Thus it is reasonable to ascribe the broad yellow band around 550 nm in the PL and EL spectra to the light emission from the deep-level states associated with oxygen vacancies near the ZnO/GaN interface [26]. For a comparison, Fig. 5.5 also presents the normalized PL spectra (dashed line) of the as-deposited thin (90 nm) ZnO layer grown on *p*-GaN without post-annealing. The as-deposited ZnO layer only exhibited the superposition of light emissions at 380

nm and 425 nm, corresponding to the ZnO NBE emission and the Mg acceptor levels in *p*-GaN, respectively. The broad yellow band around 550 nm was not observed. This further confirms that the broad yellow band is evidently related to the formation of the ZnO/GaN interfacial layer and the oxygen vacancies in *n*-ZnO near the interface during the post-deposition RTA treatment.

Figure 5.6 shows the band diagram of the *n*-ZnO/*p*-GaN heterojunction under the reverse breakdown bias to illustrate the breakdown mechanism and luminescence. The electrons supplied from the underlying un-doped (intrinsic *n*-type) GaN are pulled into *p*-GaN by the large electric field at reverse bias. As these electrons drift across the *p*-GaN layer, some of them recombine with holes in the Mg acceptor levels in *p*-GaN to produce the EL at 450 nm. For the electrons reaching the ZnO/GaN interface, they would be caught by the deep-level states near the interface, thus

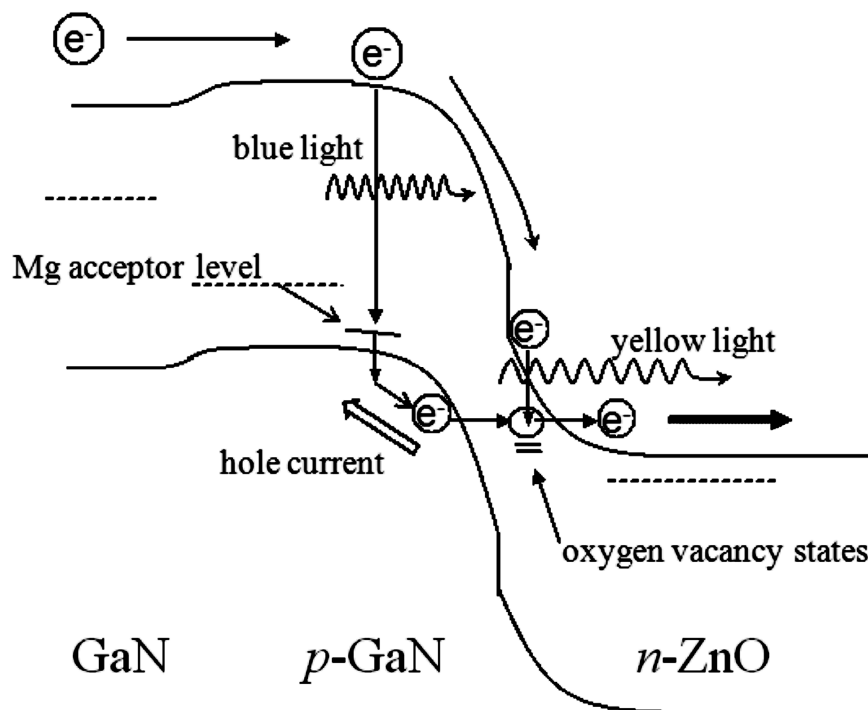

Figure 5.6 The band diagram of the undoped-GaN/*p*-GaN/*n*-ZnO of the LED under the reverse breakdown bias.

yielding the broad yellow band around 550 nm. Then the electrons in the deep-level states tunnel though the triangular energy barrier to the conduction band of *n*-ZnO, and drift out of the device. The hole current in *p*-GaN is provided by the electrons tunneling from the valence band in *p*-GaN to the deep-level states near the *n*-ZnO/*p*-GaN interface or directly to the conduction band in *n*-ZnO [16].

The tunneling rate from a bound deep-level state to a continuum of free states in a conduction band assisted by electric field can be formulated as follows [27]:

$$P = \frac{2\pi}{\hbar} \sum_f \left| \langle f | Fz | b \rangle \right|^2 \delta\left(E_f - E_b\right) \tag{5.1}$$

where $|b\rangle$ denotes the initial bound state with energy E_b, $|f\rangle$ is the final free state with energy E_f, F is the average electric field, and z is the Cartesian coordinate in the direction of the electric field. Eq.(5.1) can be simplified and the tunneling current density J can be expressed as [27]:

$$J \propto P = \frac{C_1}{F} \exp\left(-\frac{C_2}{F}\right) \tag{5.2}$$

where C_1 and C_2 are constants and this equation is deduced in Appendix 5A. The average electric field F can be estimated by

$$F = \sqrt{\frac{2q\varepsilon_p N_A N_D (\psi_{bi} - V_A)}{\varepsilon_n \left(\varepsilon_p N_A + \varepsilon_n N_D\right)}} \tag{5.3}$$

where ψ_{bi} is the built-in potential, V_A is the applied reverse bias, ε_n and ε_p are the permittivity of n and p layers, and N_A and N_D are the acceptor and donor concentrations in *p*- and *n*-type regions, respectively. On the other hand, the current associated with electrons tunneling from the occupied valence band states directly to the empty conduction band states at reverse breakdown bias is given by [28]

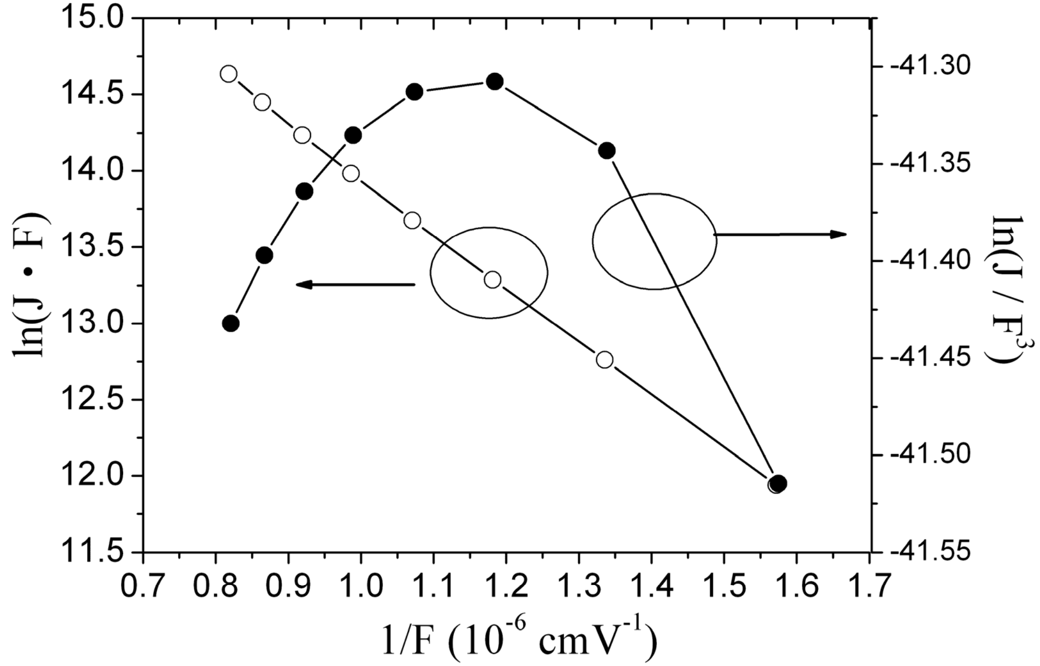

Figure 5.7 The plots of $\ln(J \cdot F)$ vs. F^{-1} and $\ln(J/F^3)$ vs. F^{-1} of the *n*-ZnO/*p*-GaN hetrojection the under reverse breakdown bias.

$$J = A \cdot F^3 \exp\left(-\frac{B}{F}\right) \tag{5.4}$$

where *A* and *B* are constants and this equation is deduced in Appendix 5B. We used Eqs.(5.2) ~ (5.4) to examine the *I-V* characteristics of the LED at reverse breakdown bias in terms of $\ln(J \cdot F)$ vs. F^{-1} and $\ln(J/F^3)$ vs. F^{-1} plots, as shown in Fig.5.7. The obvious linear dependence between $\ln(J \cdot F)$ and F^{-1} clearly indicates that the reverse breakdown is dominated by the electrons tunneling from the deep-level states near the ZnO/GaN interface to the conduction band in *n*-ZnO. The nonlinearity of experimental data in the $\ln(J/F^3)$ vs. F^{-1} plot suggests that the electrons tunneling from the valence band in *p*-GaN directly to the conduction band in *n*-ZnO is much smaller, might be due to the much larger energy barrier for electrons tunneling from the valence band in *p*-GaN than that from the deep-level states near the ZnO/GaN interface.

5.2.6 White light in CIE chromaticity coordinate

The EL image from this LED displayed in the inset of Fig.5.4, exhibiting a bright white-light emission due to the mixing of the ELs at 450 nm and 550 nm, was strong enough to be observed by the naked eye in daylight. The color chromaticity of the EL spectra shown in Fig.5.4 was calculated using the Commission Internationale de I'Eclairage (CIE) standard color matching function. The calculated CIE chromaticity coordinate of the EL spectrum was (0.31,0.36), which is close to (0.33,0.33) of the pure white light.

5.3 Excitonic Franz-Keldysh effect in ultraviolet electro- luminescence from *n*-ZnO:Al/*p*-GaN:Mg heterojunction light-emitting diodes operated at reverse breakdown bias

5.3.1 Sample preparation

Figure 5.8 shows the schematic diagram of the ZnO:Al/*p*-GaN heterojunction LED. First, a thin GaN buffer layer was deposited on the *c*-Al_2O_3 substrate at 550℃, and then a thick, undoped GaN layer was grown on the buffer layer at 1000℃ by MOCVD. Next, a Mg doped GaN (GaN:Mg) layer was subsequently grown, also by MOCVD. The hole concentration and mobility in the p-type layer are approximately 2.6×10^{17} cm^{-3} and 11.9 $cm^2V^{-1}s^{-1}$, respectively. Afterwards, an 8% Al doped ZnO layer was grown on the *p*-GaN by ALD at 180°C. Diethylzinc (DEZn, $Zn(C_2H_5)_2$), Trimethylaluminum (TMA, $Al(CH_3)_3$) and H_2O were used as the precursors of zinc, aluminum, and oxygen, respectively. Each ZnO growth cycle contained the following sequence: DEZn, 0.01 s → N_2 purge, 5 s → H_2O, 0.1 s → N_2 purge, 5 s for the deposition of ZnO (ZnO cycle). For Al_2O_3 growth cycle, on the other hand, the

precursors were replaced from DEZn to TMA. The deposition process consisted of 13 cycles of ZnO growth followed by 1 cycle of Al_2O_3. Repeating this deposition procedure up to 3000 cycles can achieve delta-doping and thereby ensure that the Al is sprayed uniformly on the ZnO thin film. After deposition, the ZnO layer was treated at 950°C for 5 min in N_2 atmosphere by rapid thermal annealing (RTA) to improve its crystallinity. Hall effect measurement revealed that the electron concentration and mobility in the annealed ZnO were 4.3×10^{18} cm^{-3} and 19.3 cm^{2}V^{-1}s^{-1}, respectively. A circular ZnO mesa 1 mm in diameter was then fabricated by masking the surface and chemically etching the ZnO away using an HCl solution. Ohmic contact to *p*-GaN was made by thermal evaporation of Ni/Au, followed by annealing at 500°C for 30 min in O_2 ambient. A direct probe on top of the *n*-ZnO was used as the *n*-type contact.

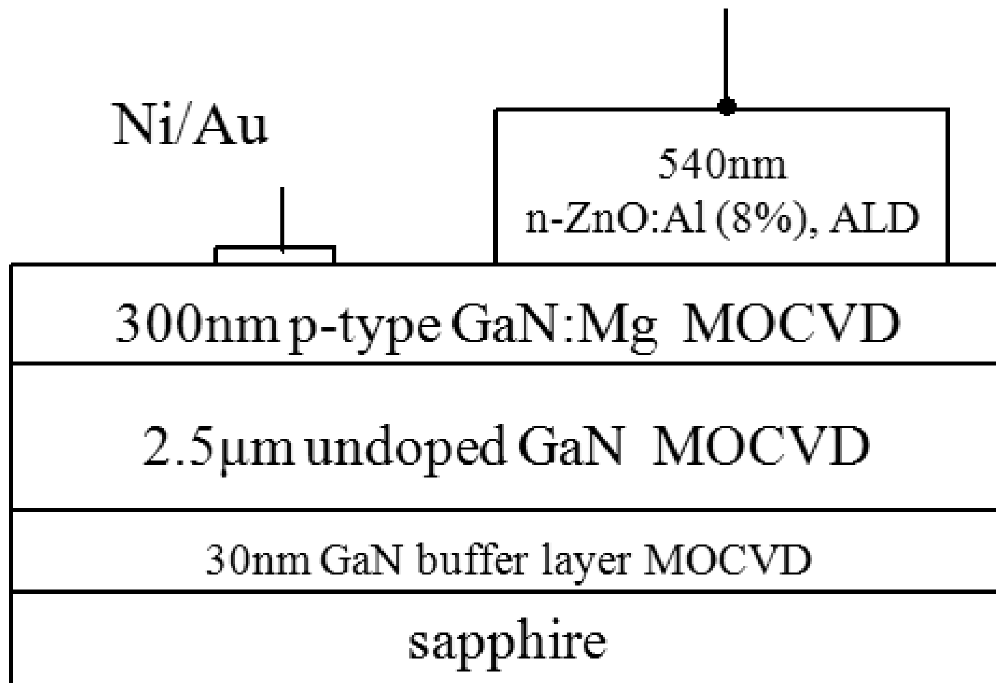

Figure 5.8 The schematic diagram of the 8% *n*-ZnO:Al/*p*-GaN heterojunction LED.

5.3.2 Current vs. voltage (*I-V*) characteristics

Figure 5.9 shows the current-voltage (*I-V*) characteristics of the *n*-ZnO:Al/*p*-GaN:Mg hetrojunction LED. It may be noted that the type II ZnO/GaN band alignment with large band offsets leads to a low injection current at forward bias. However, an onset of reverse breakdown appeared around (-)11V after which the current increased rapidly with the reverse bias. The reverse breakdown for *p-n* junctions with a breakdown voltages of less than about $4E_g/q$ (E_g~3.4 eV is the bandgap energy of ZnO or GaN) can not be attributed to the avalanche multiplication [23]. Therefore, in the case of this device, the dramatic increase in current under reverse bias should be ascribed to the electron tunneling from the valence band in *p*-GaN to the conduction band *n*-ZnO (band-to-band tunneling) [16]. According to Ref.[23], the current associated with electron tunneling from the occupied valence band states to the empty conduction band states can be formulated as follows:

$$I_{v\to c} = C_1 \int f_v(E) N_v(E) T_t [1 - f_c(E)] N_c(E) dE \tag{5.5}$$

where C_1 is a constant, *Tt* is tunneling probability, $f_v(E)$ and $f_c(E)$ are the Fermi-Dirac distribution functions, and $N_v(E)$ and $N_c(E)$ are the density of states in valence and conduction band, respectively. Integral Eq.(5.5) from E_c of n-side to E_v of *p*-side leads to the following result [28]

$$J = A \times F^3 \times \exp\left(-\frac{B}{F}\right) \tag{5.6}$$

where *J* is current density, and *A* and *B* are constant related to tunneling barrier, and the average electric field *F* is given by

$$F = \sqrt{\frac{2q\varepsilon_p N_A N_D (\psi_{bi} - V_A)}{\varepsilon_n \left(\varepsilon_p N_A + \varepsilon_n N_D\right)}} \tag{5.7}$$

where ψ_{bi} is the built-in potential, V_A is the applied reverse bias, ε_n and ε_p are the

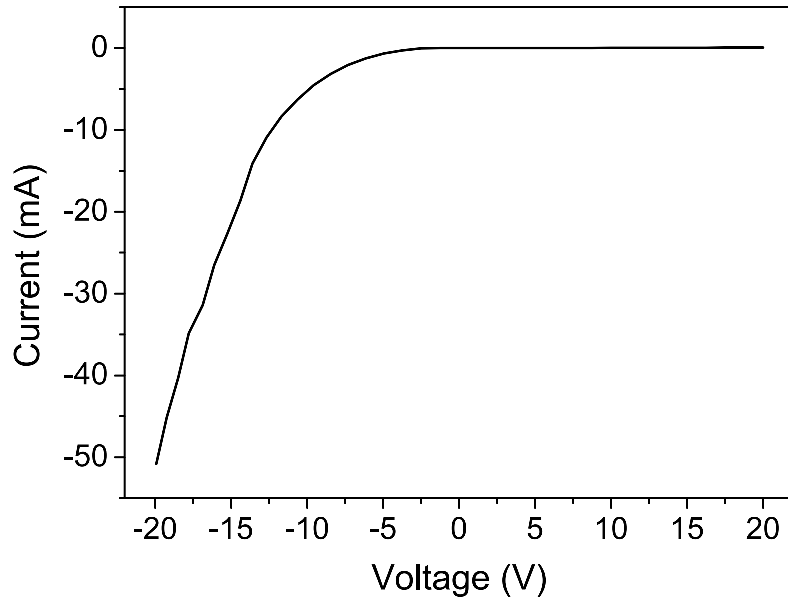

Figure 5.9 Room-temperature Current *vs.* Reverse-bias voltage (*I-V*) curve of the *n*-ZnO:Al(8%)/*p*-GaN heterojunction LED.

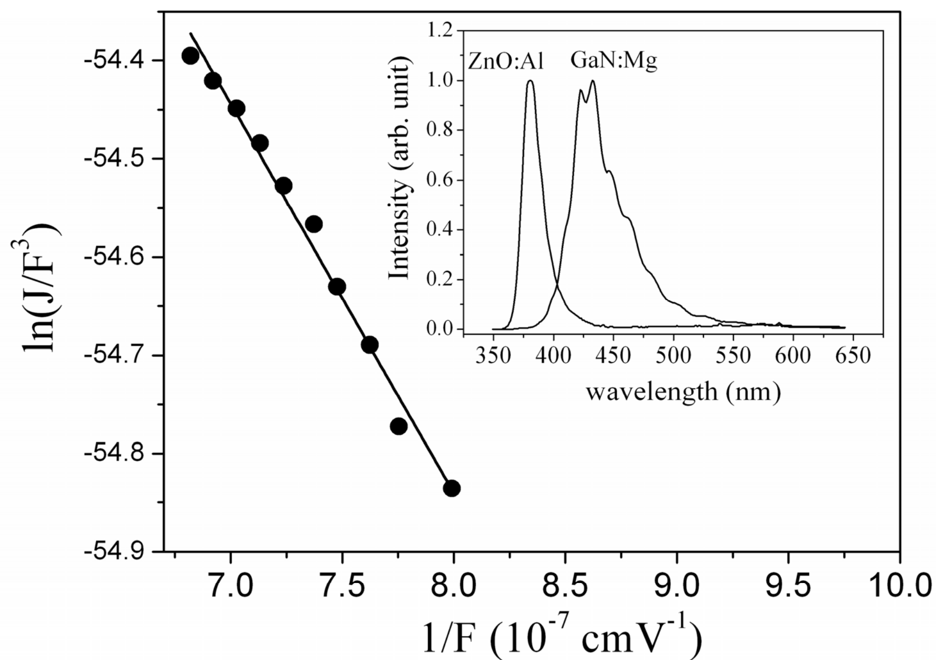

Figure 5.10 The $ln(J/F^3)$ vs. $1/F$ fitting curve of the n-ZnO:Al(8%)/p-GaN heterojunction LED under various reverse bias condition. The linear slope shows the occurrence of the tunnelling. The inset is the room-temperature photoluminescence (PL) spectra of the *p*-GaN layer and *n*-ZnO:Al(8%) layer grown on the *p*-GaN.

permittivity of n and p layers, and N_A and N_D are the acceptor and donor concentrations in p- and n-type regions, respectively. Eq.(5.6) was used to examine the *I-V* characteristics of the LED at reverse breakdown bias in terms of the $\ln(J/F^3)$ vs. F^{-1} plot, as shown in Fig.5.10. The clear linear dependence of $\ln(J/F^3)$ on F^{-} indicates that the electron tunneling from the valence band in p-GaN to the conduction band in n-ZnO is responsible for the breakdown current at the reverse bias.

5.3.3 Photoluminescence of *n*-ZnO:Al and the *p*-GaN films

Normalized photo-luminescence (PL) spectra of the n-ZnO:Al and p-GaN:Mg layers are shown in the inset of Fig. 5.10. Photoluminescence (PL) was measured at room temperature using a He-Cd laser (λ=325 nm) as the excitation source. The PL spectrum of n-ZnO shows a near-band-edge (NBE) UV emission at 380 nm with negligible defect-related bands. The NBE emission is associated with the radiative recombination of free excitons [29]. From the PL spectrum, it can thus be concluded that the ZnO film grown by ALD has a good optical property after annealing. The PL spectrum of p-GaN, on the other hand, reveals only deep-level emission around 425 nm, which can be ascribed to the transitions from the conduction band or unidentified shallow donors to the Mg acceptor levels [24].

5.3.4 Breakdown electroluminescence

Figure 5.11 shows the room-temperature EL spectra of the n-ZnO:Al(8%)/p-GaN:Mg heterojunction LED at reverse breakdown bias. The UV EL shifted significantly from 372 to 396 nm as the injection current increased from 35 to 75 mA. One may wonder whether the red shift in the UV EL spectra is caused by the heating effect due to the current injection at large reverse bias.

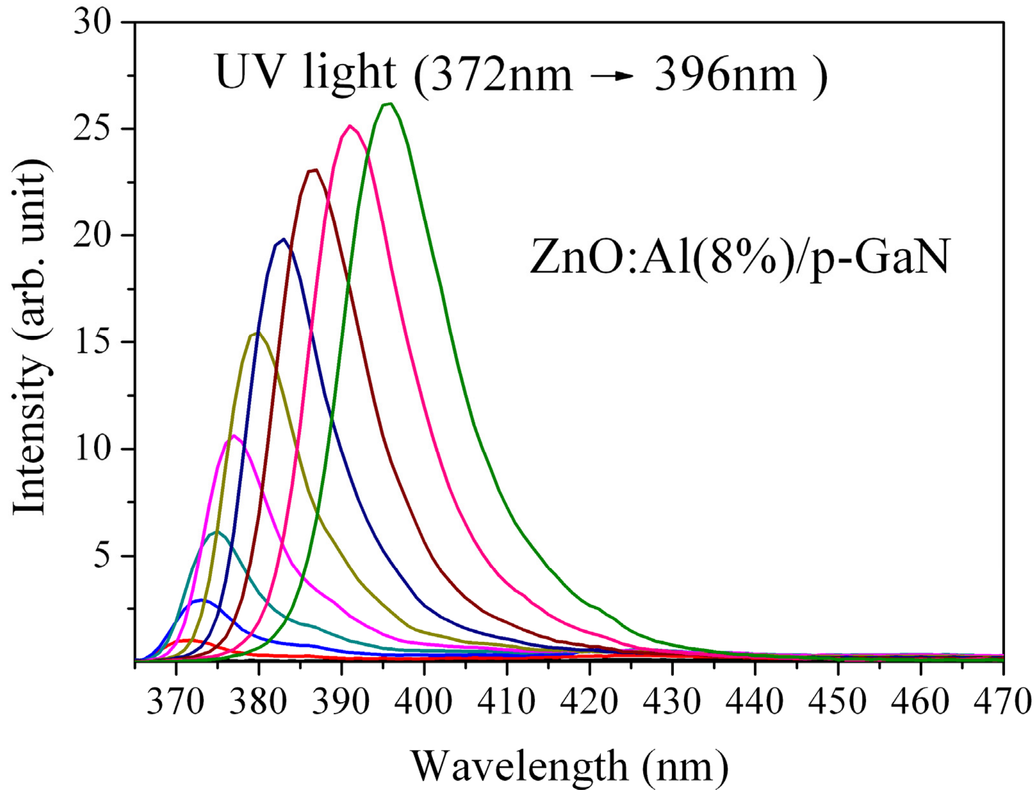

Figure 5.11 Room-temperature electroluminescence (EL) spectra of the *n*-ZnO:Al(8%)/*p*-GaN heterojunction LED measured at various injection currents from 35 mA to 75 mA under the reverse breakdown biases.

In order to determine more clearly the behavior of these EL spectra, the EL spectra of a reference LED with the *n*-ZnO:Al(2%)/*p*-GaN:Mg structure under similar injection currents (from 10 to 40 mA) at reverse breakdown bias was introduced in the Fig. 5.12. It may be noted that the Al doping percentage in the reference LED is only 2%. The EL spectra of the reference LED exhibited a trend similar to that of the present LED (with 8% Al-doped ZnO). At low injection current, the EL spectrum of the reference LED consisted of UV and blue emissions. The UV emission from 372 to 385 nm may originate from the NBE emission from *p*-GaN, and the blue light at 425 nm corresponds to the Mg acceptor state in *p*-GaN as indicated by the PL spectrum shown in the inset in Fig.5.10. It is clearly seen that the UV EL intensity increased gradually, however, the intensity of blue light decreased with the increase in the

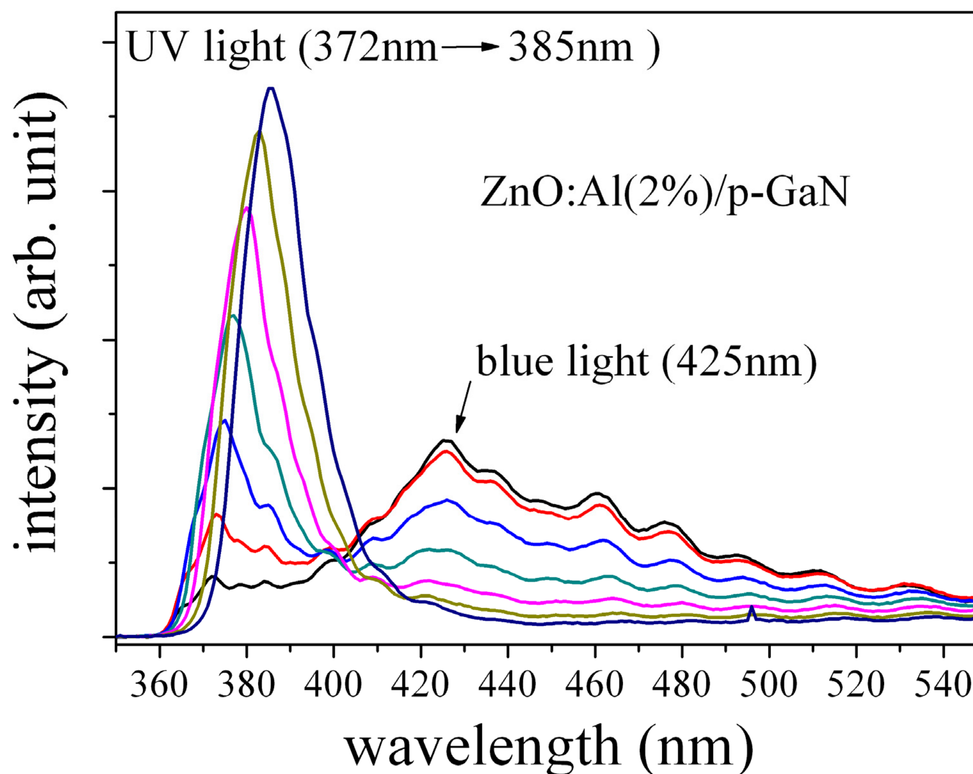

Figure 5.12 The EL spectra of *n*-ZnO:Al(2%)/*p*-GaN heterojunction LED measured at various injection currents under the reverse breakdown biases. This figure shows the intensity of UV light increase with the current increase but the blue light decrease with current increase.

injection current. The suppression of the blue light at 425 nm with the increase in the reverse breakdown bias may be a result of the extension of the depletion region into the bulk of *p*-GaN, which will be addressed detailedly in the following. It can be also observed that the UV emission gradually shifted from 372 nm to 385 nm as the reverse bias increased. However, such a red shift did not appear in the blue light at 425 nm with the increase in the reverse bias. The EL spectra shown in Fig.5.11 of the *n*-ZnO:Al(8%)/*p*-GaN:Mg LED were normalized and shown in Fig.5.13(a). Similarly, the red shift in the blue light at 425 nm was not observed as the injection current increased. In addition, the broadening of spectral peak of the UV EL with increasing the injection current was not obvious. The results suggest that the heating effect can be excluded as the cause of the red shift in the UV EL spectra.

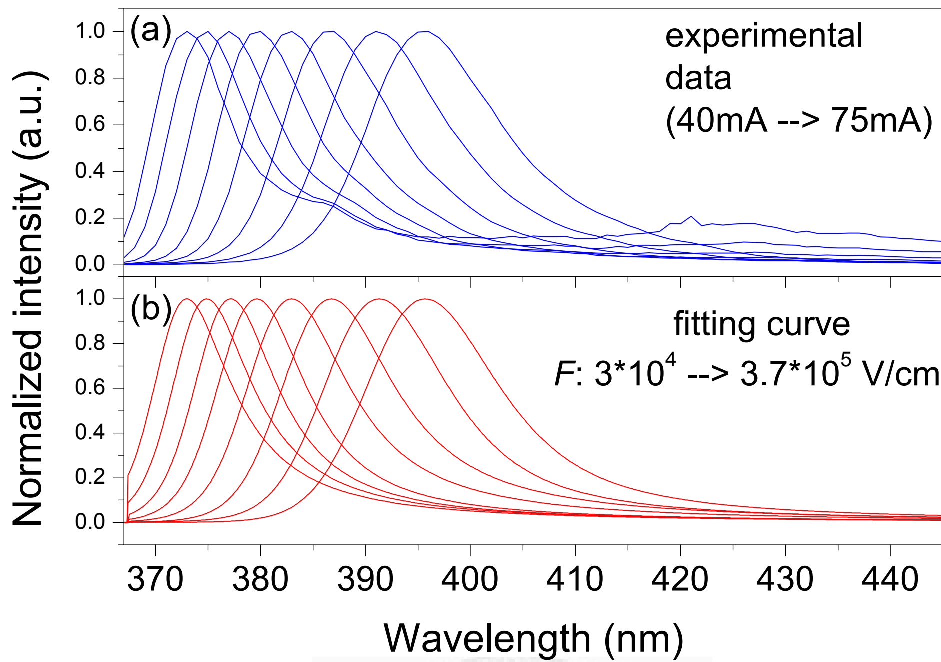

Figure 5.13 The normalized (a) EL spectra (b) fitting curves of *n*-ZnO:Al(8%)/*p*-GaN heterojunction LED.

5.3.5 Discussion

Figure 5.14 hows the band diagram of the *n*-ZnO:Al/*p*-GaN:Mg heterojunction LED under the reverse breakdown bias, which illustrates the mechanisms of carrier transport and UV emission. It can be assumed that the *n*-ZnO/*p*-GaN interface exhibits a type II band alignment where a calculated valence band offset (ΔE_v) varies from 1.0 to 2.2 eV, with an average value of 1.6 eV, depending on the interfacial configuration [30]. Owing to this large band offset formed at the heterojunction, the valence band maximum of *p*-GaN would be higher than the conduction band minimum of *n*-ZnO at small reverse bias [16]. Therefore, the electron tunneling from the valence band in *p*-GaN to the conduction band in *n*-ZnO could take place, and the tunneling probability increases with the reverse bias. As an electron in the *p*-GaN

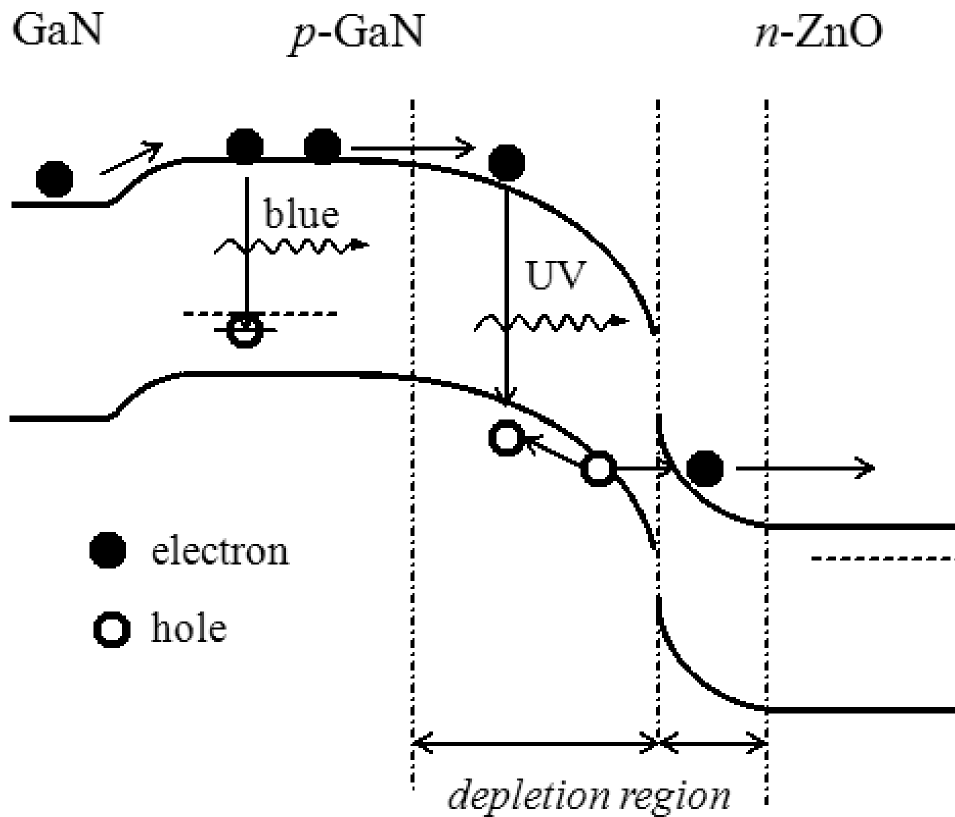

Figure 5.14 The band diagram of the *n*-ZnO:Al(8%)/*p*-GaN heterojunction LED.

valence band tunnels to the *n*-ZnO conduction band, a hole is created at the *p*-GaN near the interface and then drifts into the *p*-GaN layer by the electric field. On the other hand, the electrons in the underlying un-doped (intrinsic *n*-type) GaN are pulled into the conduction band in the *p*-GaN by the large electric field at reverse bias. Thus the NBE UV emission from *p*-GaN is observed as the hole recombines with an electron in the depletion region, in which the Mg acceptor states are inactivated, Otherwise, the blue light is generated when the the radiatively recombination of electrons and holes takes place in the bulk region of *p*-GaN, in which the Mg acceptor states are active. As the reverse bias increased, the depletion region extended into the bulk region; and therefore, the intensity of the blue light at 425 nm was suppressed, as shown in the EL spectra shown in the of Fig. 5.12 and Fig. 5.13(a).

In order to clarify the mechanism behind the red shift in the UV EL spectra, a

theoretical calculation was performed to fit the EL spectra. It is well known that the spontaneous emission spectrum is proportional to the product of density of states and carrier distribution. Since the density of state is also proportional to the absorption coefficient, the light emission spectrum $I(\hbar\omega)$ generally has the form [31],

$$I(\hbar\omega) \propto \alpha(\hbar\omega) \times f(\hbar\omega) \tag{5.8}$$

where $\alpha(\hbar\omega)$ is the absorption spectrum, $f(\hbar\omega)$ is distribution of carriers which is given by the Fermi-Dirac distribution, and E is the photon energy. According to Eq.(5.8), knowledge of the absorption spectrum is necessary to obtain the light emission spectrum.

The absorption spectrum can be derived from the Schrödinger equation of relative motion of the electron-hole pair in the presence of an electric field F and the attractive electron-hole Coulomb potential [32]. Following the steps in Ref.[32], an analytic form of the absorption spectrum was obtained as follows:

$$\alpha(E) = \alpha_{FK}(E)\left\{\Gamma\left(1-\frac{1}{\sqrt{\varepsilon}}\right)\exp\left[\frac{1}{\sqrt{\varepsilon}}\ln\left(\frac{8\varepsilon^{\frac{3}{2}}}{F}\right)\right]\right\}^2 \tag{5.9}$$

where $\alpha_{FK}(\hbar\omega)$ is the absorption spectrum in the presence of an electric field F (known as the Franz-Keldysh efftct) without considering the effect of electron-hole pair (exciton), and ε is to the energy in excitonic unit. The Γ and exponential functions in Eq.(5.9) is a result of the excitonic effect on the absorption spectrum [32]. Afterwards, a convolution of $\alpha_{T=0K}(\hbar\omega)$ with a Lorentzian function, $L(\hbar\omega)$, was carried out to take the carrier scattering into account to obtain the accurate absorption spectrum $\alpha(\hbar\omega)$:

$$\alpha(\hbar\omega) = \int_{-\infty}^{\infty} [\alpha_{EFK}(E) \times L(\hbar\omega - E)]d(E) \tag{5.10}$$

in which

$$L(\hbar\omega - E) = \frac{1}{\pi} \frac{\hbar/\tau_{in}}{(\hbar\omega - E)^2 + \left(\hbar/\tau_{in}\right)^2}. \tag{5.11}$$

where we choose the intraband relaxation time τ_{in} as 16 fs which is in good agreement with other publications. [33-35] Therefore, the theoretical light emission spectra $I(\hbar\omega)$ were obtained according to Eq.(5.8) by the multiplication of the resulting absorption spectrum $\alpha(\hbar\omega)$ of *p*-GaN by the Fermi-Dirac distribution $f(\hbar\omega)$. The fitting parameters in the theoretical calculations were the electric field F at the *p*-GaN depletion region, and Fermi level. The calculated light emission spectra were normalized and shown in Fig. 5.13(b). It can be seen in Fig. 5.13(a) and Fig. 5.13(b) that the theoretical curves agree quite well with the measured spectra experimental data, except for the small peak appearing at 386 nm in the measured spectra, which may originate from the ZnO near the *n*-ZnO/*p*-GaN interface [20]. Accordingly, it can be deduced that the UV EL originates from the electron-hole recombination in *p*-GaN, and the red shift in the UV EL spectra with the reverse breakdown bias results from the excitonic Franz-Keldysh effect under a large electric field in the depletion region of *p*-GaN. It should be note that the good agreement between the theoretical calculation and experimental data van not be achieved without considering the effect of exciton.

5.4 Summary

At reverse breakdown bias, significant white-light EL, consisting of a blue light at 450 nm and a broad yellow band around 550 nm, was observed from the *n*-ZnO/*p*-GaN hetrojunction LED with a high-quality *n*-ZnO epilayer grown by ALD. The blue light comes from the Mg acceptor levels in *p*-GaN, and the yellow band may

be attributed to the deep-level states associated with oxygen vacancies near the *n*-ZnO/*p*-GaN interfaceA theoretical study on the *I-V* characteristics at reverse breakdown bias indicates that the current is dominated by the electrons tunneling from the deep-level states near the ZnO/GaN interface to the conduction band in *n*-ZnO. The mixing color of the EL observed by human eyes located at the coordinate of (0.31,0.36) in chromaticity diagram, which is close to the standard white light. The white-light EL from this reverse-biased LED can be clearly observed even in a bright room.

In addition, a 8% Al doped ZnO film was grown on *p*-GaN by ALD to fabricate the *n*-ZnO:Al/*p*-GaN heterojunction LED. The LED emits UV light under reverse bias, and the luminescence peak wavelength is altered as the bias condition changes. The wavelength of the luminescence peak shifted from 372nm to 396nm as the current increased from 35mA to 75mA. A theoretical calculation has been performed to fit the experimental data, and the fitting result indicates that the UV light originates from the electron-hole recombination in the *p*-GaN depletion region and that the red shift is caused by the increase in the electric field in the depletion region. In addition, the low breakdown voltage can be attributed to the type II band alignment and the large band offset between *n*-ZnO and *p*-GaN, which results in a high tunneling probability from the *p*-GaN valence band to the *n*-ZnO conduction band at a low applied voltage.

Appendix 5A

Derivation of Eq.(5.2)

The rate of tunneling from the state b to the state f can be expressed by Fermi-Golden rule:

$$P = \frac{2\pi}{\hbar}\sum_f \left|\langle f|Fz|b\rangle\right|^2 \delta\left(E_f - E_b\right) \tag{A1}$$

The bound state b and the free state f with their energy E_b and E_f, respectively, are illustrated in Fig.A-1.

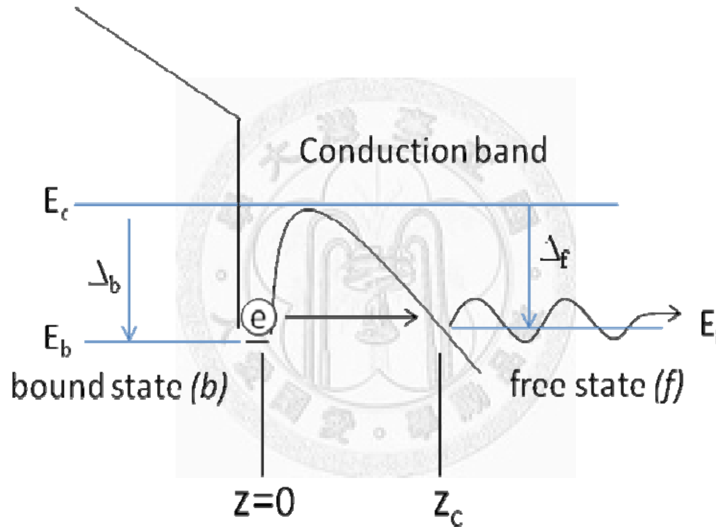

Figure A-1 The band diagram of an electron in a bound state tunneling to a free state.

In order to calculate the tunneling rate, we have to find the wave function of the bound state (deep level state) ψ_b. As an electron is bound in a Coulomb potential well, Schrodinger's equation can be written as follows:

$$\left[\frac{\hbar^2}{2m^*}\nabla^2 + V(r)\right]\psi_b = E\psi_b \tag{A2}$$

For an electron in a bound state, the wave function ψ_b can be assumed to be spherically symmetrical and thus to depend only on the distance r from the center of the bound state. Therefore, Schrodinger's equation takes the form

$$\frac{\hbar^2}{2m^*}\frac{d^2}{dr^2}\left(r\psi_b\right)+V(r)\left(r\psi_b\right)=E\left(r\psi_b\right) \quad \text{(A3)}$$

Let $V(r)=\frac{\alpha}{r}$, we can get the following equation

$$\frac{d^2}{dr^2}\left[r\psi_b(r)\right]=\left[K\left(\Delta_b-\frac{\alpha}{r}\right)\right]^2 r\psi_b(r) \quad \text{(A4)}$$

where Δ_b is the barrier height as shown in Fig. 1, and the $K(\Delta)$ is the wavefunction attenuation constant assumed to be a function of the barrier height. In general, the Δ-K dispersion relation cannot be assumed to be parabolic in this case. Therefore, an Δ-K relation called *Franz-Kane* relation (cf. Fig. A-2) calculated by two-band model will be used.

Because the Coulomb's potential well tail $\frac{\alpha}{r}$ is assumed small, we use the Taylor's expansion to expand the K function

$$K\left(\Delta_b-\frac{\alpha}{r}\right)=K(\Delta_b)-\frac{\alpha}{r}\left(\frac{dK(\Delta)}{d\Delta}\right)_{\Delta=\Delta_b} \quad \text{(A5)}$$

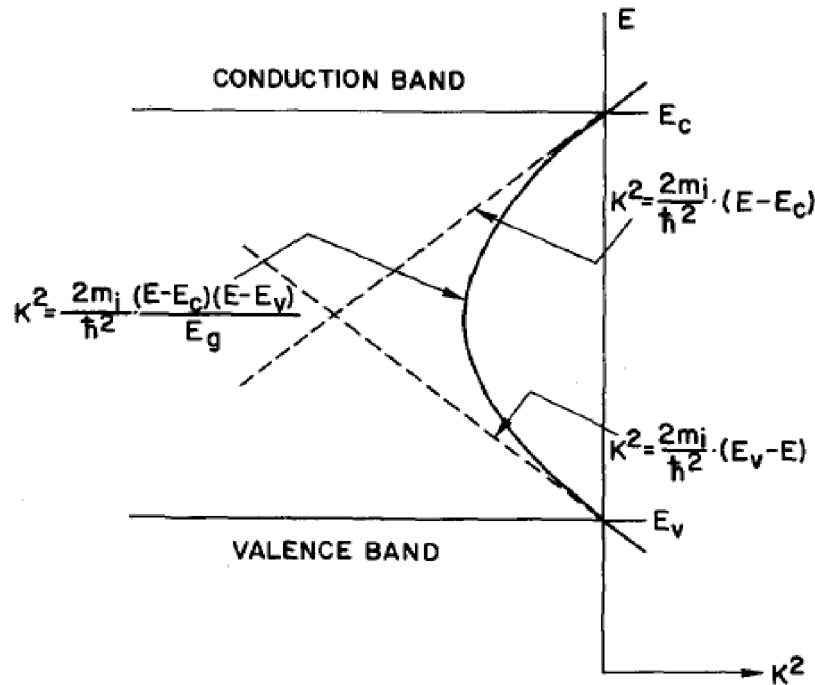

Figure A-2 Energy vs. square of the wave vector for electrons in the forbidden band. (ref. K. H. Gundlach, *J. Appl. Phys.* 44 pp.5005-5010, 1973)

Insert Eq. (A5) into Eq. (A4), the Schrodinger function of the deep level state becomes

$$\frac{d^2}{dr^2}(r\psi_b)=\left[K^2(\Delta_b)-2\frac{\alpha}{r}K(\Delta_b)\frac{dK(\Delta)}{d\Delta}+\left(\frac{\alpha}{r}\frac{dK(\Delta)}{d\Delta}\right)^2\right](r\psi_b) \qquad \text{(A6)}$$

Solve Eq. (A6) within the WKB approximation. Let $\psi_b(r)=r^{\alpha}e^{mr}$ and insert it into Eq. (A6), then we can get the following equation

$$a(a-1)r^{a-2}+2mar^{a-1}+m^2r^a=K^2(\Delta_b)r^a-2p_bK(\Delta_b)r^{a-1}+p_b{}^2r^{a-2} \qquad \text{(A7)}$$

Let $a=p_b$ and $m=-K_b$, we can get the bound state wave function

$$\psi_b(r)=C_br^{p_b+1}e^{-K_br} \qquad \text{(A8)}$$

in which C_b is a constant and $p_b=\alpha\left(\frac{dK(\Delta)}{d\Delta}\right)_{\Delta=\Delta_b}$ and $K_b=K(\Delta_b)$.

Second, we calculate the wave function of the tail of free state in the forbidden region in band gap

$$\left(\frac{\hbar^2}{2m^*}\nabla^2+Fz+\frac{\alpha}{r}\right)\psi_f(r)=E_f\psi_f(r) \qquad \text{(A9)}$$

F is the electric field. For the convenience, we consider z direction only, the Eq. (A9) can be written as

$$\frac{\hbar^2}{2m}\frac{d^2}{dz^2}\psi_f(z)=\left[K\left(\Delta_f-Fz-\frac{\alpha}{z}\right)\right]^2\psi_f(z)=K_f^2\psi_f(z) \qquad \text{(A10)}$$

the *K(Δ)* is the wavefunction attenuation constant and follows the *Franz-Kane* relation. Assume that $\psi_f(z)=e^{\frac{i}{\lambda}\sigma(z)}$, its first derivate is

$$\psi_f'(z)=\frac{i}{\lambda}\sigma'e^{\frac{i}{\lambda}\sigma} \qquad \text{(A11)}$$

and the second derivate is

$$\psi_f''(z)=\frac{i}{\lambda}\sigma''e^{\frac{i}{\lambda}\sigma}-\frac{1}{\lambda^2}(\sigma')^2e^{\frac{i}{\lambda}\sigma} \qquad \text{(A12)}$$

Insert Eq. (A11) and (A12) into equation (A10), we can get the following equation

$$\frac{\hbar^2}{2m}\left[\frac{i}{\lambda}\sigma''e^{\frac{i}{\lambda}\sigma}-\frac{1}{\lambda^2}(\sigma')^2e^{\frac{i}{\lambda}\sigma}\right]=K_f^2e^{\frac{i}{\lambda}\sigma} \qquad \text{(A13)}$$

Now, we expand the phase function *σ(z)* formally in powers of *λ/i*

$$\sigma = \sigma_0 + \left(\frac{\lambda}{i}\right)\sigma_1 + \left(\frac{\lambda}{i}\right)^2 \sigma_2 + \cdots \tag{A14}$$

Derivate Eq. (A13) and keep only the first two terms. We can get the first and second derivates of Eq. (A13) as following

$$\sigma' = \sigma_0' + \left(\frac{\hbar}{i}\right)\sigma_1' \tag{A15}$$

$$\sigma'' = \sigma_0'' + \left(\frac{\lambda}{i}\right)\sigma_1'' \tag{A16}$$

Insert Eq. (A15) and (A16) into equation (A13), and we can get the following equation

$$-\left[(\sigma_0')^2 + \frac{2\lambda}{i}\sigma_0'\sigma_1' - \lambda^2(\sigma_1')\right] + i\lambda\left[\sigma_0'' + \left(\frac{\lambda}{i}\right)\sigma_1''\right] = 2mK_f^2 = K^{*2} \tag{A17}$$

And compare the various orders of λ

(1) Consider the order of λ^0, we obtain

$$\sigma_0'^2 = -K^{*2}, \tag{A18a}$$

or

$$\sigma_0' = \pm iK^* \tag{A18b}$$

in which $K^* = K^*\left(\Delta_f - Fz - \frac{\alpha}{z}\right) = K^*\left(\Delta_f' - \frac{\alpha}{z}\right)$ and using the Taylor's expansion to expand K^*, we can get

$$K^*\left(\Delta_f' - \frac{\alpha}{z}\right) \cong K^*(\Delta_f') - \frac{\alpha}{z}\left(\frac{dK^*(\Delta)}{d\Delta}\right)_{\Delta=\Delta_f'} \tag{A19}$$

insert this equation into Eq. (A18b), we can obtain

$$\sigma_0' = \pm i\left(K^*(\Delta_f') - \frac{\alpha}{z}\left(\frac{dK^*(\Delta)}{d\Delta}\right)_{\Delta=\Delta_f'}\right) = \pm i\left(K^*(\Delta_f') - \frac{p_f}{z}\right) \tag{A20}$$

Then, solve the differential equation, the zero order phase function σ_0 can be written as

$$\sigma_0 = \pm i\left(\int_z^{z_c} K^*(\Delta_f')dz + \int_z^{z_c} -\frac{p_f}{z}dz\right) \tag{A21}$$

the integral boundary z_c in Eq. (A21) has been defined in Fig. A-1 and the other boundary z is in the forbidden region ($z < z_c$).

(2) Consider the first order terms (λ) we have

$$2\sigma_0'\sigma_1' + \sigma_0'' = 0 \tag{A22}$$

so that

$$\sigma_1 = \frac{1}{2}\ln\left(\frac{C}{K^*(\Delta_f')}\right) \tag{A23}$$

in which C is a constant produced by the integration. Summarizing the results, from Eq. (A21) and (A23), we obtain

$$\psi_f(z) = e^{\frac{i}{\lambda}\sigma}$$

$$= \exp\left[\frac{i}{\lambda}\left(\pm i\int_z^{z_c} K^*(\Delta_f')dz \mp i\ln\left(\frac{z_c}{z}\right)^{p_f} + \frac{\lambda}{i}\ln\left(\frac{C}{K^*(\Delta_f')}\right)^{1/2}\right)\right]$$

$$= \left(\frac{C}{K^*(\Delta_f')}\right)^{1/2}\left(\frac{z_c}{z}\right)^{\frac{\pm p_f}{\lambda}} \exp\left(\mp\frac{1}{\lambda}\int_z^{z_c} K^*(\Delta_f')dz\right) \tag{A24}$$

using λ=1, we can obtain

$$\psi_f(z) = \left(\frac{C}{K^*(\Delta_f')}\right)^{1/2}\left(\frac{z_c}{z}\right)^{\pm p_f} \exp\left(\mp\int_z^{z_c} K^*(\Delta_f')dz\right) \tag{A25}$$

In the region of $z < z_c$, Eq. (A25) describes an exponentially increasing or decaying solution in the classically forbidden region. The exponentially increasing solution is clearly unphysical and has to be discarded, so that we have in the classically forbidden region should be

$$\psi_f(z) = \left(\frac{C}{K^*(\Delta_f')}\right)^{1/2}\left(\frac{z_c}{z}\right)^{p_f} \exp\left(-\int_z^{z_c} K^*(\Delta_f')dz\right) \tag{A26}$$

The $K^*(\Delta_f')$ can be regarded as constant K_f if z is close to z_c (in high electric field), and considering that z deviates only slightly from r, i.e.,

$$z = r\cos\theta \approx r\left(1 + \frac{\theta^2}{2}\right) \tag{A27}$$

so that,

$$\exp\left(-\int_z^{z_c} K_f dz\right) = \exp\left[-K_f \cdot (z_c - z)\right]$$

$$= \exp\left[-K_f \cdot \left(z_c - r + \frac{r\theta^2}{2}\right)\right]$$

$$= e^{-K_f(z_c - r)} e^{-\frac{rK_f}{2}\theta^2} \tag{A28}$$

In order to match the spherical wave function at bound state, we averaging the angle-dependent part of the $\psi_f(z)$ and get only *r* dependent wave function

$$\psi_f(z) = \int \psi_f(z) d\theta d\phi$$

$$= \int \frac{C}{K_f}\left(\frac{r_c}{r}\right)^{p_f} e^{-\frac{rK_f}{2}\theta^2} e^{-K_f(z_c - r)} d\theta d\phi$$

$$= \frac{1}{\sqrt{2\pi}} \frac{C}{K_f} r_c^{p_f} e^{-K_f z_c} r^{-p} \frac{1}{2K_f r} e^{K_f r} = C_f r^{-p_f - 1} e^{K_f r} \tag{A29}$$

in which C_f is a constant. Expand the *z*-axis dependent wave function (Eq. (A29)) into all directions, so that, the wave function of the free state can be written as

$$\Psi_f(r) = \psi_f(r_\perp) \cdot \psi_f(z)$$

$$= \left(A_\perp e^{k_\perp r_\perp}\right)\left(C_f r^{-p_f - 1} e^{K_f r}\right) \tag{A30}$$

where, $k_\perp$ and $r_\perp$ is the wave vector and distance variable in the direction perpendicular to the *z*-direction, and $A_\perp$ is a constant. From the bound and free states wave function Eq. (A8) and Eq. (A30), the matrix element in Eq. (A1) can be calculated as

$$\langle f|Fz|b\rangle = \int \Psi_f^*(Fz)\Psi_b dz$$

$$= A_\perp e^{k_\perp r_\perp} \times F\cos^2\theta \int \psi_f^* \times r \times \Psi_b dr$$

$$= A_\perp e^{k_\perp r_\perp} \times F\cos^2\theta \times \left(\int C_f r^{-p_f - 1} e^{K_f r} \times r \times C_b r^{p_b + 1} e^{-K_b r} dr\right)$$

$$= A_\perp e^{k_\perp r_\perp} \times C_{fb} \times F \int r^{p_b - p_f} \times r \times e^{(K_f - K_b)r} dr \tag{A31}$$

Further, by recalling that we are mainly interested in transition for which $\Delta_f \cong \Delta_b$, we will set $K_f \sim K_b$, and $p_f = p_b \sim 1$. Therefore, we obtain

$$\langle f|Fz|b\rangle = A_\perp e^{k_\perp r_\perp} \times C_{fb} \times F \int_0^\infty r dr$$

$$= A_\perp e^{k_\perp r_\perp} \times C'_{fb} \times F \times \left(\int_0^{z_c} z dz \right)$$ (neglect the region $z>z_c$, the overlap is small)

$$= A_\perp e^{k_\perp r_\perp} \times C'_{fb} \times F \times \frac{z_c^2}{2}$$ ($z_c^2 = \left(\frac{\Delta_{f=b}}{eF} \right)^2$)

$$= A_\perp e^{k_\perp r_\perp} \times C''_{fb} \times \frac{1}{F} \tag{A32}$$

where the C_{fb} are constants. So that

$$\left| \langle f | Fz | b \rangle \right|^2 = \left| A_\perp e^{k_\perp r_\perp} \right|^2 \times C''_{fb} \times \frac{1}{F^2} \tag{A33}$$

Finally, from Eq. (A1), the summation over the final states is transformed into a triple integral in k space and thus into the expression:

$$P = \frac{1}{\pi} \frac{m^{*2}}{\hbar^5} \left[\int_{E=0}^{\infty} \delta(E - E_b) \times \int_{E_\perp=0}^{E} \left| \langle f | Fz | b \rangle \right|^2 \frac{dE_\perp}{k_{zf}} dE \right]$$

$$= \frac{1}{\pi} \frac{m^{*2}}{\hbar^5} \times \int_0^{\infty} \left| \langle f | Fz | b \rangle \right|^2 \times \delta(E - E_b) \int_{E_\perp=0}^{E} \left| A_\perp e^{k_\perp r_\perp} \right|^2 dE_\perp dE$$

$$= D_{fb} \times \left(\frac{1}{F^2} \right) \times \left(B_1 F \times e^{-\frac{B_2}{F}} \right)$$

$$= \frac{C_1}{F} \exp\left(-\frac{C_2}{F} \right) \tag{A32}$$

in which the C_1 and C_2 are constants. On the other hand the integration $\int_{E_\perp=0}^{E} \left| A_\perp e^{k_\perp r_\perp} \right|^2 dE_\perp$ is illustrated in the Appendix 5B.

Appendix 5B

Derivation of Eq.(5.4)

The probability T of band to band tunneling (cf. Fig. B-1) can be written as

$$T = \frac{\pi^2}{9}\exp\left(-2\int_0^{x_1}|ik|dx\right) \qquad \text{(B1)}$$

in which, k is the electron wave vector. Consider the x direction as the current direction, and decompose k into

$$k^2 = k_x^2 + k_y^2 + k_z^2 = k_x^2 + k_\perp^2 \qquad \text{(B2)}$$

so that,

$$T = \frac{\pi^2}{9}\exp\left(-2\int_0^{x_1}\sqrt{k_x^2 + k_\perp^2}\,dx\right) \qquad \text{(B3)}$$

using $k_x^2 = \frac{2m^* qF}{\hbar^2}x$ and $k_x = k_\perp \cdot \tan\theta$, we can get the following equation

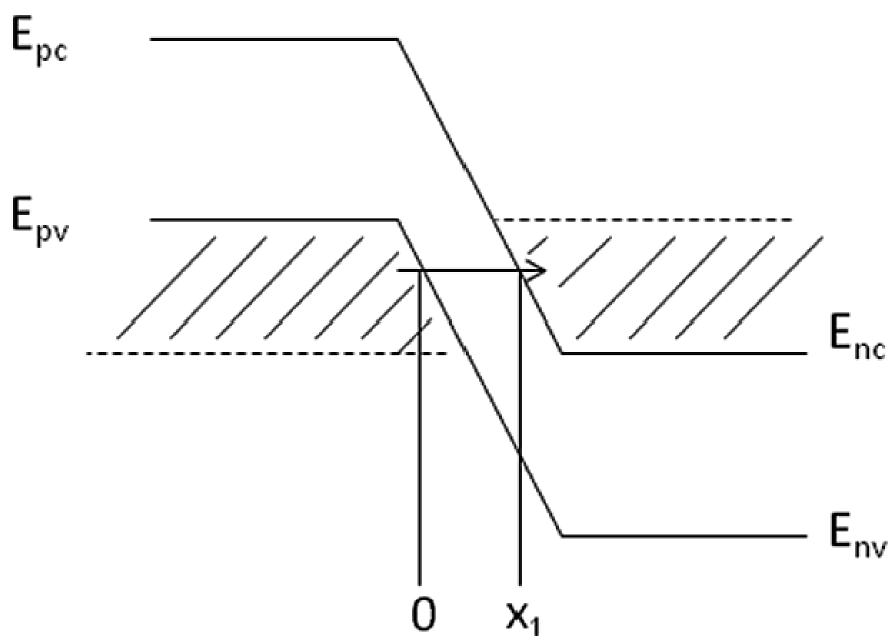

Figure 5B-1 Band diagram of the p-n junction and the shadow region is the band to band tunneling region.

$$\int_0^{x_1}\sqrt{k_x^2+k_\perp^2}\,dx=\int_{k_{down}}^{k_{up}}(2k_x)\times\left(\frac{\hbar^2}{2mqF}\right)\times\sqrt{k_x^2+k_\perp^2}\,dk_x$$

$$=\int_{\theta_{down}}^{\theta_{up}}(2k_\perp\tan\theta)\times\left(\frac{\hbar^2}{2mqF}\right)\times k_\perp\times\sqrt{\tan^2\theta+1}\times\left(k_\perp\sec^2\theta\right)d\theta$$

$$=\left(\frac{\hbar^2}{m^*qF}\right)\times k_\perp^3\times\int_{\theta_{down}}^{\theta_{up}}\left(\tan\theta\sec^3\theta\right)d\theta$$

$$=\left(\frac{\hbar^2}{m^*qF}\right)\times k_\perp^3\times\left(\frac{1}{3}\sec^3\theta\right)\Bigg|_{\theta_{down}}^{\theta_{up}}$$

$$=\left(\frac{\hbar^2}{3m^*qF}\right)\times k_\perp^3\times\left\{\left[\left(\frac{\frac{2m^*qFx_1}{\hbar^2}}{k_\perp^2}\right)+1\right]^{\frac{3}{2}}-1\right\}\qquad (E_g=qFx_1)$$

$$=\left(\frac{\hbar^2}{3m^*qF}\right)\times\left\{\left[\left(\frac{2m^*E_g}{\hbar^2}\right)+k_\perp^2\right]^{\frac{3}{2}}-\left(k_\perp^2\right)^{\frac{3}{2}}\right\}$$

$$=\left(\frac{\hbar^2}{3m^*qF}\right)\times\left(\frac{2m^*}{\hbar^2}\right)^{\frac{3}{2}}\times\left\{\left(E_g+E_\perp\right)^{\frac{3}{2}}-E_\perp^{\frac{3}{2}}\right\}\qquad (E_\perp=\frac{\hbar^2k_\perp^2}{2m^*})$$

$$=\left(\frac{2^{\frac{3}{2}}m^{*\frac{1}{2}}}{3\hbar F}\right)\times\left[E_g^{\frac{3}{2}}+\frac{3}{2}E_g^{\frac{1}{2}}E_\perp\right]\qquad\text{(B4)}$$

where m^* is the effective mass of electron, F is the electric field, E_g is the band gap energy, and $E_\perp$ is the kinetic energy of electron perpendicular to the x-axis. Then, we expand the Eq. (B4) with Taylor expansion to first order and insert it into Eq. (B3). Therefore, the band to band tunneling probability can be written as

$$T=\frac{\pi^2}{9}\exp\left(-2\times\left(\frac{2^{\frac{3}{2}}m^{*\frac{1}{2}}}{3\hbar F}\right)\times\left[E_g^{\frac{3}{2}}+\frac{3}{2}E_g^{\frac{1}{2}}E_\perp\right]\right)$$

$$=\frac{\pi^2}{9}\exp\left(\frac{-2^{\frac{5}{2}}m^{*\frac{1}{2}}E_g^{\frac{3}{2}}}{3\hbar F}\right)\exp\left(-2^{\frac{3}{2}}\frac{m^{*\frac{1}{2}}E_g^{\frac{1}{2}}}{\hbar F}E_\perp\right)$$

$$= \frac{\pi^2}{9} \exp\left(\frac{-2^{\frac{5}{2}} m^{*\frac{1}{2}} E_g^{\frac{3}{2}}}{3\hbar F} \right) \exp\left(-2E_\perp / \bar{E} \right) \quad \text{(B5)}$$

in which,

$$\bar{E} = \frac{\sqrt{2}\hbar F}{m^{*\frac{1}{2}} E_g^{\frac{1}{2}}} \quad \text{(B6)}$$

In order to obtain the tunneling current density, we using a simple model of a diode

$$J = nev \quad \text{(B7)}$$

where n is the carrier concentration, and v is the velocity of the carrier, which can be replaced by

$$v = \frac{1}{\hbar} \frac{\partial E}{\partial k_x} \quad \text{(B8)}$$

After all, we integrate the tunneling current through whole the tunneling region. Therefore,

$$J = \frac{e}{4\pi^3\hbar} \int\int T(E_\perp) dk_\perp dk_x \frac{\partial E}{\partial k_x}$$

$$= \frac{em^*}{2\pi^2\hbar^3} \int\int_0^{E-E_x} T(E_\perp) dE_\perp dE_x \qquad \left(dk_\perp = k_\perp dk_\perp d\phi = \frac{m^* dE_\perp d\phi}{\hbar^2} \right)$$

$$= \frac{em^*}{18\hbar^3} \exp\left(\frac{-\pi m^{*\frac{1}{2}} E_g^{\frac{3}{2}}}{2\sqrt{2}\hbar F} \right) \int\int_0^{E-E_x} \left[f_1(E_1) - f_2(E_2) \right] \times \exp\left(-2E_\perp / \bar{E} \right) dE_\perp dE_x \quad \text{(B9)}$$

where, $f_1(E)$ and $f_2(E)$ are the occupancy factor in n and p side. In reverse bias, we assume the states in p-type valance band and n-type conduction band are fully occupied and unoccupied, therefore, the factors f_1 and f_2 are 1 and 0. Base on that, the integral limits should be range from E_{nc} to E_{pv} (cf. Fig. B-1).

$$J = \frac{em^*}{18\hbar^3} \exp\left(\frac{-\pi m^{*\frac{1}{2}} E_g^{\frac{3}{2}}}{2\sqrt{2}\hbar F} \right) \int_{E_{nc}}^{E_{pv}} \int_0^{E-E_x} \exp\left(-2E_\perp / \bar{E} \right) dE_\perp dE_x \quad \text{(B10)}$$

because of the value of E_x distribute from *0* to E, therefore, dE_x can be change to dE and the integral limits are change to *0 to E*.

$$J = \frac{em^*}{18\hbar^3}\exp\left(\frac{-\pi m^{*\frac{1}{2}} E_g^{\frac{3}{2}}}{2\sqrt{2}\hbar F}\right) \times \frac{\bar{E}}{2} \times \int_{E_{nc}}^{E_{pv}} \left[1 - \exp\left(-2E/\bar{E}\right)\right] dE \tag{B11}$$

Define the integration as D

$$D = \int_{E_{nc}}^{E_{pv}} \left[1 - \exp\left(-2E/\bar{E}\right)\right] dE$$

$$= \left(E_{pv} - E_{nc}\right) + \frac{\bar{E}}{2} \times \left[\exp\left(-2E_{pv}/\bar{E}\right) - \exp\left(-2E_{cn}/\bar{E}\right)\right] \tag{B12}$$

In the situation that $\bar{E}$ is much smaller than eV (applied voltage), the *exp* terms in the equation can be ignored. Therefore,

$$D \approx \left(E_{pv} - E_{nc}\right) = eV \tag{B13}$$

where the applied voltage V can be replaced by the electric field through the following dependence when $V >> \psi_{bi}$

$$F = \sqrt{\frac{q(\psi_{bi} - V)N_A N_D}{2\varepsilon_s(N_A + N_D)}} \cong \sqrt{\frac{q(V)N_A N_D}{2\varepsilon_s(N_A + N_D)}} \tag{B14}$$

Therefore,

$$D = C \times F^2 \tag{B15}$$

where C is a constant. Insert Eq. (B6) and Eq. (B15) into Eq. (B11), we can get the electric field related current density as following

$$J = A \times F^3 \times \exp\left(-\frac{B}{F}\right) \tag{B16}$$

in which the A and B are constants.

Reference

[1] W. Y. Liang and A. D. Yoffe, Phys. Rev. Lett., vol.20, pp.59-62, 1968.

[2] A. Tsukazaki, A. Ohtomo, T. Onuma, M. Ohtani, T. Makino, M. Sumiya, K. Ohtani, S. F. Chichibu, S. Fuke, Y. Segawa, H. Ohno, H. Koinuma and M. Kawasaki, Nature Mater., vol.4, pp.42-46, 2005.

[3] M. H. Huang, S. Mao, H. Feick, H. Yan, Y. Wu, H. Kind, E. Weber, R. Russo, and P. Yang, Science, vol.292, pp.1897-1899, 2001.

[4] W. I. Park, Y. H. Jun, S. W. Jung, and Gyu-Chul Yi, Appl. Phys. Lett., vol.82, pp.964-966, 2003.

[5] Ü. Özgür, Ya. I. Alivov, C. Liu, A. Teke, M. A. Reshchikov, S. Doğan, V. Avrutin, S.-J. Cho, and H. Morkoç, J. Appl. Phys., vol.98, 041301, 2005.

[6] L. Niinistö, J. Päiväsaari, J. Niinistö, M. Putkonen and M. Nieminen, Phys. Stat. Sol. (a), vol.201, pp.1443-1452, 2004.

[7] H. C. Chen, M. J. Chen, M. K. Wu, Y. C. Cheng and F. Y. Tsai, *IEEE J. Selected Topics Quantum Electronics*, vol.14, pp.1053-1057, 2008.

[8] D. C. Look, B. Claflin, Ya. I. Alivov and S. J. Park, Phys. Stat. Sol. (a), vol.201, pp.2203-2212, 2004.

[9] X. H. Pan, J. Jiang, Y. J. Zeng, H. P. He, L. P. Zhu, Z. Z. Ye, B. H. Zhao and X. Q. Pan, J. Appl. Phys., vol.103, 023708, 2008.

[10] Ya. I. Alivov, J. E. Van Nostrand, D. C. Look, M. V. Chukichev and B. M. Ataev, Appl. Phys. Lett., vol.83, pp.2943-2945, 2003.

[11] D. J. Rogers, F. Hosseini Teherani, A. Yasan, K. Minder, P. Kung and M. Razeghi, Appl. Phys. Lett., vol.88, 141918, 2006.

[12] S. J. Jiao, Y. M. Lu, D. Z. Shen, Z. Z. Zhang, B. H. Li, J. Y. Zhang, B. Yao, Y. C. Liu and X. W. Fan, *Phys. Stat. Sol. (c)*, vol.3, pp.972-975, 2006.

[13] H. Y. Xu, Y. C. Liu, Y. X. Liu, C. S. Xu, C. L. Shao and R. Mu, *Appl. Phys. B*, vol.80, pp.871-874, 2005.

[14] R. W. Chuang, R. X. Wu, L. W. Lai, and C. T. Lee, *Appl. Phys Lett.*, vol.91, 231113, 2007.

[15] H. S. Yang, S. Y. Han, Y. W. Heo, K. H. Baik, D. P. Norton, S. J. Pearton, F. Ren, A. Osinsky, J. W. Dong, B. Hertog, A. M. Dabiran, P. P. Chow, L. Chernyak, T. Steiner, C. J. Kao, G. C. Chi, *Jpn. J. Appl. Phys.*, vol.44, pp.7296-7300, 2005.

[16] W. I. Park and G. C. Yi, *Adv. Mater.*, vol. 16, pp.87-90, 2004.

[17] E. Titkov, A. S. Zubrilov, L. A. Delimova, D. V. Mashovets, I. A. Liniichuk, and I. V. Grekhov, Semiconductors, vol.41, pp. 564–569, 2007.

[18] M. Willander, O. Nur, Q. X. Zhao, L. L. Yang, M. Lorenz, B. Q. Cao, J. Z. Perez, C. Czekalla, G. Zimmermann, M. Grundmann, A. Bakin, A. Behrends, M. Al-Suleiman, A. El-Shaer, A. C. Mofor, B. Postels, A. Waag, N. Boukos, A. Travlos, H. S. Kwack, J. Guinard, and D. L. S. Dang, *Nanotechnology*, vol.20, 332001, 2009.

[19] A. M. C. Ng, Y. Y. Xi, Y. F. Hsu, A. B. Djurisic, W. K. Chan, S. Gwo, H. L. Tam, K. W. Cheah, P. W. K. Fong, H. F. Lui, and C. Surya, *Nanotechnology*, vol.20, 445201, 2009.

[20] M. K. Wu, Y. T. Shih, W. C. Li, H. C. Chen, M. J. Chen, H. Kuan, J. R. Yang, and M. Shiojiri, *IEEE Photonics Technol. Lett.*, vol.20, pp.1772-1774, 2008.

[21] Y. T. Shih, M. K. Wu, W. C. Li, H. Kuan, J. R. Yang, M. Shiojiri and M. J. Chen, *Nanotechnology*, vol.20, 165201, 8pp, 2009.

[22] H. C. Chen, M. J. Chen, M. K. Wu, W. C. Li, H.L Tsai, J. R. Yang, H. Kuan and M. Shiojiri, *IEEE Journal of Quantum Electronics* **46**, pp.265-269, 2010.

[23] S. M. Sze and K. K. Ng, “Physics of Semiconductor Devices”, 3ed Edition, John Wiley & Sons, pp.104 and pp.422-424, (2007)

[24] U. Kaufmann, M. Kunzer, M. Maier, H. Obloh, A. Ramakrishnan, B. Santic, and P. Schlotter, *Appl. Phys. Lett.*, vol.72, pp.1326-1328, 1998.

[25] A. Billeb, W. Grieshaber, D. Stocker, E. F. Schubert, R. F. Karlicek, *Appl. Phys. Lett.*, vol.70, pp.2790-2792, 1997.

[26] D. C. Reynolds, D. C. Look, and B. Jogai, *J. Appl. Phys.*, vol. 89, pp.6189-6191, 2001.

[27] S. Makram-Ebeid and M. Lannoo, Phys. Rev. B, vol.25, pp.6406-6424, 1982.

[28] E. O. Kane, *J. Appl. Phys.*, vol. 32, pp.83-91, 1961.

[29] Y. Chen, D. Bagnall, and T. Yao: Mater. Sci. Eng. B **75** 190 (2000).

[30] T. Nakayama, M. Murayama, *J. Cryst. Growth*, **214**, 299 (2000).

[31] E. F. Schubert, “Light Emitting Diodes”, 2ed Edition, Cambridge University Press, Cambridge, 2003.

[32] H. Hang, S. W. Koch, “Quantum Theory of the Optical and Electronic Properties of Semiconductors”, 5th edition, world scientific, pp.360, 2009.

[33] W. Fang and S. L. Chuang, Appl. Phys. Lett. **67** 751 (1995).

[34] J. Piprek, R. K. Sink, M. A. Hansen, J. E. Bowers, and S. P. Denbaars, ‘Simulation and optimization of 420 nm InGaN/GaN laser diodes’, Proc. SPIE-Int. Soc. Opt. Eng., 2000, 3944, pp. 28–39.

[35] L. H. Peng, C. W. Chuang, and L. H. Lou, Appl. Phys. Lett. **74** 795 (1999).

Chapter 6

Conclusion

In this thesis, we present the low-threshold stimulated emission of the ZnO and ZnO:Al epilayers grown on *c*-Al_2O_3 by ALD and treated by post-deposition RTA and furnace annealing process. The XRD measurement indicates that the ZnO epilayer was highly *c*-axis orientated and the cross-sectional TEM images show that the columnar structures were not formed in the ZnO epilayer, which may be attributed to the layer-by-layer growth and low deposition temperature of ALD. The HRTEM images display that a distorted ZnO layer exists at the ZnO/sapphire interface. Because of the relaxation of the misfit by the interfacial distorted layer coupled with the layer-by-layer growth of ALD, no obvious threading dislocations appeared in the TEM images even though the lattice mismatch between ZnO and *c*-Al_2O_3 is up to 18 %. A dominant UV emission at 3.28 eV with a negligible defect band was shown in the spontaneous emission PL spectrum ascribed the good crystalline quality of the ZnO epilayer.

The presence of Al in ZnO films reduces the stimulated emission threshold. With the increase in the Al concentration the threshold of stimulated emission decreases from 49.2kW/cm^2 of 0% to 12.2kW/cm^2 of 4% Al doping percentage. The segregation of excess Al in the heavily doped ZnO:Al films might contribute to the optical scattering centers, resulting in close-loop paths and coherent feedback, and be responsible for the reduction in the threshold of stimulated emission with the increasing Al doping percentage.

We also fabricated the *n*-ZnO/*p*-GaN heterojunction LEDs by growing *n*-ZnO epilayer using ALD on the *p*-GaN and found that light emission from the Mg acceptor

levels in *p*-GaN is obvious at a low injection current. With the increase in the forward bias emission from *n*-ZnO gradually dominate the EL spectrum. Competition between the ELs from ZnO and GaN is elucidated to be attributed to the interfacial layer as well as the differences in the light emission efficiency and the carrier concentration in *n*-ZnO and *p*-GaN layers. The achievement of UV EL at a low DC injection current from ZnO indicates that the ZnO epilayers grown by the ALD technique are effectually applicable to the next-generation short-wavelength photonic devices. In addition, an aluminum external-feedback reflector was evaporated on the back of the double-polished c-Al_2O_3 substrate. Remarkable enhancement of the UV EL intensity, superlinear increase in the EL intensity, coupled with the spectral narrowing, from ZnO with the injection current are attributed to the external optical feedback and ASE in the high-quality ZnO epilayer. The achievement of the electrically pumped ASE in a ZnO epilayer grown by ALD indicates that the ALD technique is applicable to the high-quality ZnO for next-generation UV photonic devices.

On the other hand, significant white-light EL, consisting of a blue light at 450 nm and a broad yellow band around 550 nm, was observed from the *n*-ZnO/*p*-GaN hetrojunction LED at reverse breakdown bias. The blue light comes from the Mg acceptor levels in *p*-GaN, and the yellow band may be attributed to the deep-level states associated with oxygen vacancies near the *n*-ZnO/*p*-GaN interface. A theoretical study on the *I-V* characteristics at reverse breakdown bias indicates that the current is dominated by the electrons tunneling from the deep-level states near the ZnO/GaN interface to the conduction band in *n*-ZnO. The mixing color of the EL observed by human eyes located at the coordinate of (0.31,0.36) in chromaticity diagram, which is close to the standard white light. The white-light EL from this reverse-biased LED can be clearly observed even in a bright room.

In addition, a 8% Al doped ZnO film was grown on *p*-GaN by ALD to fabricate

the *n*-ZnO:Al/*p*-GaN heterojunction LED. The LED emits UV light under reverse bias, and the luminescence peak wavelength is altered as the bias condition changes. The wavelength of the luminescence peak shifted from 372nm to 396nm as the current increased from 35mA to 75mA. A theoretical calculation has been performed to fit the experimental data, and the fitting result indicates that the UV light originates from the electron-hole recombination in the *p*-GaN depletion region and that the red shift is caused by the increase in the electric field in the depletion region. In addition, the low breakdown voltage can be attributed to the type II band alignment and the large band offset between *n*-ZnO and *p*-GaN, which results in a high tunneling probability from the *p*-GaN valence band to the *n*-ZnO conduction band at a low applied voltage.